DETERMINATION OF ENGINEERING PROPERTIES OF STEEL-CONCRETE INTERFACE OF REINFORCED CONCRETE EXPOSED TO MARINE ENVIRONMENT

Thesis

Submitted in partial fulfilment of the requirements for the degree of

DOCTOR OF PHILOSOPHY

by

SHARAN KUMAR

DEPARTMENT OF CIVIL ENGINEERING

NATIONAL INSTITUTE OF TECHNOLOGY KARNATAKA,

SURATHKAL, MANGALURU – 575 025

JULY 2020

DETERMINATION OF ENGINEERING PROPERTIES OF STEEL-CONCRETE INTERFACE OF REINFORCED CONCRETE EXPOSED TO MARINE ENVIRONMENT

Thesis

Submitted in partial fulfilment of the requirements for the degree of

DOCTOR OF PHILOSOPHY

by

SHARAN KUMAR

(155018CV15F08)

Under the Guidance of

Dr. BIBHUTI BHUSAN DAS
Associate Professor, CED

Dr. SHASHI BHUSHAN ARYA
Assistant Professor, MME

DEPARTMENT OF CIVIL ENGINEERING

NATIONAL INSTITUTE OF TECHNOLOGY KARNATAKA,

SURATHKAL, MANGALURU - 575025

JULY 2020

DECLARATION

I hereby declare that the Research Thesis entitled "**Determination of Engineering Properties of Steel-Concrete Interface of Reinforced Concrete Exposed to Marine Environment"** which is being submitted to the **National Institute of Technology Karnataka, Surathkal** in partial fulfilment of the requirements for the award of the Degree of **Doctor of Philosophy** in **Civil Engineering** is a bonafide report of the research work carried out by me. The material contained in this Research Thesis has not been submitted to any University or Institution for the award of any degree.

Place: NITK, SURATHKAL

Date:

SHARAN KUMAR

155018CV15F08

Research Scholar

Department of Civil Engineering

CERTIFICATE

This is to certify that the Research Thesis entitled "**Determination of Engineering Properties of Steel-Concrete Interface of Reinforced Concrete Exposed to Marine Environment"** submitted by **SHARAN KUMAR** (Registration number: 155018CV15F08) as the record of research work carried out by him, is accepted as Research Thesis submission in partial fulfilment of the requirements for the award of degree of **Doctor of Philosophy**.

Dr. BIBHUTI BHUSAN DAS

Department of Civil Engineering

Research Supervisor

Dr. SHASHI BHUSHAN ARYA

Department of Metallurgical and Materials Engineering

Research Supervisor

Dr. SWAMINATHAN K

Department of Civil Engineering

Chairman - DRPC

Dedicated to

My Beloved Parents

and

Teachers

ACKNOWLEDGEMENTS

I would like to express my sincere gratitude to the authorities of NITK Surathkal, for providing me excellent facilities and comfortable stay in the campus. And also thank all the teaching and non-teaching staff of Department of Civil Engineering, National Institute of Technology Karnataka, Surathkal, for their co-operation and help during the project work.

Special thanks to all my friends at NITK who were always co-operative and friendly to me. I sincerely thank all my friends, Mr. Shivaprasad K N, Mr. Sourab M, Ms. Snehal K, Mr. B P Sharath, Mr. Sumukh E P, Mr. Prasanna K M, Dr. Parameswhwar Hiremath, Dr. Punith Kotagi, Dr. Darshan C Shekar, Mr. Prasad Naik and many others for all the support during this experimental work.

Special thanks to Mrs. Sunanda Panda and my little friend Mr. Shreesham Das for being on my side during good and bad times. The time spent with our research group and every moment of my Ph.D. journey has been engraved in my heart.

Finally, I wish to express my warmest regards to all my beloved family members and special thanks to my beloved wife Mrs. Ashwini Goudar, without whose encouragement and support this work would not have been possible. I have no words to thank them for showering love and affection to me and all the sacrifices they had to make during all these years.

SHARAN KUMAR

ABSTRACT

In this investigation, engineering properties of steel-concrete interface (SCI) such as porous zone thickness and calcium hydroxide content around the reinforcing steel were studied through the measurement of ultimate bond strength and also by employing advance characterization techniques such as scanning electron microscopy (SEM) powered with energy dispersive spectroscopy (EDS) and nano-indentation. Three types of cements, i.e., ordinary Portland cement (OPC), Portland pozzolana cement (PPC), and Portland slag cement (PSC) were used in this study and their influence towards the SCI properties was determined. A reliable grayscale-based thresholding technique was used to determine the porous zone thickness at SCI. The nano mechanical properties of concrete such as hardness and modulus of elasticity around the SCI were analysed using nano-indentation technique. Also, the effect of marine environment exposure on ultimate bond strength and porous zone thickness of SCI was investigated.

A detailed sample preparation technique for scanning electron microscopy (SEM) studies is proposed and ensured for a minimal damage to the SCI properties as compared to the methods adopted by the earlier researchers. It is to be noted that engineering properties of SCI were found to be quite influenced by the curing period. There found to be a reduction in mean porous zone thickness because of a prolonged curing period. Nano-indentation analysis revealed that average hardness and modulus of elasticity values around SCI were 0.8 GPa and 30 GPa, respectively.

It is also observed that exposure of reinforced concrete (RC) samples to marine environment till the age of 180-days increased the bond strength. The microstructure study revealed that corrosion products penetrated the porous zone between steel and concrete and increased friction during pull out test which resulted in increased bond strength. However, RC samples exposed to marine environment for a longer period of 720-days induced severe corrosion and the ultimate bond strength between steel and concrete found to be reduced significantly. This can be attributed to the fact that corrosion products filled the porous zone completely and the expansive pressure in the concrete induced cracking that resulted in the reduction in ultimate bond strength between steel and concrete.

CONTENTS

TABLE OF CONTENTS

LIST OF FIGURES

xi

LIST OF TABLES

NOMENCLATURE

The following is a general list of abbreviations used throughout the chapters.

SCI	Steel-Concrete Interface
CH	Calcium hydroxide
SEM	Scanning electron microscope
BSE	Back scatter electron
EDS	Energy dispersive spectroscopy
C-S-H	Calcium silicate hydrate
NaCl	Sodium chloride
EIS	Electrochemical impedance spectroscopy
w/c	Water cement ratio
w/b	Water binder ratio
ITZ	Interfacial transition zone
SCC	Self compacting concrete
OPC	Ordinary Portland cement
PPC	Portland pozzolana cement
PSC	Portland slag cement
FEA	Finite element analysis
C_3S	Tricalcium silicate
C_2S	Dicalcium silicate
$Ca(OH)_2$	Calcium hydroxide
GHPC	Green high performance concrete
GGBS	Ground granulated blast furnace slag
CA	Coarse aggregates
FA	Fly ash
PZT	Porous zone thickness

CHAPTER – 1

INTRODUCTION

1.1 GENERAL

Reinforced concrete (RC) is considered to be one of the most versatile and durable construction materials in the present world. It consists of steel and concrete, which are two different kinds of materials. The non-homogeneity between steel and concrete in RC results in the formation of a distinct area at their interface which found to be porous in nature (Page, 1975; Monteiro, Gjorv and Mehta, 1985; Horne, Richardson and Brydson, 2007). This distinct interfacial area between steel and concrete is being referred as steel-concrete interface (SCI). It is being reported that SCI is porous and of several micron meter thickness in size (Scrivener and Pratt, 1996; Horne, Richardson and Brydson, 2007; Chen *et al.*, 2018). The porous nature of SCI influences the bond strength and durability of reinforced concrete structures (Zhu and Bartos, 2000).

There are many durability issues of reinforced concrete such as chloride migration, carbonation of concrete, sulfate ingression and etc., that leads to corrosion of steel in reinforced concrete structures (Santhanam *et al*., 2001; Moreno *et al.*, 2004; Guo *et al.*, 2015) Particularly in marine environment, chloride ions diffuse through the pore structure of concrete and starts accumulating at SCI. The diffusion time of chloride ions can be increased by providing an appropriate thickness of concrete cover in reinforced concrete structures. Concrete cover protects the reinforcing steel from corrosion and it ensures the reinforcement can be actively engaged without slipping when loaded (Castel *et al.*, 2000). Providing a suitable concrete cover ensures a tortuous path for chloride ion diffusion, but, eventually they reach SCI. Once the chloride threshold limit exceeds near the steel surface, corrosion initiation occurs (Söylev and François, 2005). The occurrence of active corrosion of steel in concrete is also determined by the presence of voids or pores at SCI

(Soylev and Franc, 2003). Hence, understanding and characterizing the engineering properties associated to SCI, especially the porous zone around SCI is need of the hour. However, it is noticed that determination of engineering properties associated to SCI is quite challenging and needs advanced characterization techniques. Because of the complexity associated in characterization of SCI, researchers have assumed the properties of SCI, particularly the thickness of porous band which is being referred as porous zone thickness (Glass *et al.*, 2001a; Kenny and Katz, 2015; Chen *et al.*, 2019).

The significance of porous zone around SCI can be found in service life prediction models (Castel et al., 2003; El Maaddawy and Soudki, 2007; Horne, Richardson and Brydson, 2007; Chernin, Val and Volokh, 2010; Chen et al., 2018). However, researchers reported that larger porous area around SCI is in favor of increasing time required for crack initiation of concrete (Chernin, Val and Volokh, 2010; Chen et al., 2018), which leads to prolong the service life of corrosion affected reinforced concrete structures exposed to marine environment. On the other way, larger porous area around SCI has other adverse effects such as bond strength degradation, enough oxygen and moisture available for faster corrosion of reinforcement bars (C. L. Page, 2009; Kenny and Katz, 2012). Hence, systematic characterization of SCI, especially the porous zone between steel and concrete is need of the hour.

Because of the limited information, it is often assumed that SCI has similar properties as that of aggregate cement paste interface. In most of the service life prediction models, where porous zone between steel and concrete was considered, it has been assumed that SCI has uniform porous zone thickness of 10-20 μm, which is nearly same as the porous zone between aggregate cement paste interface (Ollivier, Maso and Bourdette, 1995; Scrivener and Pratt, 1996; Brough and Atkinson, 2000; Chen et al., 2018) without any further experimental verification. Thus, assuming a steady value of porous zone thickness for all kinds of concretes seems to be an oversimplification. In addition, engineering properties of SCI can be characterized with respect to the formation of hydration products (Horne, Richardson and Brydson, 2007) as well and also with their elastic properties such as elastic modulus (Zhao, Dai and Jin, 2012) and hardness (Zacharda, Štemberk and

2

Němeček, 2018). Researchers have also measured the ultimate bond strength between steel and concrete as an indirect tool for the assessment of the quality of steel-concrete interface (Castel *et al.*, 2003; T. A. Soylev and François, 2003; Kenny and Katz, 2010; Yalciner, Eren and Sensoy, 2012).

It is to be noted that characterization of SCI is a complex and challenging process. It is reported that there are good chances of disturbing the properties of SCI during sample collection and sample preparation for microstructure studies. Few experimental studies regarding geometric characterization of SCI can be found in the literature (Kenny and Katz, 2012; Chen *et al.*, 2018). Researchers used advanced characterization tools such as scanning electron microscope (SEM) equipped with energy dispersive spectroscopy (EDS) to characterize the microstructure properties of SCI. Porosity and pore size distribution and formation of hydration products especially the calcium hydroxide was studied using SEM and EDS (Scrivener, Crumbie and Laugesen, 2004; Horne, Richardson and Brydson, 2007; Zhao, Wu and Jin, 2013). Researchers used backscattered electron (BSE) imaging technique to characterize SCI properties, which is an advanced technique to study the microstructure properties of concrete on a flat polished surface (Glass et al., 2001a; Horne, Richardson and Brydson, 2007; Kenny and Katz, 2015; Chen et al., 2019). However, one of the main issues with BSE imaging is sample preparation of reinforced concrete. Preparation of a flat polished surface with minimal damage to SCI is a challenging process. However, a detailed sample preparation technique for reinforced concrete to obtain BSE images from SEM was not given much importance by researchers (Zayed, 1991; Glass *et al.*, 2001b; Wong *et al.*, 2010). It is to be noted that major damage to the properties of SCI, especially the porous zone thickness may occur during the cutting of reinforced concrete samples for cross-sectional analysis. Visible cracks at SCI can be noticed in the images reported by Wong *et al.*, (2010) and such cracks were noticed in many other literature also (Monteiro, Gjorv and Mehta, 1985; Zayed, 1991; Glass and Reddy, 2002; Wong *et al.*, 2010). From all these studies it was observed that a reliable method of sample preparation technique is yet to be developed where there is minimal damage to SCI.

Nano-indentation is another advanced technique for characterizing the properties of SCI, where elastic modulus and hardness of material can be measured at the nano-level (Mondal, Shah and Marks, 2008; Davydov, Jirásek and Kopecký, 2011; Hu and Li, 2015). Studies reported earlier on steel fiber and cement paste interface through nano-indentation reveals that indentation modulus increases with the increasing distance from the steel fibre surface (Allison *et al.*, 2012). In one of the similar study carried out on interfacial transition zone of steel fibre and cement paste, it is reported that calcium hydroxide was largely concentrated in the transition zone and C-S-H gel was largely concentrated in the bulk denser concrete (Horne, Richardson and Brydson, 2007). Further, research reported on nano-indentation shows that mean modulus of elasticity of clinker is about ~120 GPa, low density C-S-H gel ~20 GPa, high density C S-H gel ~31 GPa and calcium hydroxide ~40 GPa (Němeček, Králík and Vondřejc, 2013). In order to understand and improve macroscopic mechanical performances of cement based materials, it is crucial to inspect their mechanical properties at micro and nano-structural level. In order to improve the engineering and durability properties of reinforced concrete, it is important to study the nanomechanical properties of SCI. From nano-indentation study of SCI, porous zone can be approximated with respect to variation in elastic modulus values from steel surface towards bulk concrete.

Characteristics of SCI can also be accessed through bond strength between steel and concrete, which is an indirect representation of properties and quality of SCI (Turk, Karatas and Ulucan, 2010; Yalciner, Eren and Sensoy, 2012; Kenny and Katz, 2015). The physical properties of SCI definitely influence bond strength properties in reinforced concrete (Castel *et al.*, 2003; Fang *et al.*, 2006). It is important to explore the relationship between bond strength and properties of SCI. It is observed that numerous amounts of literature are available that deal with relationship between pullout test of concrete and rebar properties, but not with respect to the properties of SCI (Ji and Song, 2008; Novidis and Pantazopoulou, 2008; Xu and Wang, 2008).

Secondary cementitious materials have become an integral part of durable and sustainable concrete. The smaller particles and pozzolanic action of mineral admixtures

improve the durability properties of concrete by densifying the microstructure (Das, Singh and Pandey, 2011; Sahoo, Das and Mustakim, 2016; Vedalakshmi *et al.*, 2016). It is also noticed that mineral admixtures are effective in reducing the porosity of interfacial transition zone between aggregate and cement paste (Scrivener and Pratt, 1996; Prokopski and Halbiniak, 2000; Elsharief, Cohen and Olek, 2003; Scrivener, Crumbie and Laugesen, 2004; Shen, Pan and Zhan, 2017). Even though research fraternity has made significant contributions on enhancement of properties of concrete with addition of mineral admixtures, contribution towards important aspects of characterizing SCI is very much limited. It was reported that mineral admixtures have negligible or no effect in reducing porosity at SCI (Sagoe-Crentsil and Glasser, 1990). While, other researchers had reported a reduction in calcium hydroxide content and pH of the pore solution at SCI when mineral admixtures were used (Monteiro, Gjorv and Mehta, 1985; Chris L Page, 2009). However, research findings on the effect of mineral admixtures and mineral admixed cements on the porous zone thickness around SCI yet to be ascertained.

1.2 NEED FOR THE PRESENT WORK

The properties of SCI, especially the porous zone thickness plays an important role in determining the durability properties of reinforced concrete structures. The porous zone thickness around SCI is an important parameter in service life prediction models. A small variation in considering the porous zone thickness leads to misinterpretation of remaining service life of reinforced concrete structures. It is observed that a constant and uniform distribution of porous zone thickness around SCI is being assumed in service life prediction models without any experimental verification. Few recent studies reported that porous zone thickness around SCI is non uniform. Hence, it is understood that a more refined and systematic approach is currently not possible in accurately accessing the porous zone thickness with this amount of reported investigations available in the literature. Thus, characterization of SCI precisely is need of the hour. In the present study, a reliable grayscale-based thresholding technique was used to determine the porous

zone thickness at SCI. Further, nano-mechanical properties of SCI were evaluated through nano-indentation technique.

A detailed sample preparation technique for SEM studies is proposed and ensured for a minimal damage to SCI properties as compared to the methods adopted by the earlier researchers. Further, influence of marine environment on rust distribution in porous zone of SCI and its effect on bond strength of reinforced concrete is explored.

1.3 THESIS STRUCTURE

The thesis is divided into seven chapters. Chapter one gives a brief description of general introduction and need of the study. Chapter two presents a comprehensive review of relevant literature and critical review towards the research gap and objectives of the present investigation. Third chapter contains the materials used in the present study, measurement of compressive strength and bond strength, SEM sample preparation for investigating the properties of SCI and PZT measurement around SCI. Chapter four discusses the factors of sample preparation techniques on the properties of SCI. The effect of speed of cutting the sample on PZT and nano mechanical properties of SCI are discussed. In chapter five, the effect of curing duration on the properties of SCI is analyzed by employing advanced characterization tools such as SEM and EDS. The effect of marine environment on ultimate bond strength and properties of SCI is presented in chapter six. Conclusions along with the major findings from the present work and the scope for future research are presented in chapter seven.

CHAPTER – 2

LITERATURE REVIEW

2.1 GENERAL

This chapter provides a comprehensive review of relevant literature on mechanism of reinforcing steel corrosion, properties, significance, importance and characterization of SCI. Further, the effect of corrosion on the bond strength between steel and concrete is reviewed. The critical review of literature and gaps identified in the literature were also summarized.

2.2 MECHANISM OF REINFORCING STEEL CORROSION IN MARINE ENVIRONMENT

The pore solution of concrete has a pH level of more than 13.5, this high alkalinity creates a passive layer on the steel surface providing better resistance to reinforcement corrosion (Page, 1975). It is well established that concrete produced with low w/c ratio will help in improving the microstructure of concrete. Also, the permeability of aggressive agents such as carbon dioxide, chloride ions, sulfate ions, moisture, etc. has been reduced. It should be noted that a properly designed, executed and maintained reinforced concrete structure should face the very little problem of reinforcement corrosion during its service life (Ahmad, 2003). Because of poor construction practices, the structures which are built in the marine environment are facing great problem of reinforcement corrosion. The prime reason for reinforcement corrosion is ingress of chloride ions and carbonation of cement paste. The pH of the concrete pore solution will be drastically reduced by the ingress of chloride ions which eventually destroys the passive layer around the steel bar and initiates the corrosion process. Once the corrosion of reinforcement bars has been initiated, it progresses at a steady rate. The corrosion

products start to accumulate at the interfacial transition zone of SCI. Because of the volume expansion of corrosion products, the concrete starts to crack and spalling of concrete cover takes place (Morris and Vazquez, 2002). After the spalling of concrete cover sufficient amount of oxygen and moisture will be resupplied to the steel surface through the cracks generated, which further accelerates the corrosion process (Djelal *et al.*, 2016). The corrosion rate has a direct influence on the remaining service life of the reinforced concrete structures in the marine environment (Bhargava *et al.*, 2005). A detailed process of reinforcement corrosion in concrete has been explained in the subsequent section.

2.2.1 Corrosion cell

The reinforcement corrosion in concrete is considered as an electrochemical process. The ACI Committee 222, in the year 1992 states that the reaction which occurs in a flash battery and corrosion of reinforcement bar is similar. The reinforcement bar itself acts as a mixed electrode, upon which coupled cathodic and anodic reactions take place (Equation 2.1 – 2.6). The pore solution of concrete acts as the complex electrolyte which helps in the process of charge transfer from anodic to the cathodic region and vice versa. Thus, a reinforcement corrosion cell is formed (Weyers, Sprinkel and Brown, 2006).

2.2.2 Anodic and cathodic reactions

The anodic and cathodic reactions which occur at SCI were termed as half-cell reactions. The anodic reaction is regarded as oxidation process in which loss of metal takes place. Similarly, the cathodic reaction is termed as reduction process where the reduction of dissolved oxygen forms hydroxyl ions. For the reinforcement corrosion in concrete, the following are the possible anodic reactions depending upon the pH of pore solution which acts as an electrolyte, the existence of aggressive anions and a suitable electrochemical potential at steel surface.

$$3Fe + 4H_2O \rightarrow Fe_3O_4 + 8H^+ + 8e^- \tag{2.1}$$

$$2Fe + 3H_2O \rightarrow Fe_2O_3 + 6H^+ + 8e^- \tag{2.2}$$

$$Fe + 2H_2O \rightarrow HFeO^- \tag{2.3}$$

$$Fe \rightarrow Fe^{2+} + 2e^- \tag{2.4}$$
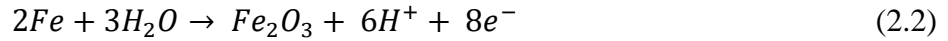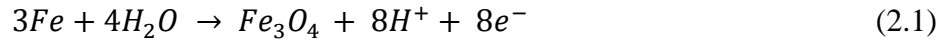
The feasible reduction reactions (cathodic reactions) depend on the ease of access to oxygen and pH at SCI.

$$2H^+ + 2e^- \rightarrow H_2 \tag{2.5}$$

$$2H_2O + O_2 + 4e^- \rightarrow 4OH^- \tag{2.6}$$

2.3 THE STEEL-CONCRETE INTERFACE

The interface refers to a place or an area or a point, where two or more systems with different things meet and interact with or without affecting one another. In case of concrete, there exists a number of interfaces in concrete as it is being produced by the combining several materials of different physical, morphological and chemical characteristics. These interfaces play an important role in determining the unique behavior of concrete. The basic ingredients used for the production of concrete are cement (less than 90 μm in size), water, fine aggregates (μm to mm in size), coarse aggregates (certain mm in size), mineral admixtures such as fly ash (20-60 μm in size), silica fume (less than 0.1 μm in size), ground granulated blast furnace slag (GGBS) (20-50 μm in size), chemical admixtures such as accelerators, retarders, water reducing admixtures etc. These ingredients of concrete have a different range of particle sizes, shape, texture and specific gravities (varies from 1 to 3.15), which is also one of the reasons for non-homogeneity in concrete. Because of the non-homogeneity between different ingredients, there exists a transition zone at their interfaces and is being termed as interfacial transition zone (ITZ) (Scrivener and Pratt, 1996; Prokopski and Halbiniak,

2000; Richardson, 2000; Elsharief, Cohen and Olek, 2003; Chen *et al.*, 2018). One of the important transition zone, that is, ITZ between aggregate and cement paste was explored extensively by the research community. However, there is another transition zone in RC between steel and concrete which has gained the attention of researchers lately and is widely called as steel-concrete interface. With the limited information, it was believed that the characteristics at aggregate-cement paste interface and SCI are considerably same (Zayed, 1991; Chen *et al.*, 2018). But the recent developments in microstructure studies revealed that ITZ properties around the aggregates-cement paste interface, ITZ properties at SCI and bulk cement paste differs significantly (Horne, Richardson and Brydson, 2007).

2.3.1 Significance and importance of steel-concrete interface

The non-homogeneity between steel and concrete in RC results in the formation of a distinct area at their interface which was found to be porous in nature (Page, 1975; Horne, Richardson and Brydson, 2007). The porous nature of SCI was attributed to the wall effect (Scrivener and Pratt, 1996; Page, 2009; Chen *et al.*, 2018). Porosity at SCI is a prime factor in forecasting the time required for corrosion initiation to corrosion cracking (Bhargava *et al.*, 2005; Horne, Richardson and Brydson, 2007; Chen and Mahadevan, 2008; Wang *et al.*, 2009). Prediction of time to corrosion cracking is a key element in evaluating the service life of corroded RC structures. For predicting the time to initial cover cracking, many recent theoretical models have introduced the PZT (PZT) at SCI as one of the important parameter. Tuutti, 1980 proposed a theoretical model to predict the service life of RC structures which did not include the PZT parameter around SCI. The proposed two phase model is shown in Figure 2.1.

According to Tuutti's model of service life prediction, the service life of a structure has two stages of corrosion degradation. The first stage of deterioration is corrosion initiation period (T_o). During this period, the penetration of CO_2 or chloride ions from the outside environment into the RC structure takes place. These ions dissolve in concrete pore solution, also migrate through voids, cracks, and crevices of concrete and finally reach

SCI. Because of higher water to cement ratio at SCI, moisture and oxygen supply will be abundant compared to bulk concrete which triggers the initiation of corrosion process (C. L. Page, 2009). The second stage was called as propagation period (T_{cr}). Soon after the corrosion initiation, the corrosion products start to exert an expansive pressure on the concrete. As the expansive pressure exceeds the tensile strength of concrete, concrete cracking process begins which was considered as end of service life of structures. It was observed that the actual service life of structures was considerably more than the predicted one's by Tuutti's service life prediction model. This confusion led the researchers to investigate SCI properties especially the PZT. Page and Treadaway (1982) reported the existence a porous zone at SCI.
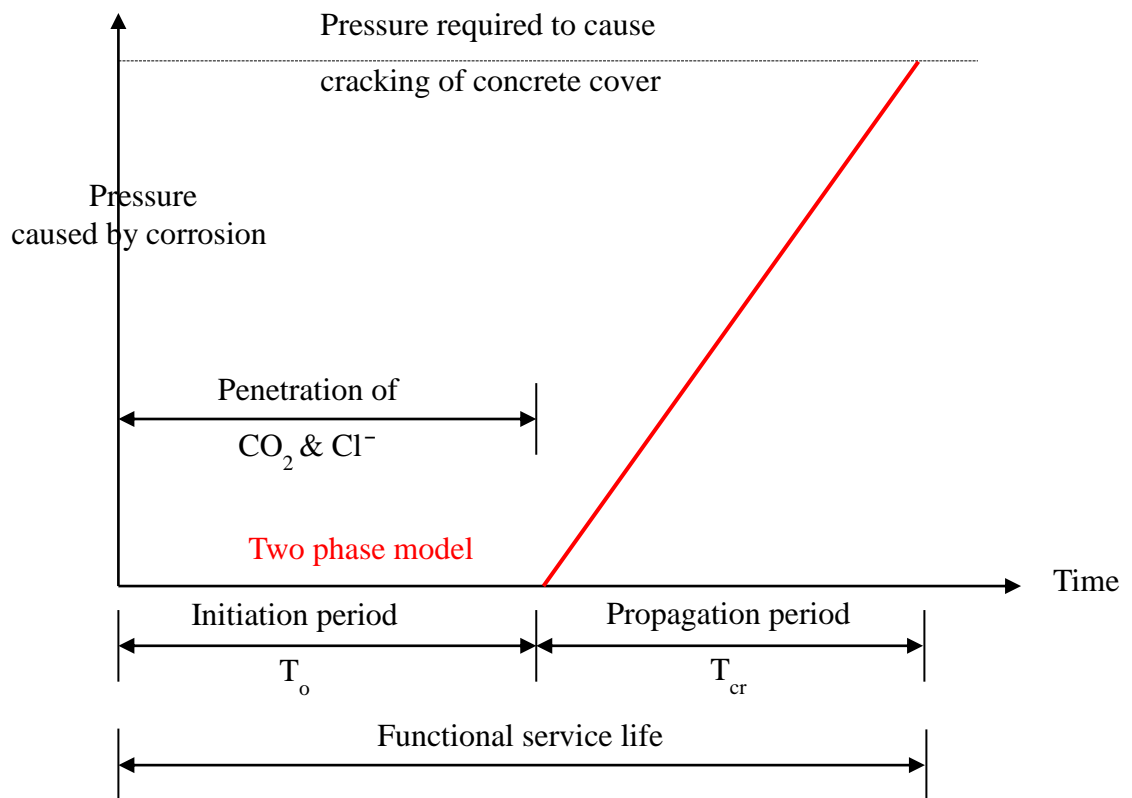
Figure 2.1: Tuutti's service life prediction model of corroded RC structures (Tuutti, 1980)

11

The concept of PZT at SCI was incorporated by Weyers (1998) and proposed a three-stage model for service life prediction as shown in Figure 2.2. In which the free expansion zone was introduced between corrosion initiation and propagation period. In the modified service life prediction model, the propagation period, T_{cr}, was separated into two different periods. The first one is the free expansion period, T_{free}, represents time to fill corrosion products in the porous zone adjacent to corroding steel. The second period, T_{stress}, represents the time in which the corrosion products exerts an expansive pressure on the surrounding concrete as the porous zone was completely filled.

It was proposed that some amount of corrosion products formed after corrosion initiation migrates away from the reinforcing steel through voids and crevices in the concrete and some corrosion products fills the porous zone at SCI. During this period no expansive pressure was exerted on the concrete surface, but once these pores in porous zone were completely filled by the corrosion products, further formation of corrosion products imparts expansive pressure on the concrete surface. This model assumes that, with the increase in the volume of corrosion products the expansive pressure also increases linearly. This induces the tensile stresses inside the concrete. When it exceeds the tensile strength of concrete, cover cracks were generated. Once the cracks were generated, the expansive pressure exerted by corrosion products on the surrounding concrete cannot be quantified as they may discharge out from these cracks. So, the generation of a cover crack in concrete represents the end of service life of the corroded RC structures.

Figure 2.3 shows a schematic diagram of the corrosion-cracking process as proposed by Weyers (1998). This modified service life prediction model was brought up with certain assumptions to formulate the internal radial pressure which occurs due to the expansion of corrosion products. The basic assumption was about the expansive stresses around the steel bar was due to the uniform development of corrosion products around the steel reinforcing bar. Several models on volume expansion by corrosion (Bazant, 1979; Morinaga, 1988; Weyers, 1998) were proposed by using this assumption. But in general, the development of corrosion products around the steel reinforcement bar was not

uniform as the extent of corrosion varies around the steel reinforcing bar. This variation in corrosion is mainly due to non-uniform surface exposure of steel bar to the corroding environment.
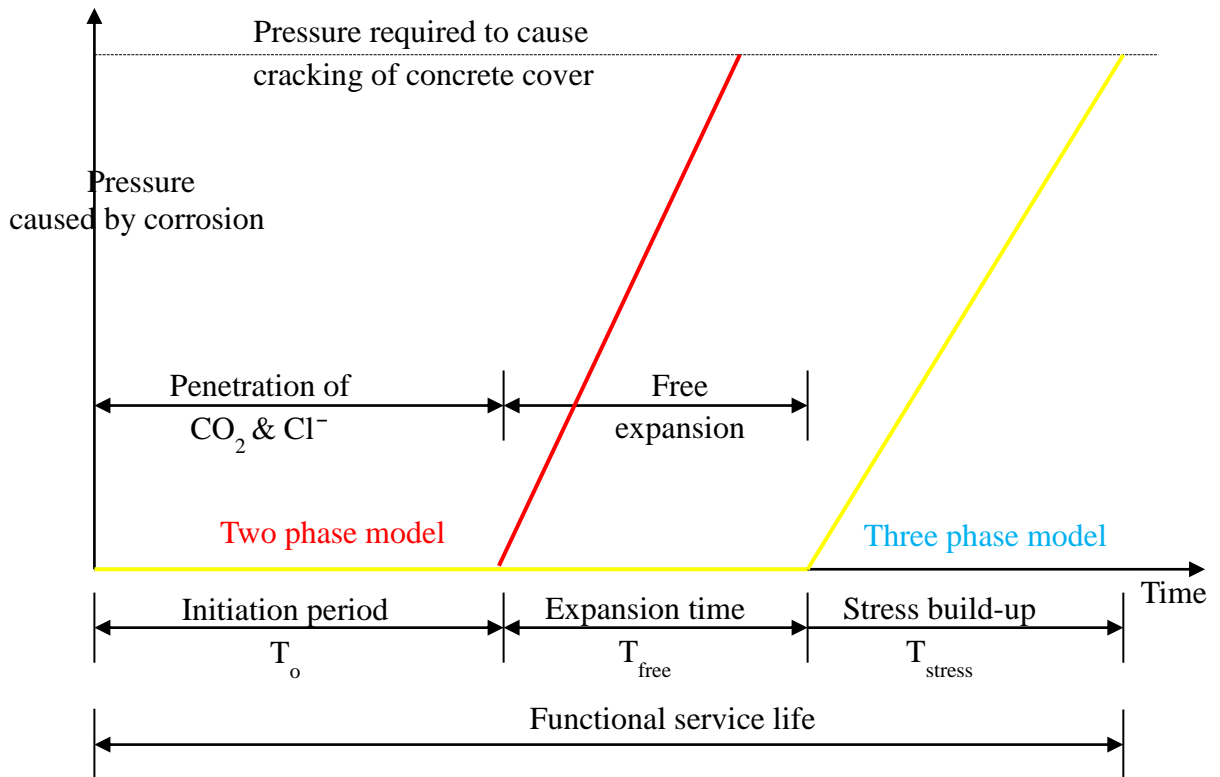
Figure 2.2: Three phase service life prediction model proposed by Weyers, 1998

Liu, (1996) proposed a mathematical model where in mass loss rate of corroding steel and time to fill the porous zone around SCI before exerting the expansive pressure were considered. However, for predicting the remaining service life of structures a constant value of PZT was being assumed without any experimental investigation. Liu, (1996) assumed the occurrence of 12.5 µm thick porous zone and Petre-Lazar and Gérard, (2000) assumed 40 µm thick porous zone around steel bar for modeling and testing purpose. It is also observed that a thickness of 40 µm has been adopted by many others too (Bazant, 1979; Liu, 1996a; Petre-Lazar and Gérard, 2000; Thoft-Christensen, 2000; Bhargava *et al.*, 2005; Chen and Mahadevan, 2008) without any further experimental

verification. It was also observed that a uniform distribution of PZT around the steel bar was assumed by all the previous researchers for assessing the service life of corroding RC structures (Bhargava *et al.*, 2005; Chen and Mahadevan, 2008). The recent developments in the microstructure study of SCI reveal that PZT varies from point to point along the length of reinforcing steel (T. A. Soylev and François, 2003; Horne, Richardson and Brydson, 2007; Kenny and Katz, 2015; Yu, François and Gagné, 2016). Thus, assuming a steady value of PZT and uniform distribution of PZT for all kinds of concretes in modeling seems to be an oversimplification. Also, the physical condition of SCI is considered as an important factor while dealing with the chloride threshold, which in turn influences the prediction of the service life of RC structures (Ann and Song, 2007).

Hence, systematic characterization and understanding about the porosity or PZT at SCI is one of the crucial phenomena in assessing the service life of existing structures in marine environment. A slight variation in considering the PZT in service life prediction models leads to misinterpretation of the actual service life of RC structures. Thus, characterizing SCI has gained the attention among the research fraternity in assessing the primary reason for the corrosion initiation, assessing chloride threshold and modeling the remaining service life of RC structures in the marine environment.

(a) Corrosion initiation

(b) Corrosion product expansion

(c) Stress build up

(d) concrete cracking

(e) Concrete spalling and steel exposed to the environment
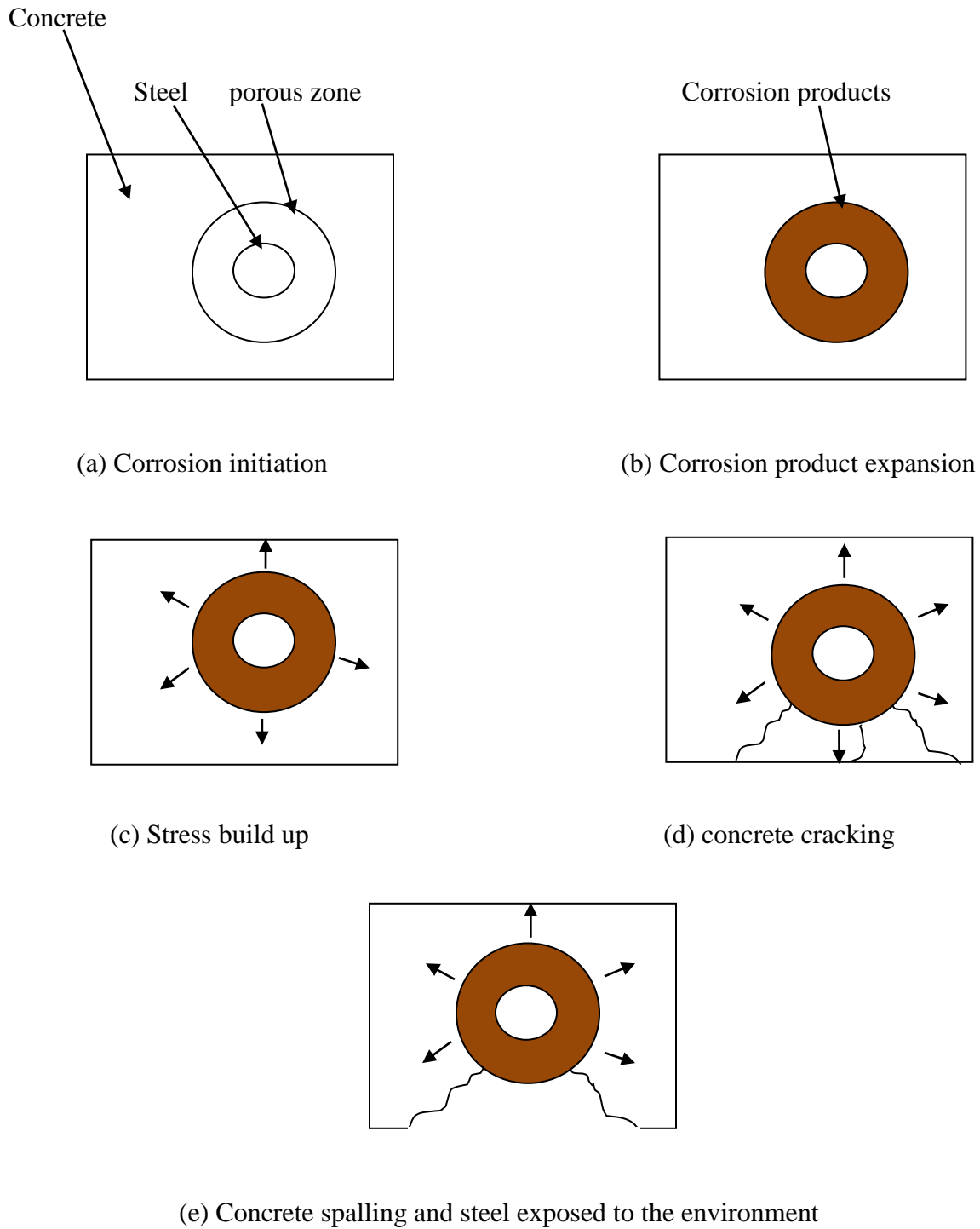
Figure 2.3: Corrosion and cracking process in reinforced concrete (Weyers, 1998)

2.3.2 Why the steel-concrete interface is porous?

When the cement paste comes in contact with stationary reinforcement bar, the cement particles tends to separate out from the cement paste because of the shearing forces and this phenomenon is widely recognized as the 'wall effect'. This action forms a narrow region around the reinforcement bar with fewer cement particles and more water. Thus, water to cement ratio at SCI was higher compared to the bulk concrete. The higher water to cement ratio and fewer cement particles at SCI creates the porous zone (Horne, Richardson and Brydson, 2007). Scrivener et al. (Scrivener, Crumbie and Laugesen, 2004) reported the phenomenon of wall effect on the basis of particle size distribution and packing of various components of concrete against the larger solid surface as shown in Figure 2.4. According to this mechanism, the concrete grains or aggregates were having their own size and shape. When the aggregates come in contact with large solid surface (such as reinforcement bars), the aggregates would not cut their surface against the stationary and solid surface. During compaction, the large aggregates move away from the solid surface because of the shearing forces. Only smaller grains or aggregates remains near the interface. In a normal concrete, around 20–30% of the cement paste accumulates in the ITZ adjacent to the reinforcing steel bars. The cement particles in cement paste move away from the interface during compaction, due to which large amount of water accumulates at the interface. The local w/c ratio was significantly higher in the interface compared to that of bulk denser concrete. The high water content at the interface causes the porous nature of SCI.

Also, the grading of cement particles plays an important role in the process of hydration at the interface. At any given time of hydration, the reacted thickness of any cement grain is approximately the same. During the early ages of hydration, the smaller cement grains as well as the outer surface of the larger cement grains reacts first. Thus, the inner core of the larger cement grains remains unreacted and coarser. As a result of all these, the hydration products and smaller cement grains are accumulated near the steel surface and the larger anhydrous material moves away from the interface due to the wall effect. The wall effect can be reduced by varying the gradation of concrete ingredients. The addition

of finer materials such as mineral admixtures/fillers can make the ITZ denser, provided the particle size of fillers should be smaller than the cement particles (Kenny and Katz, 2015). Some of the researchers reported that the casting direction also has the impact on the porosity of SCI. For example in horizontally placed reinforcement bars (such as beams), the casting was done from the top side or in other words perpendicular to the horizontal reinforcement (T. A. Soylev and François, 2003; Horne, Richardson and Brydson, 2007).
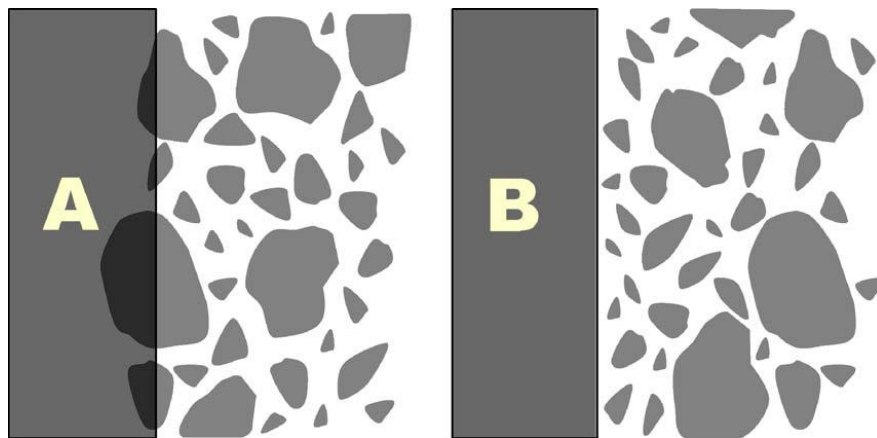
Figure 2.4: Illustration of the wall effect (Scrivener, Crumbie and Laugesen, 2004)

In such cases, bleeding occurs beneath the horizontal bars. The heavier solid particle settles downwards and the free water rises upwards during compaction. This free water moves upwards until it gets trapped below the horizontal reinforcement which ultimately becomes a void once the water evaporates (Horne, Richardson and Brydson, 2007; Kenny and Katz, 2015; Chen *et al.*, 2018). As a result of increased w/c ratio the plastic viscosity increases which enhances the bleeding and reduces the concrete quality around the bottom area of horizontal reinforcement. Some of the researchers reported that the voids or gaps were in the order of millimetres. The voids under the horizontal bars can be seen in Figure 2.5. The accumulation of bleed water on the underside of the horizontally cast reinforcement bar can be described by a mechanism proposed by Kenny and Katz (Kenny and Katz, 2015). According to this mechanism the bleed water continues to rise upwards

and accumulates under the horizontal reinforcement bar up to some extent. Then this accumulated bleed water finds a way up along the sides of the reinforcement bar by breaking the water filled zone under the steel bar as shown in Figure 2.6. This upward movement of bleed water empties the water filled void below the horizontal bar and reduces its thickness. This upward movement of bleed water continues to rise until the hydration products prevent this movement. Once the hydration products terminate the upward movement of bleed water, the final size of the void is determined, and remains unchanged after this. According to this mechanism, the void size is independent of volume of bleed water and the rheological properties of the mix like viscosity determines the void size before and after rising of water.
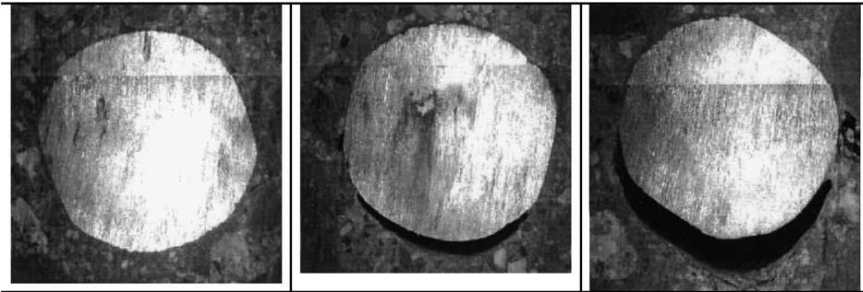
Figure 2.5: Void formation below the horizontal bars (T. A. Soylev and François, 2003)
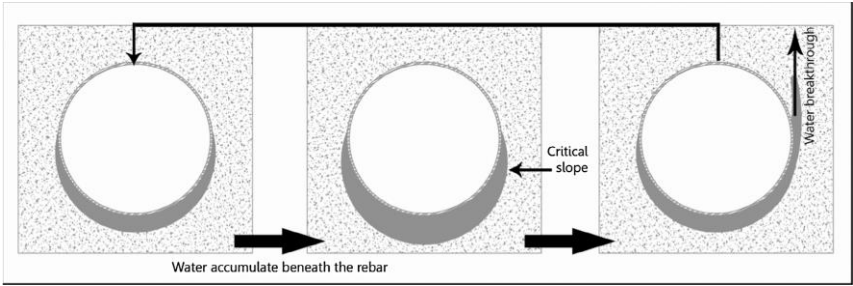
Figure 2.6: Water accumulation pattern beneath the horizontal bar (Kenny and Katz, 2015)

18

The bleeding induced voids have crescent shape or more elongated nature which helps them to gain a better contact area with the reinforcing bars compared to air voids (Angst *et al.*, 2017). Water filled in bleeding induced voids were gets emptied on drying and chemical shrinkage. Emptied bleeding induced voids can be refilled by water on wetting. Accumulation of bleed water not only exists below horizontal casted bars, but also takes place in between indentation on steel bars, under cover blocks, tie wires, reinforcement bar intersection junction in the RC (Angst *et al.*, 2017).

2.4 PROPERTIES OF THE STEEL-CONCRETE INTERFACE

As SCI is referred as a weakest zone in RC structure, their properties are ones which decides mechanical and durability properties of RC structures. With limited information, it is often assumed that SCI has a similar property as the interfacial transition zone, which is the interface between cement paste and aggregates. However, recent developments showed that the properties of SCI and ITZ of aggregate cement paste interface are different from each other (Horne, Richardson and Brydson, 2007; Kenny and Katz, 2015; Chen *et al.*, 2018). The properties of SCI that are being referred are porosity or PZT, hydration products such as calcium hydroxide, CSH and unhydrated cement particles. The variation in porosity or PZT reported by few previous researchers were reported systematically. Also, the hydration products formed at SCI are discussed.

2.4.1 Porosity

Porosity is the quality of the material being porous, or completely filled with tiny holes. It is the open empty spaces between grains or trapped in grains in a microstructure. The occurrence of small tiny openings or spaces within a material is known as porosity. Porosity has a much higher importance in the case of SCI as it is regarded the weakest zone in RC structure.

Porosity in SCI arises due to the bleeding induced defects, shrinkage and poor packing of cement grains against the reinforcing steel bars (T. A. Soylev and François, 2003; Horne, Richardson and Brydson, 2007; Ryou and Ann, 2008). The packing of cement grains

during the early ages of cement hydration leaves more porous zone around the reinforcing steel. Hydration products that precipitates within the porous zone is calcium hydroxide, which tends to fill the voids in the porous zone and reduces porosity (T. A. Soylev and François, 2003; Liao *et al.*, 2004). But even in later stages of hydration, the porosity in the ITZ is still significantly more than bulk denser concrete (Basheer, Basheer and Long, 2005) which is mainly due to the wall effect and bleeding induced defects (Horne, Richardson and Brydson, 2007). Due to the wall effect, smaller grains are accumulated at SCI. During the first day of hydration, porosity at SCI is about 85% more than that of bulk denser concrete. The porosity reduced as hydration proceeds during later ages, the percentage reduction in porosity is same in both SCI and bulk denser concrete due to preferential precipitation (Liao *et al.*, 2004). Around the vertically cast reinforcement bars and the topside of the horizontally cast reinforcement bar, the precipitation of $Ca(OH)_2$ was found to be 5 μm distant from the steel surface, whereas 40 μm distant porous zone was found in the underside of the horizontal reinforcement bar (Horne, Richardson and Brydson, 2007). Thus the voids which remain unfilled became a permanently porous region which contributes in corrosion initiation and reducing mechanical and durability properties of concrete (Horne, Richardson and Brydson, 2007).

The orientation of reinforcement of bars such as vertically cast (columns) and horizontally cast (beams) members also has the influence on porosity of SCI. The ITZ properties around horizontally cast members and vertically cast members are not the same (Horne, Richardson and Brydson, 2007; Kenny and Katz, 2015). A uniform and dense concrete (less porous) is usually found around the vertically cast members. Whereas in the case of horizontally cast members, two different zones namely upper and lower zones exist. The upper zone occurs above the reinforcement bar which is quite denser and similar to the ITZ properties around the vertically cast reinforcement bar. The lower zone occurs on the underside of the reinforcement bar which is more porous and has very low density (Horne, Richardson and Brydson, 2007; Kenny and Katz, 2015; Angst *et al.*, 2017). Usually a circumferential void is formed underneath the bottom half of the steel reinforcement bar that largely affects the durability properties of SCI [7].

20

The w/c ratio of the mix also determines the extent of porosity at SCI. The porosity of SCI increases with increase in w/c ratio (Horne, Richardson and Brydson, 2007; Ryou and Ann, 2008; Chen *et al.*, 2018). For a concrete of 0.49 w/c ratio, the porosity at SCI was approximately 30%, whereas, in case of bulk concrete, approximately 8% porosity was found after first day of hydration. Even after 7 days of hydration, the porosity adjacent to steel was more than the bulk concrete (Horne, Richardson and Brydson, 2007). For a concrete of 0.7 w/c ratio, the porosity at SCI was approximately 50% and at the same time porosity of bulk concrete was 12%. Similar kind of observations on the effect of w/c ratio was reported by several researchers (Kenny and Katz, 2015; Chen *et al.*, 2018). The porosity of SCI is usually about twice or thrice the porosity of bulk denser concrete (Basheer, Basheer and Long, 2005).

Few researchers have experimentally determined the percentage porosity at SCI and are presented in Table 2.1. The effect of w/c ratio and effect of supplementary cementitious material (SCM) on the porosity of SCI can be understood from Table 2.1.

The percentage porosity at SCI and w/c ratio is directly proportional, as the w/c ratio increases porosity at SCI also increases. It can be observed that the top side of horizontally cast reinforcement bars and vertically cast reinforcement shows similar porosity values at SCI. Significant variation of percentage porosity was noticed for the bottom side of horizontally cast reinforcement bars. Kenny and Katz (Kenny and Katz, 2015) reported that the porosity found beneath all horizontal reinforcement bar was 1.0 or very close to this value only mixes with a w/c of 0.52 and higher powder contents had a somewhat lower porosity of 0.8–0.9. The porosity above horizontal reinforcement bars and around vertical reinforcement bars ranged from 0.15 to 0.52 and from 0.24 to 0.46, respectively. The SEM images showed 0.5 mm – 2 mm voids below the horizontally cast reinforcement bars.

Few researchers reported the effect of addition of SEM's on the percentage porosity of SCI. These reported values of SEM's on the porosity of SCI may not be conclusive, as very few reported findings were available. A systematic approach on the effect of SEM's on the properties of SCI is missing in the literature. Due to the addition of SCM's,

significant reduction in percentage porosity was noticed at SCI (Zayed, 1991; T. A. Soylev and François, 2003). The pozzolanic reaction due to the addition of SEM's was predicted to be the reason for reduced percentage porosity at SCI (Zayed, 1991).

Table 2.1: Compiled literature data on percentage porosity at SCI

Reference	w/c ratio	Filler/SCM	Filler/SCM (%)	Porosity at SCI (%)		
				Horizontal (Top)	Horizontal (Bottom)	Vertical
(Zayed, 1991)	0.45	-	-	30	-	22
	0.45	Silica Fume	10%	19	-	08
(T. A. Soylev and François, 2003)	0.75	-	-	19	-	-
	0.53	-	-	16	-	-
	0.6	Limestone filler	140	16.5	-	-
	0.39	-	-	15	-	-
	0.39	Silica Fume	30	10	-	-
(Horne, Richardson and Brydson, 2007)	0.49	-	-	5	45	7
	0.7	-	-	9	85	23
(Kenny and Katz, 2015)	0.4	Powdered CaCO$_3$	0	0.48	1	0.34
	0.44		0	0.16	0.96	0.46
	0.45		4	0.52	0.96	0.4
	0.45		8	0.39	1	0.41

Reference	w/c ratio	Filler/SCM	Filler/SCM (%)	Porosity at SCI (%)		
				Horizontal (Top)	Horizontal (Bottom)	Vertical
(Kenny and Katz, 2015)	0.45		12	0.23	1	0.24
	0.45		16	0.29	0.99	0.31
	0.45		20	0.49	1	0.28
	0.47		0	0.15	1	0.35
	0.52		8	0.21	0.97	0.46
	0.52		12	0.22	0.8	0.35
	0.52		17	0.2	0.92	0.36
	0.55		0	0.21	0.99	0.3
	0.6		0	-	-	0.33
	0.65		0	0.15	0.9	0.3

-SCM – supplementary cementitious material, w/c – water to cement ratio

The percentage porosity at SCI and w/c ratio is directly proportional, as the w/c ratio increases porosity at SCI also increases. It can be observed that the top side of horizontally cast reinforcement bars and vertically cast reinforcement shows similar porosity values at SCI. Significant variation of percentage porosity was noticed for the bottom side of horizontally cast reinforcement bars. Kenny and Katz (Kenny and Katz, 2015) reported that the porosity found beneath all horizontal reinforcement bar was 1.0 or very close to this value only mixes with a w/c of 0.52 and higher powder contents had a somewhat lower porosity of 0.8 – 0.9. The porosity above horizontal reinforcement bars and around vertical reinforcement bars ranged from 0.15 to 0.52 and from 0.24 to 0.46, respectively. The SEM images showed 0.5 mm – 2 mm voids below the horizontally cast reinforcement bars.

Few researchers reported the effect of addition of SEM's on the percentage porosity of SCI. These reported values of SEM's on the porosity of SCI may not be conclusive, as very few reported findings were available. A systematic approach on the effect of SEM's on the properties of SCI is missing in the literature. Due to the addition of SCM's, significant reduction in percentage porosity was noticed at SCI (Zayed, 1991; T. A. Soylev and François, 2003). The pozzolanic reaction due to the addition of SEM's was predicted to be the reason for reduced percentage porosity at SCI (Zayed, 1991).

Ann and Song (2007) investigated the chloride threshold levels of reinforcement corrosion in RC. The importance of chloride threshold level measurement, influencing factors and their representation were discussed. It was reported that the amount of entrapped air void content at SCI was a dominating factor in measuring the chloride threshold value. The authors also reported that SCI defects such as entrapped air voids were the true reason for corrosion initiation. Authors interpreted that as the air voids content increases at SCI, chloride threshold level decreases significantly. The authors reported a graph, which represents dependency of chloride threshold with the amount of interfacial air voids (or porosity) in the vicinity of SCI as represented in Figure 2.7.
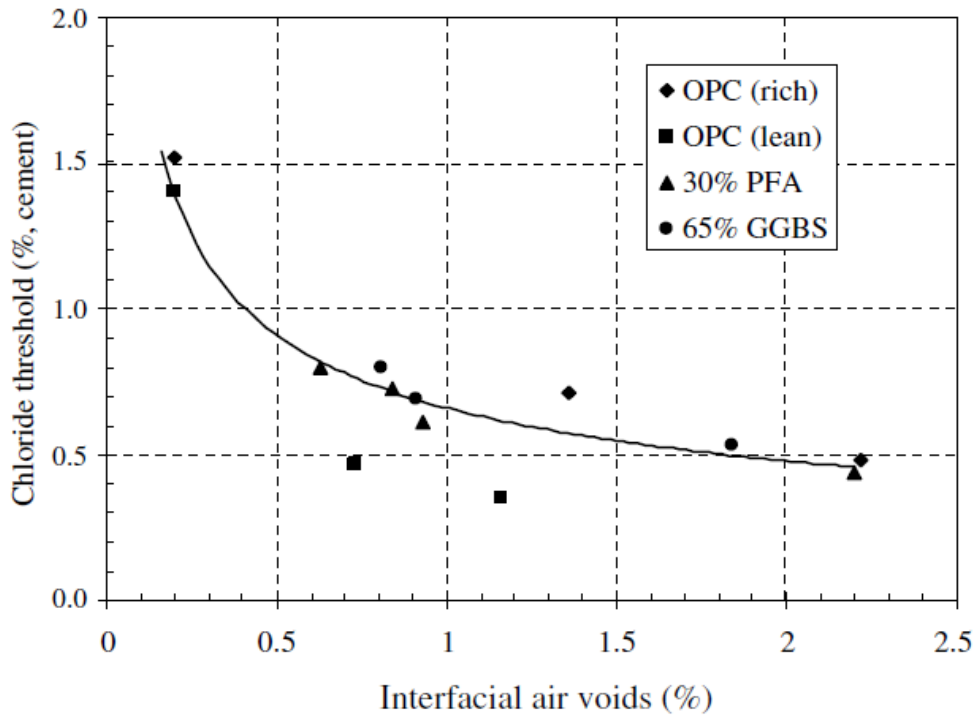
Figure 2.7: Relationship between the air voids (or porosity) at SCI and the chloride threshold for OPC, 30% PFA and 65% GGBS concretes (Ann and Song 2007).

2.4.2 Porous zone thickness at the steel-concrete interface

Some of the researchers reported the porosity at SCI in terms of PZT. The PZT was considered as an influencing and important parameter in service life prediction models (Liu, 1996a; Thoft-Christensen, 2000; Bhargava *et al.*, 2005; El Maaddawy and Soudki, 2007; Goudar, Bibhuti Bhusan Das and Arya, 2019). Few researchers assumed the PZT while predicting the service life of structures in service life prediction models without any experimental investigations (Liu, 1996a; Petre-Lazar and Gérard, 2000). Thoft-Christensen (2000) suggested that the thickness of porous zone was in the range of 10 to 20 μm and assumed 12.5 μm PZT for the service life prediction through mathematical modeling. Liu (1996) also developed a mathematical model for the service life prediction of a structure by assuming 12.5 μm of PZT at SCI. Assuming the PZT without experimental investigation may lead to the misinterpretation of service life of structures.

Due to the developments in microstructure study of SCI, several researchers experimentally measured the PZT at SCI. Horne et al. (Horne, Richardson and Brydson, 2007) measured the PZT at SCI by doing image analysis of BSE images. Only two locations, the top and bottom sides of the steel, are quantitatively analysed in their study. One or two locations around SCI were measured by other researchers also (Zayed, 1991; T. A. Soylev and François, 2003; Yuan and Ji, 2009). This appears to be inadequate to represent the whole SCI around the steel bar. A thorough quantitative measurement should be conducted for the entire interface area around the steel. Only two researchers Chen *et al.* (2018) and Kenny and Katz (2015) measured the PZT all around SCI which helps to understand the variation in PZT around the entire interface. This kind of measurement of PZT all around SCI is need of the hour. In this regard, few researchers have experimentally determined the PZT at SCI and the same data is compiled and are presented in Table 2.2. The effect of w/c ratio and effect of supplementary cementitious material (SCM) on the PZT of SCI can be understood.

Table 2.2: Compiled literature data on porous zone thickness at SCI

Reference	w/c ratio	Filler/SCM	Filler/SCM (%)	PZT (µm)		
				Horizontal Top (H-Top)	Horizontal Bottom H-Bottom)	Vertical
(Zayed, 1991)	0.45	-	-	50	50	50
	0.45	Silica fume	10	35	35	40
(Zhu and Bartos, 1997)	0.35	-	-	10	50	15
(Liu, 1996a)	0.35	-	-	12.5	12.5	12.5
(Thoft-Christensen, 2000)	0.35	-	-	10	10	10
	0.4	-	-	20	20	20
(Zhu and Bartos, 2000)	0.43	-	-	35	60	-
	0.36	GGBS	60	30	50	-
(Zhu, Sonebi and Bartos, 2004a)	0.36	GGBS	60	30	50	-
	0.68	-	-	40	70	-

Reference	w/c ratio	Filler/SCM	Filler/SCM (%)	PZT (µm)		
				Horizontal Top (H-Top)	Horizontal Bottom H-Bottom)	Vertical
(Horne, Richardson and Brydson, 2007)	0.49	-	-	15	65	20
	0.7	-	-	25	165	35
(Mondal, Shah and Marks, 2008)	0.35	-	-	20	20	20
	0.5	-	-	100	100	100
(Wang *et al.*, 2009)	0.3	Silica fume	10	80	95	87
	0.3	-	0	90	105	98
	0.5	-	0	107	125	114
(Yuan and Ji, 2009)	0.6	-	-	87	104	95
(Angst *et al.*, 2017)	0.55	-	-	-	140	-
	0.6	-	-	-	150	-
('Biniam_Thesi	0.4	-	-	17	44	18

Reference	w/c ratio	Filler/SCM	Filler/SCM (%)	PZT (µm)		
				Horizontal Top (H-Top)	Horizontal Bottom H-Bottom)	Vertical
s_Nov_30 (44)', no date)	0.5	-	-	20	69	21
(Zhao, Wu and Jin, 2013)	0.44	-	-	65	118	-
(Kenny and Katz, 2015)	0.40	Powdered CaCO₃	0	30	268	112
	0.44		0	45	280	79
	0.45		4	88	245	89
	0.45		8	129	299	113
	0.45		12	114	311	136
	0.45		16	74	287	84
	0.45		20	87	304	76
	0.47		0	94	320	109

Reference	w/c ratio	Filler/SCM	Filler/SCM (%)	PZT (μm)		
				Horizontal Top (H-Top)	Horizontal Bottom H-Bottom)	Vertical
	0.52		8	81	288	135
	0.52		12	77	226	118
	0.52		17	85	186	85
	0.55		0	104	264	117
	0.6		0			88
	0.65		0	54	296	110
(Chen *et al.*, 2018)	0.5	-	-	21.5	37	-
	0.45	-	-	10	19	-
	0.4	-	-	9.5	15	-
(Zacharda, Štemberk and Němeček, 2018)	0.4	-	-	40	40	40

-SCM – supplementary cementitious material, w/c – water to cement ratio, PZT - porous zone thickness

2.4.2.1 Influence of w/c ratio on the porous zone thickness of SCI

The orientation of reinforcement bar also plays an important role in analysing the PZT at SCI. The PZT of vertically cast members and horizontally cast members varies significantly. There are two distinct zones for horizontally cast members, namely, horizontal top (H-Top) and horizontal bottom (H-Bottom). The variation in PZT with respect to w/c ratio of horizontal top and horizontal bottom as reported by research fraternity is presented in Figure 2.8 and Figure 2.9, respectively. The variation in PZT with respect to w/c ratio of vertically cast members is presented in Figure 2.10. The data of PZT and w/c ratio in Figure 2.8, Figure 2.9 and Figure 2.10 were extracted from Table 2.2.
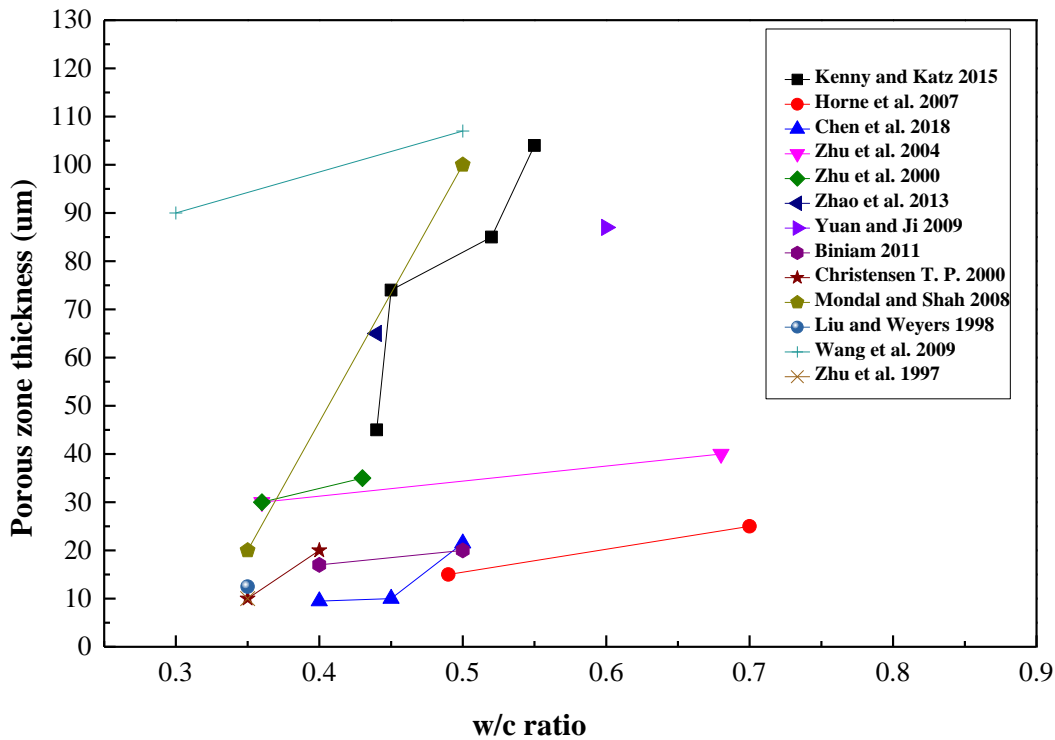
Figure 2.8: Variation in the porous zone thickness and w/c ratio of top side of horizontally cast reinforcement bar (H-Top)
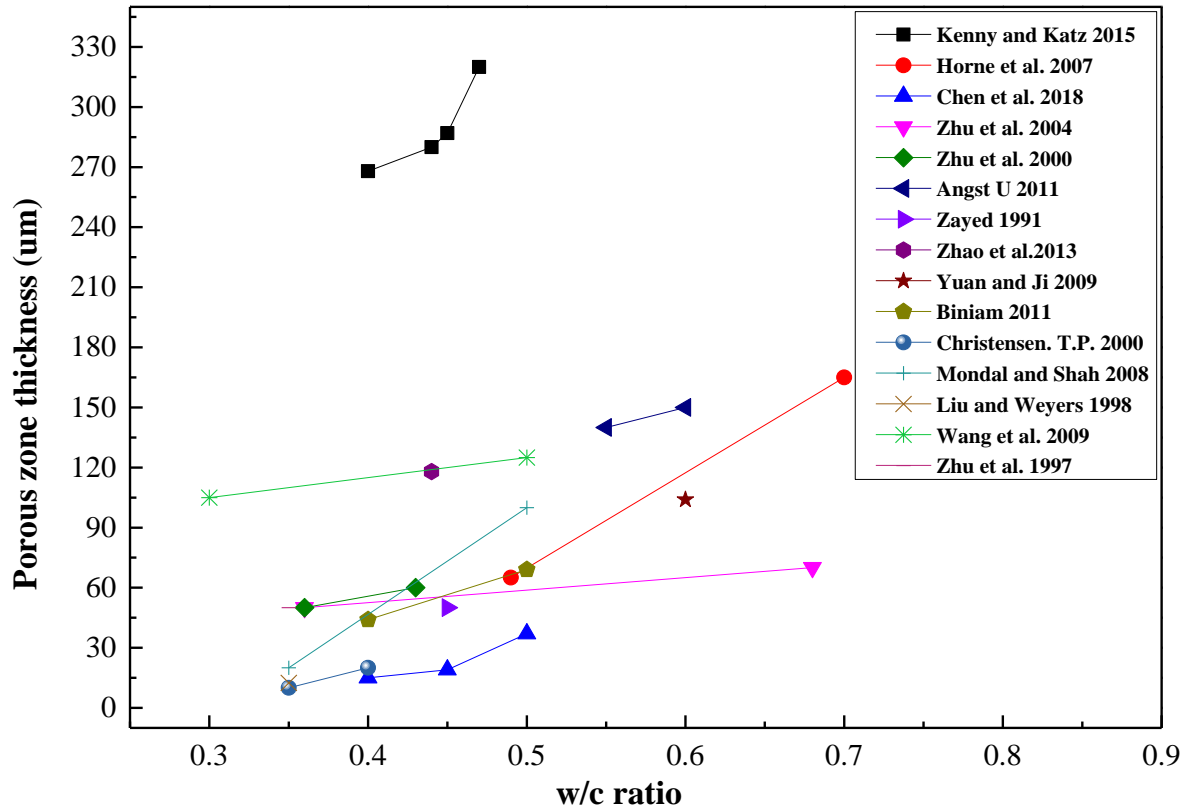
Figure 2.9: Variation in the porous zone thickness and w/c ratio of bottom side of horizontally cast reinforcement bar (H-Bottom)

It is difficult to come to a common conclusion as different researchers reported different values of PZT for similar w/c ratio. Leaving some extreme values, it can be noticed that w/c ratio and PZT are directly correlated. PZT at SCI increases as w/c ratio increases. In most of the observations, the PZT around the vertically cast reinforcement bar and above the horizontally cast reinforcement bar shows almost similar values. The bottom side of horizontally cast reinforcement bar has PZT in the order of several hundred micrometres to few millimetres range.

2.4.2.2 Influence of adding supplementary cementitious materials (SCM) or fillers on porous zone thickness

The beneficial effects of adding supplementary cementitious materials (SCM) or fillers on the microstructure properties of bulk concrete were known to us. The SCM's also displayed reduction in porosity of ITZ between aggregate cement paste interfaces (Scrivener, Crumbie and Laugesen, 2004). However, very few articles were reported the effect of SCM's on the properties of SCI especially the PZT. It can be observed from Table 2.2 that addition of SCM slightly reduces the PZT at SCI, irrespective of reinforcement bar orientation in the RC. However, the bottom side of horizontally cast reinforcement bars showed least reduction in PZT due to the addition of SCM's. It was also noticed that higher dosage of SCM's/filler has better effect towards the reduction in PZT of SCI. Very limited amount of literature is available where the effect of SCM's on PZT of SCI was analysed. A detailed and systematic analysis of effect of SCM's on the properties of SCI is required.
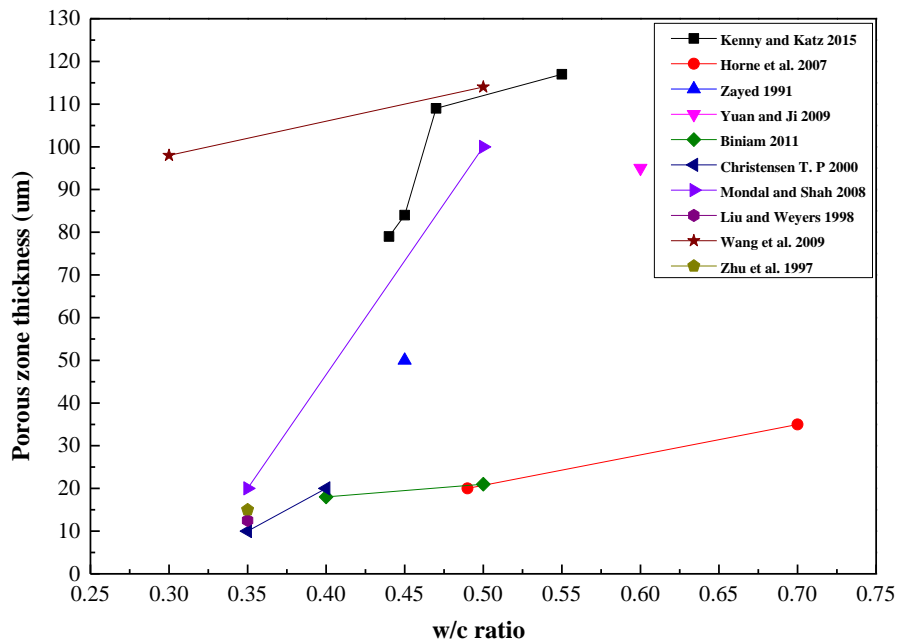
Figure 2.10: Variation in the porous zone thickness and w/c ratio of vertically cast reinforcement bar

2.5 METHODS AND TECHNIQUES FOR DETERMINATION OF ENGINEERING PROPERTIES OF STEEL-CONCRETE INTERFACE

2.5.1 Bond strength

The bond strength of RC is an indirect representation of properties at SCI (Turk, Karatas and Ulucan, 2010; Yalciner, Eren and Sensoy, 2012; Kenny and Katz, 2015). The physical properties of SCI definitely influence the bond strength properties in RC (Castel *et al.*, 2003; Soylev and Franc, 2003; Fang *et al.*, 2006). It is important to explore the relationship between bond strength and properties of SCI, the publications which investigate both are rare.

Numerous amount of literature is available which deal with relationship between pullout test and concrete and rebar properties, but not with respect to properties of SCI (Ji and Song, 2008; Novidis and Pantazopoulou, 2008; Xu and Wang, 2008). When both pullout strength and SCI properties were examined, no relationship between the two was established (Zhu, Sonebi and Bartos, 2004b). The correlation between the pullout strength and PZT of SCI analyzed by Kenny and Katz (2010), reported that the PZT at SCI for vertically cast rebars was 40 μm and horizontally cast members was 400 μm, which significantly influenced the pullout strength. The maximum stress during pullout test was negatively correlated with the PZT at SCI. Similar observations were reported by other researchers also (Soylev and Franc, 2003; Horne, Richardson and Brydson, 2007; Wong *et al.*, 2010). However, PZT is not the sole influencing parameter, the other hydration products such as variation in calcium hydroxide around SCI will also affect the bond strength properties. With respect to time there are no significant changes in the PZT of SCI (Horne, Richardson and Brydson, 2007), however, the hydration products such as calcium hydroxide and other hydration products change with respect to curing time.

Turk, Karatas and Ulucan (2010) analyzed bond strength of nine different types of concrete, normal concrete and eight types of self-compacting concretes (SCC). The OPC was incorporated with different dosages of class F fly ash and silica fume. The authors

observed that type and dosage of mineral additions had an important effect on the bond strength of steel bars embedded in SCC. It was reported that the SCC samples with 10% silica fume had the highest average bond strength with 7.05 MPa followed by the SCC samples with 30% fly ash with 6.93 MPa. Also, it was reported that the bond strengths of the beam specimens made with SCC was generally higher than that of the beam specimens made with normal concrete. The reason can be attributed to SCC including high volume fine grains in comparison to normal concrete, which covered reinforcements more effectively. Also, the accumulation of bleed water under horizontally positioned bars reduced, as a result of the increasing volume fraction of fine materials.

Bond behavior of RC produced from powder type SCC were analyzed by Pop *et al.* (2013) and authors reported that cube samples were cast by using two vibrated concretes and four self-compacting mixes. The authors examined parameters such as cement/limestone ratio, effect of rebar diameter and effect of the embedded length of rebars. It was reported that SCC (50 MPa compressive strength) has provided higher ultimate and characteristic bond strengths compared to vibrated concretes. As the compressive strength both SCC and vibrated concretes reached a value of 70 MPa, authors did not find any significant differences in the bond strength of both the concretes. However, the authors mentioned that for the equivalent slip of 0.01 mm the bond strength of SCC was superior to vibrated concrete. It was reported that embedment length of reinforcement bars had an effect on the bond strength of both the concretes. As the embedment length of reinforcement bars increased the bond strength reduced for both the concretes. Bond strength seems to have a linear co-relation with the reinforcement bar diameter. The SCC had shown an increase in bond strength as bar diameter increased and slightly smaller decreased values were observed for vibrated concrete. Fang *et al.* (2006) reports the bond strength variation in RC for different corrosion levels. The bond strength values calculated by pull out tests were compared with the results obtained from finite element analysis (FEA). For accelerating the corrosion process an electrolyte corrosion technique was employed. The authors reported that a corrosion level of 4% had negligible effect on the ultimate bond strength of confined deformed bars. As the corrosion level

increased from 4% to 6% the authors observed a substantial reduction in bond strength. For similar corrosion level (4 - 6%), the FEA results and experimental results of unconfined steel had shown 30 – 65% lesser bond strength in comparison with confined steel bars. The FEA assumed that corrosion products behaved as a granular material which illustrated a convincingly better agreement with the experimental results concerning bond strength and bond stiffness.

Fang *et al.* (2004) investigated the significance of corrosion on bond strength of rebars in RC. The corrosion levels of 0% to 9% were considered to analyze the effect of different corrosion levels on bond strength and bond slip behavior. With series of test results the authors conformed that bond strength of reinforcement bars without confinement were really sensitive to corrosion levels and usually declined with the increased corrosion level. However, at 9% corrosion level the bond strength was only one third of that of non-corroded samples reported by authors. It was observed by the authors that, effect of corrosion had less significance on the bond strength of reinforcement bars with confinement. It was also reported that up to a corrosion level of 5%, the bond strength of reinforcement bars was reported to be increased. Arel and Yazıcı (2012) studied the significance of curing time, depth of concrete cover and various compressive strength levels on the bond strength of RC. The reinforcement bars of 14 mm were used and the concrete cover up to a depth of 70 mm was considered. It was reported that as the depth of concrete cover increases, the bond strength of reinforcement bars were increased. The compressive strength had a major influence on the bond strength of reinforcement bars. Maximum bond strength values were reported for concrete samples which had higher compressive strengths (75.4 MPa) and vice versa for lower compressive strength (13.4 MPa) concrete samples. And also, as the concrete cover depth increases the bond strength seemed to increase considerably for the concrete samples which had higher compressive strengths. The pulls out strength of RC were mathematically modeled considering mechanical properties, concrete cover thickness and different curing times. The bond strength values measured with the proposed mathematical model were almost similar with the experimentally calculated values.

Yalciner, Eren and Sensoy (2012) investigated the consequence of corrosion on the bond strength of RC. The SCC and normal vibrated concretes with three concrete cover depths (25, 40 and 70 mm) were considered for the bond strength analysis. An empirical model was developed by incorporating the results of pull out tests. It was reported that rebars were corroded by employing an accelerated corrosion process. The mass loss of rebars was measured after the corrosion process. For various corrosion levels bond-slip relationships were evaluated. It was reported that the bond strength of non-corroded RC samples varied from that of corroded samples. The brittleness of corrosion products in corroded samples caused a sudden loss of bond strength. Corrosion effect in high strength concrete significantly reduced the bond strength because the concrete started cracking during pull out tests.

In order to carry out non-destructive monitoring, the piezoceramic (PZT) sensors were incorporated in to the concrete by bonding the sensors to reinforcing bars (Tawie and Lee, 2010). These advanced sensors indicate the bond development between concrete and steel. The bond development between rebar and concrete was monitored by EIS technique. The advantage of EIS technique was that early age characteristics of steel-concrete bond can be evaluated non-destructively. The results revealed that early age improvement of bonding between steel rebar and concrete were affected by various factors. The development of frequency shifts of the PZT, used as an indicator of bond development during curing, shows a good agreement with varying w/c ratios. It was reported that RC with high w/c ratios would likely to gain lower bonding strength than low w/c ratio due to the loose microstructure at SCI. The authors commented that lower rate of frequency shift may suggest that bond development is progressing slowly and one of the reasons could be due to low curing temperature. Finally, the lower amount of frequency shifts by the poor compacted specimen compared to the fully compacted specimen demonstrated that poor compaction may result in lack of bonding across the interface between steel rebar and concrete.

2.5.1.1 Effect of corrosion level on bond strength of reinforced concrete.

The bond strength and corrosion of reinforcing steel has peculiar relation. Some of the authors reported that corrosion of a limited degree increased the bond strength of RC. However, it was also reported that bond strength significantly reduced as the corrosion level increased from certain level. The data reported by several researchers is compiled and effect of corrosion level on bond strength of RC is presented in Figure 2.11. The possible explanation for increased bond strength at the initial level of corrosion is due to the accumulation of corrosion products at SCI, which reduces the porosity and increases the friction while pullout test, hence bond strength increases. As the corrosion level increases, the corrosion products at SCI starts exerting the expansive pressure and corrosion cracks will be generated, which ultimately reduces the bond strength significantly.
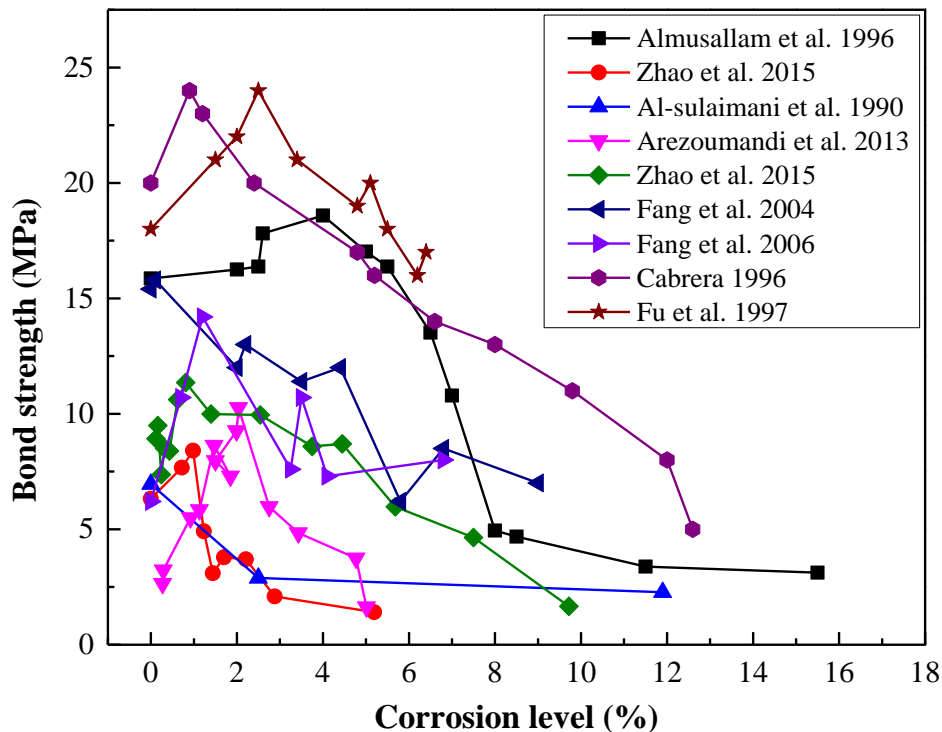
Figure 2.11: Effect of corrosion level on bond strength of reinforced concrete.

2.5.2 Scanning electron microscope (SEM)

Scanning electron microscope is a commonly used technique for characterizing and measuring the engineering properties of SCI. SEM is a powerful tool, with the help of which microstructure of the material can be accurately interpreted by magnifying it to micro to the nanometer scale. The thickness of porous zone, an important parameter which clearly distinguishes the interfacial transition zone from concrete and steel, can be measured and interpreted with the help of SEM. Yuan and Ji (2009) investigated the corrosion properties of steel bars in reinforced concrete which were corroded in chloride environment. Also, the authors studied the microstructure of steel-concrete interface and propagation of the rust layer between the interface of concrete and steel bar. Authors used digital optical microscope and SEM, in order to investigate the distribution of the rust layer along the boundary of reinforcement bars. The interface along the periphery of the reinforcement bar was measured at different regions as shown in Figure 2.12.
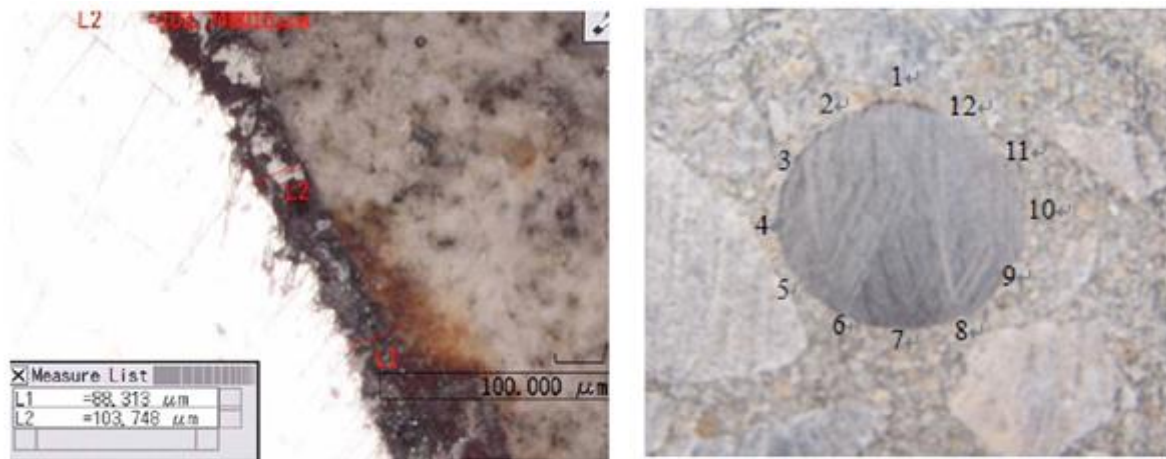
Figure 2.12: Measuring the thickness of corrosion products layer and regions arrangement along circumference (Yuan and Ji 2009).

It was reported that interfacial transition zone (ITZ) linking steel bar and cement paste had remarkable high porosity and offered space for the extension of the corrosion products (shown in Figure 2.13). The authors reported that porous zone thickness at steel-

concrete interface varies from point to point along the periphery of the steel bar and the average thickness of this porous layer varies from 80-103 μm.
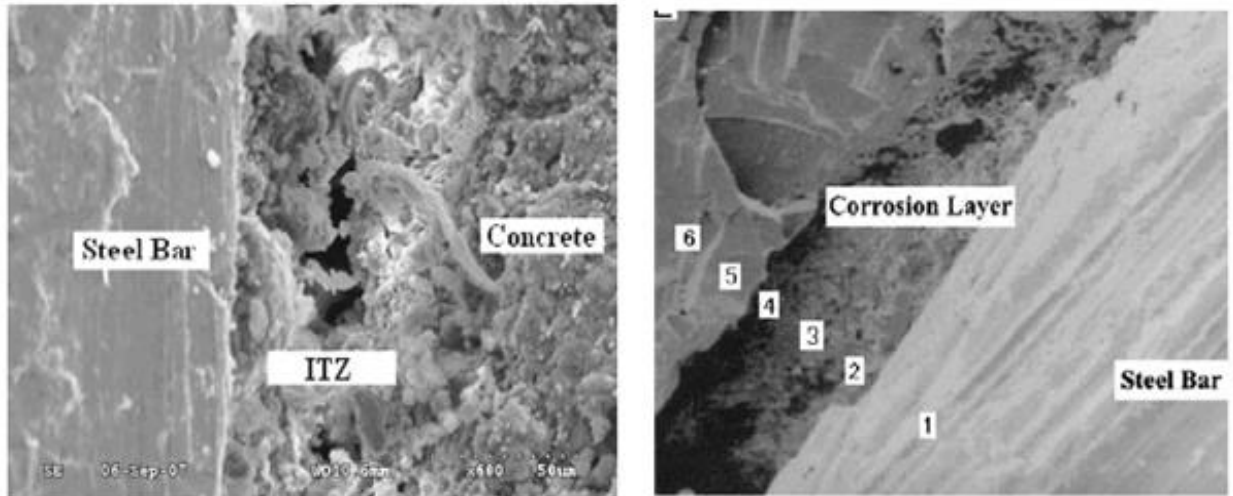
Figure 2.13: ITZ between steel bar and concrete which was filled by corrosion products after corrosion (Yuan and Ji 2009)

The authors reported that the ITZ between un-corroded steel bar and concrete showed characteristic of high porosity. Authors also explored that at some point in the corrosion process the rust layer spread in to the ITZ, and the ITZ will be converted in to rust layer consisting of cement paste and corrosion products. Once the corrosion products reach the solid concrete surface, the expansive pressure will be developed.

Zhao, Wu and Jin, (2013) investigated a 2 years deteriorated reinforced concrete specimen in chloride environment. Corrosion induced cracks and steel-concrete interface were observed by SEM to examine the effect of mill scale on the steel surface and the allocation of corrosion products. The sample prepared for SEM investigation is presented in 2.14.
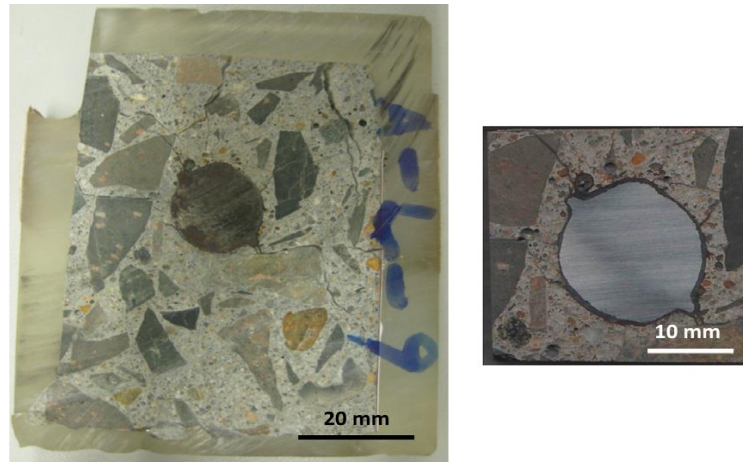
Figure 2.14: Sample prepared for SEM investigation (Zhao, Wu and Jin, 2013).

The authors reported that the distribution of O and Fe along the steel-concrete interface was explored by Energy dispersive spectrum analysis (EDS) across an analytical line, as reported in Figure 2.15 (a) and (b). The vertical axis corresponds to the photoelectrons/second, representing the contents of O and Fe, and the horizontal axis corresponds to the distance along the analytical line. From the reported results in energy dispersive spectrum analysis it is to be observed that there are distinctly five areas available along the analytical line. These are steel, corrosion layer, millscale, corrosion filled paste and concrete. The thickness of millscale was measured approximately at 80 locations around the corroded steel bar, and the mean value of millscale thickness ranged from 24-27 µm for each sample. It was reported that type of reinforcement bar and its manufacturing process had an effect on the thickness of the millscale. For example, in the author's earlier study (Zhao, Wu and Jin, 2013), the millscale of plane reinforcement bar implanted in concrete had the millscale thickness of 34.5 µm, which varied from the millscale thickness (24-27 µm) calculated by Zhao, Wu and Jin, (2013). The EDS analysis graph of steel-concrete interface clearly indicates that the porous zone thickness between steel and concrete varies from 150-195 µm.
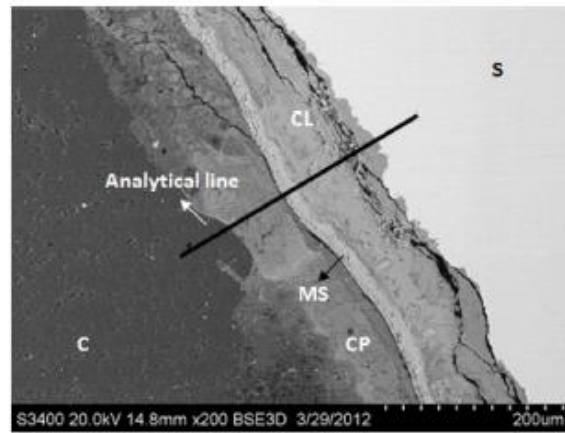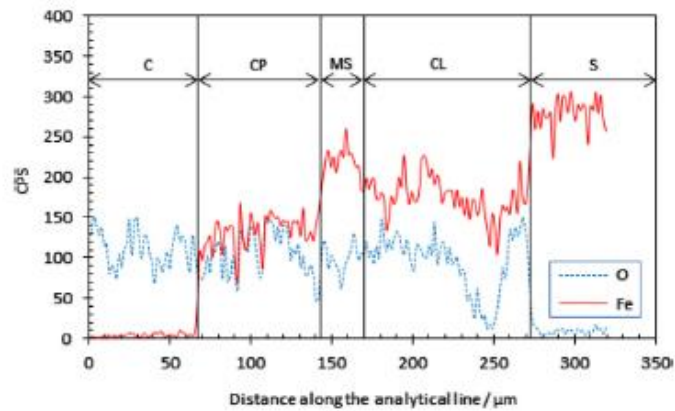
Figure 2.15: Rust distributions at steel/concrete interface. (a) BSE image at the steel-concrete interface (C – concrete, CP - corrosion-filled paste, MS – millscale, CL - corrosion layer, S - steel) and an analytical line across the interface. (b) The distributions of Fe and O across the steel-concrete interface analyzed by EDS along the analytical line (Zhao, Wu and Jin, 2013).

Zhao, Dai and Jin, (2012) studied steel-concrete interface of concrete samples which were electrochemically corroded. The authors utilized digital microscopy for measuring the thickness of corrosion products at inner and outer cracked surface of concrete cover. The authors analyzed SCI in SEM by back scatter electron (BSE) mode which is shown in Figure 2.17 (a). The authors reported that there was a clear interface between two layers of iron oxides. The oxide layer near the steel bar appears dark, while the oxide

43

layer adjoining to concrete is somewhat brighter. From the reported results as presented in Figure 2.17 it is to be observed that there are distinctly five regions available along the analytical line. These are rebar, rust produced in accelerated corrosion process, millscale, rust contaminated concrete and concrete.
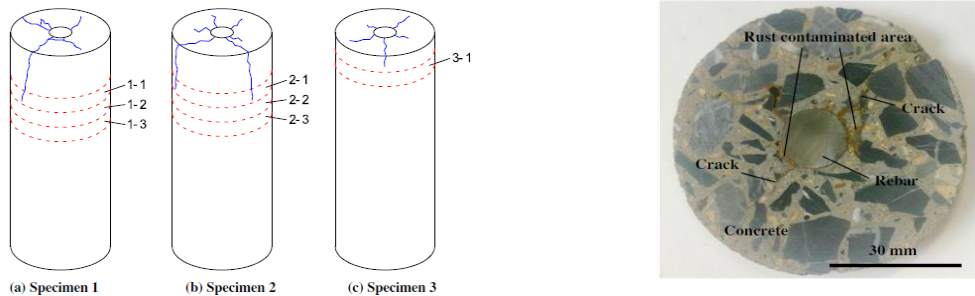
Figure 2.16: Schematic diagrams of the specimens and the location of the slices (left) and sample of slice 1-1 for digital microscope observation (right) (Zhao, Dai and Jin, 2012).
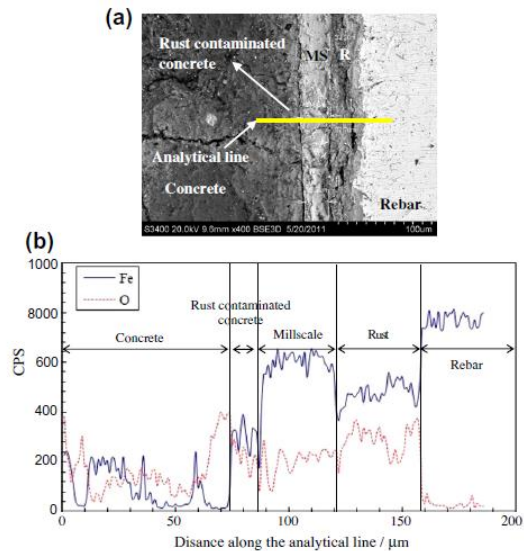
Figure 2.17: EDS analysis across the steel-concrete interface. (a) BSE image at steel-concrete interface (R – rust, MS - millscale) and an analytical line across the interface. (b) The distributions of Fe and O across the SCI analyzed by EDS along the analytical line (Zhao, Dai and Jin, 2012).

44
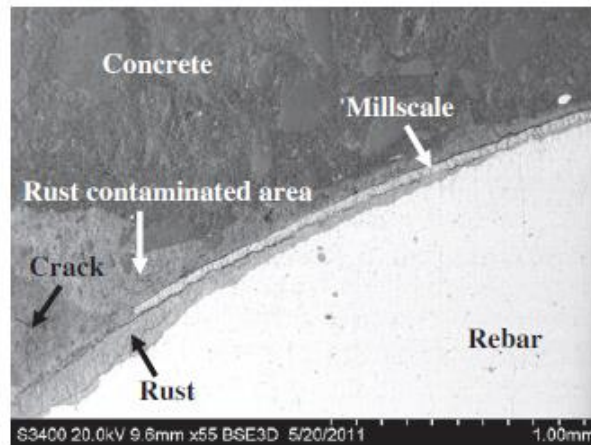
Figure 2.18: Millscale distributions at the steel-concrete interface (Zhao, Dai and Jin, 2012).

Binam (2011) investigated the causes for delamination of concrete cover in the bridge decks. The field samples were collected and cut using diamond saw cutters. Porous zone thickness between the steel rebar and concrete were measured from environmental scanning electron microscope. A representative picture reported by the author showing the porous zone thickness for the steel-concrete interface is presented in Figure 2.19.
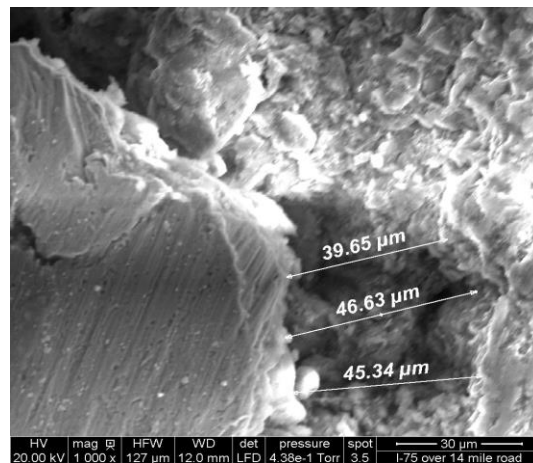
Figure 2.19: Porous zone thickness measurement of steel-concrete interface using environmental SEM.

The authors measured porous zone thickness of field collected as well as laboratory prepared samples. The porous zone thickness ranged from 17 μm to 69 μm for the laboratory tested specimens. It was also reported that higher porous zone thickness was observed for control specimen without introduced chloride, while lower porous zone thickness was observed for freeze-thaw and salt water exposed specimens with introduced chloride.

2.5.3 Energy dispersive spectroscopy (EDS)

Energy dispersive spectroscopy sometimes called energy dispersive X-ray analysis (EDAX), is an analytical technique used for the elemental analysis or chemical characterization of a sample. The EDS analysis was used to study the presence of hydration products at SCI. During the hydration of cement, the bulk concrete undergoes micro structural development by hydration products. Calcium silicate hydrate gel (C-S-H gel) and calcium hydroxide denoted by $Ca(OH)_2$ or CH are the two major products that are formed (Scrivener, Crumbie and Laugesen, 2004; Horne, Richardson and Brydson, 2007). These two hydration products strongly determine the physical, mechanical and durability properties of concrete. The ITZ properties around the aggregates-cement paste interface, ITZ properties at SCI and bulk cement paste differs significantly due the variation in formation of hydration products (Zayed, 1991; Horne, Richardson and Brydson, 2007). Very few research articles report the variation in hydration products around SCI. Bäumel (1959), Page (1975) and Page (2009) confirmed the existence of lime rich and dense layer of calcium hydroxide at SCI. The calcium hydroxide at the vicinity of SCI is helpful in maintaining the pH value at relatively higher level which acts as physical barrier for corrosion initiation (C. L. Page, 2009).

Horne et al. (2007) studied the steel-concrete interface and also aggregate-cement paste interface using SEM in BSE mode. The variables such as w/c ratio, curing period and steel insertion direction were considered by the authors. It was reported that for vertically cast reinforcement bars a large amount of $Ca(OH)_2$, increased level of porosity and decreased level of unhydrated cement content were observed near the aggregate and steel-

cement paste interfaces than the bulk cement paste (Refer Figure 2.20). In comparison with the bulk paste, the C-S-H content was considerably less around the boundary of aggregates as well as around the steel-concrete interface. The properties of steel-concrete interface were considerably changed when the w/c ratio was altered, the CH content increased from 19% to 30% when the w/c ratio decreased from 0.7 to 0.49 respectively. It was also reported that as w/c ratio increased the porosity at steel-concrete interface also increased. The accumulation of bleed-water beneath the horizontally cast reinforcement bar was the prime reason for reduction in $Ca(OH)_2$ content and an increased porosity. The properties of the steel-concrete interface greatly varied as orientation of reinforcing bars changed.
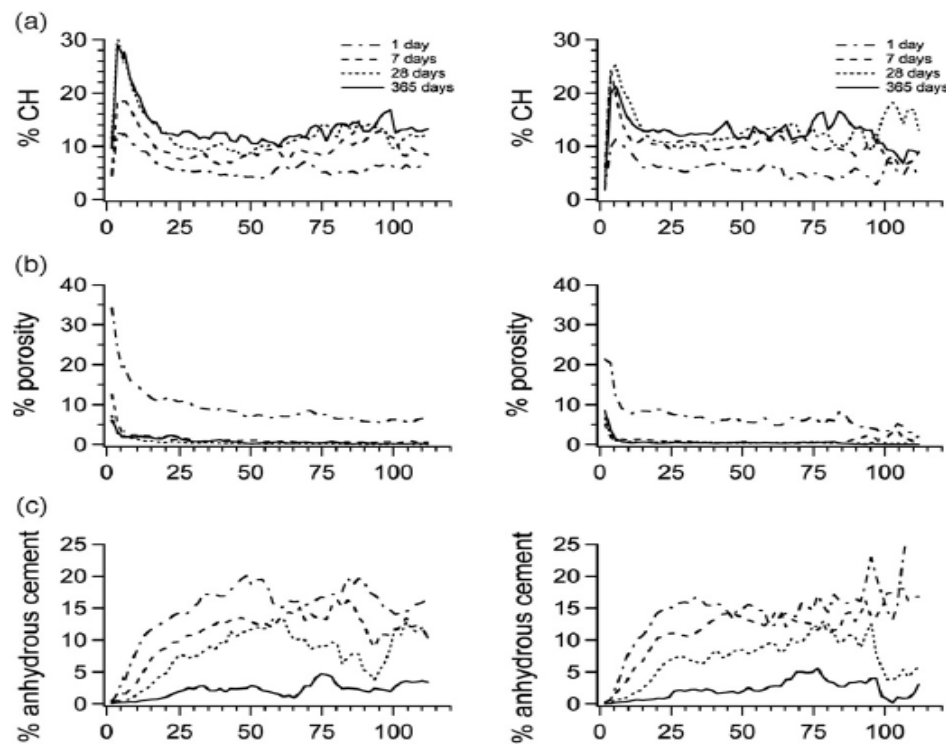
Figure 2.20: Microstructural gradients in the interfacial region between cement paste and vertically cast steel (left) and aggregate (right) at four ages in a concrete with a w/c ratio of 0.49: (a) calcium hydroxide, (b) porosity, (c) unreacted clinker phases (Horne et al. 2007).

47

The addition SCM's showed better distribution of the cement grains in addition to filling the available space between the cement grains. The calcium hydroxide distribution at SCI was significantly reduced due to the addition of silica fume (Zayed, 1991). The distribution of calcium hydroxide in plain and silica fume admixed concrete at different distances from the steel surface can be observed in Figure 2.21. For plain and silica fume concrete, the calcium hydroxide distribution profile at SCI showed the same general trends with a reduction in the amount of calcium hydroxide from 15% in plain mixes to about 5% in silica fume admixed concrete.
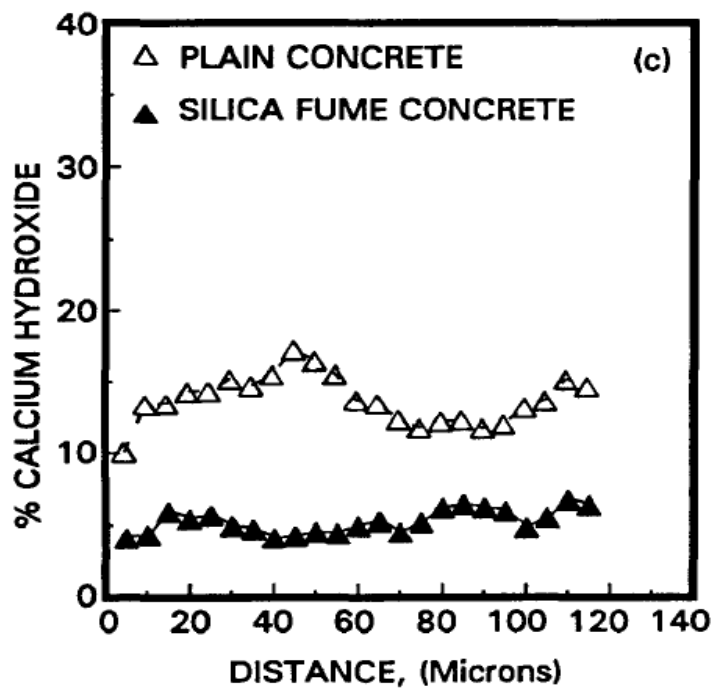
Figure 2.21: The distribution of calcium hydroxide in plain and silica fume admixed concrete at different distances from the steel surface (Zayed, 1991).

Wong et al. (2010) investigated the propagation of rust in to the ITZ and the associated damage to the steel-concrete interface. It was reported that alternate wetting (NaCl spray) and drying (40 ˚C) cycles were employed to induce various degrees of corrosion in reinforced concrete. The authors verified that rust products which were formed during

corrosion of steel in reinforced concrete had the tendency to diffuse in to the cement paste. Also, it was reported that the corrosion products have a tendency to occupy the space in the air voids near the vicinity of steel-concrete interface. Figure 2.22 and Figures 2.23 represent the SEM images in BSE mode, which clearly differentiate the boundary between the unaffected and affected paste areas. The corrosion products have diffused in to the ITZ which was recognized by higher O and Fe contents in the cement paste near the interface. Authors reported that local porosity and diffusivity were increased when calcium leaching of C-S-H gel and the dissolution of $Ca(OH)_2$ were occurred. It was also reported that the air voids in the ITZ were being filled by corrosion products. Once the entire ITZ was covered with corrosion products (rust), an expansive pressure will be generated causing bond failure and initiation of corrosion cracks. The authors interpreted that a 100 μm thick corrosion product, covering approximately about 20% of rebar perimeter was quite enough to induce visible cracks of 0.05 mm width on concrete cover.
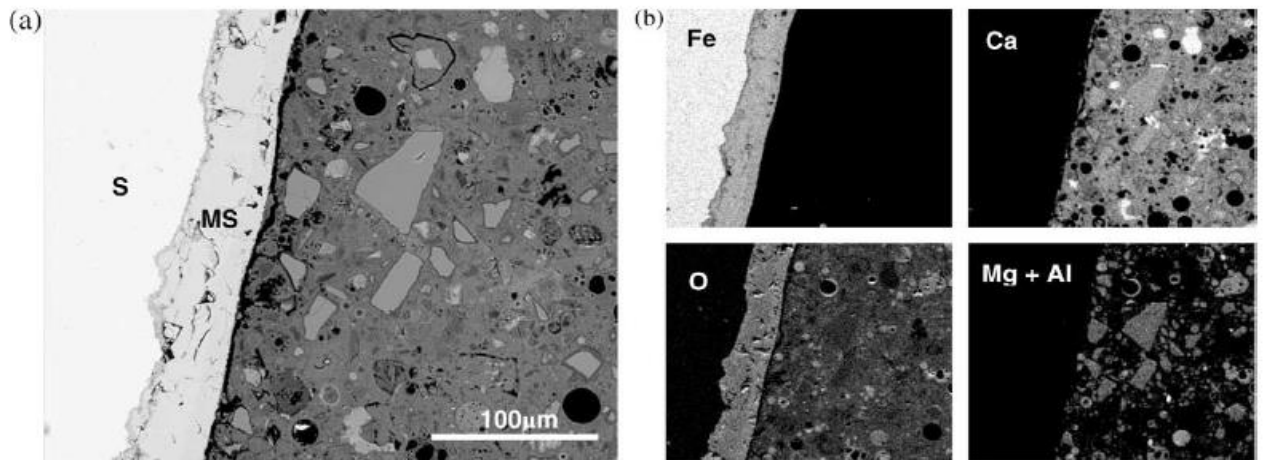
Figure 2.22: (a) BSE image and (b) EDS element maps of SCI (S – steel, MS – millscale, field of view: 343×274 μm) (Wong *et al.*, 2010).
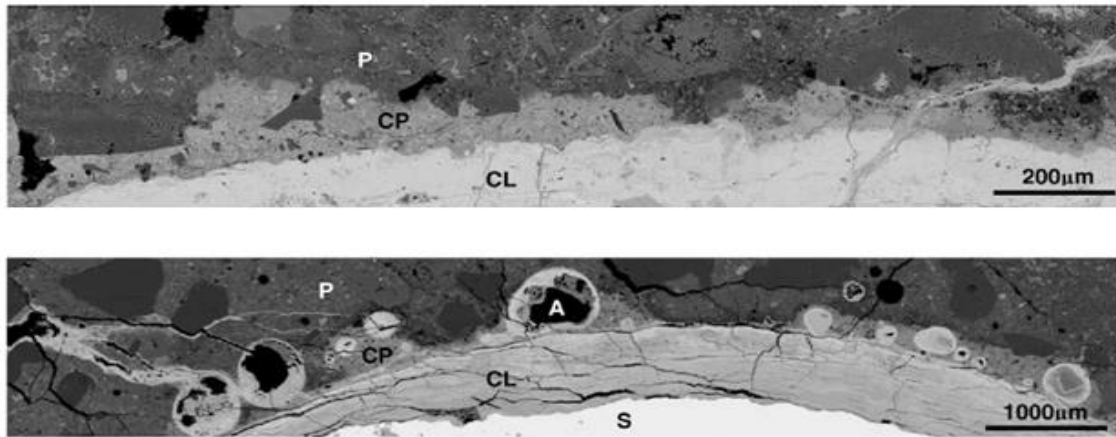
Figure 2.23: BSE images taken from normal grade concrete sample (6.81% corrosion) and high performance concrete sample (6.65% corrosion) showing accumulation of corrosion products at the steel-concrete interface and migration of corrosion products into the cement paste, air voids and cracks. (S – Steel, CL - corrosion layer, CP - corrosion-filled paste, P - unaltered paste, A - air voids), (Wong et al., 2010).

2.5.4 Nano-indentation

Zhu, Sonebi and Bartos (2004a) reports the significance of SCC on bond strength and ITZ properties of SCI. Depth-sensing nano-indentation techniques were utilized to measure micro-strength of ITZ and elasticity modulus of SCI. The bond and interfacial properties of SCI in different SCC mixes and conventional vibrated concrete mixes were examined considering same strength grades (35 MPa and 60 MPa). It was reported that reinforcement bar diameter had major influence on the bond strength of RC. When reinforcement bar diameter increased from 12 to 20 mm, the maximum bond strength seems to decrease. It was reported that bond strength of SCC mixes was 10 – 40% higher than the conventional vibrated concrete mixes for both the reinforcement bar diameters (12 and 20 mm). The nano-indentation study on SCI conformed that bottom side of horizontal bars had lesser elastic modulus values and also the micro-strength of ITZ were considerably poor than on the top side.

Wang *et al.* (2009) studied the ITZ in steel fiber reinforced mortar using nano-indentation testing. The steel fiber-matrix and fiber-matrix-aggregate interfaces were investigated. Two w/c ratios were considered (0.3 and 0.5), as well as the concrete mix was incorporated with 10% silica fume. The elastic modulus and hardness of ITZ between steel fibers and mortar was analyzed by nano-indentation techniques. It was reported that w/c ratio had an influence on the hardness values of ITZ between steel fibers and mortar. The hardness value of transition zone in sample with w/c ratio 0.3 was more than that of the samples with 0.5 w/c ratio. The authors reported that addition of silica fume had influenced the elastic modulus and nano-indentation hardness of the ITZ between steel fibers and mortar. It was reported that hardness profile was increased for the sample with 0.3 w/c ratio and 10% silica fume, indicating good interfacial bonding across the transition zones. It was also reported that the samples without silica fume had shown comparatively low hardness profile and voids were observed in the vicinity of steel fiber matrix. SEM image in BSE mode showing indentation area is shown in Figure 2.24.
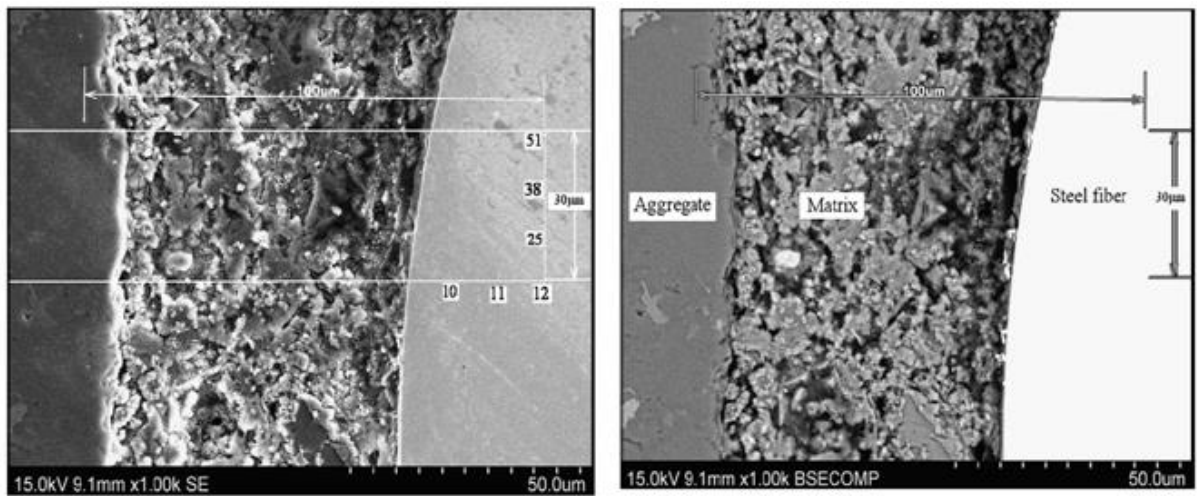
Figure 2.24: Images of the steel fiber-matrix-aggregate interfacial zone in sample 0.5 water/binder ratio, SE image (Left), BSE image, where the dimension of the indented area is 100 μm × 30 μm (Right) (Wang *et al.*, 2009).

Allison *et al.* (2012) investigated the effect of a new kind of coating on the ITZ properties between reinforcing steel and concrete. The authors created a glass-ceramic coating by combining C_3S and C_2S to the exterior surface of glass-enameled steel which was efficiently employed to enhance the bond between concrete and steel bars, which also provided corrosion protection to the steel. The ITZ of uncoated samples had relatively higher porosity and also weak phases at SCI. Also, the values of elastic modulus were dropped significantly at SCI. However, the change in elastic modulus values were steadier in coated samples, with little variation from the steel to 1st ground-coat enamel, then to 2nd cement/enamel coat, and lastly to the paste (Refer Figure 2.26). Spikes which were observed in Figure 2.25 were unusual (e.g., the 100 GPa spike at 140 µm depth, 150 GPa spike at 130 µm depth and etc.) and the reason for their presence was attributed to the anhydrous cement particles present in the paste. SEM micrographs of ITZ of coated and uncoated steels are presented in Figure 2.26. It was reported that the gradual change in elastic modulus values at SCI had positive impact on the bond properties between steel and concrete. The coating on the steel surface had decreased the debonding problems and eventually improved the bond strength of reinforcing bars.
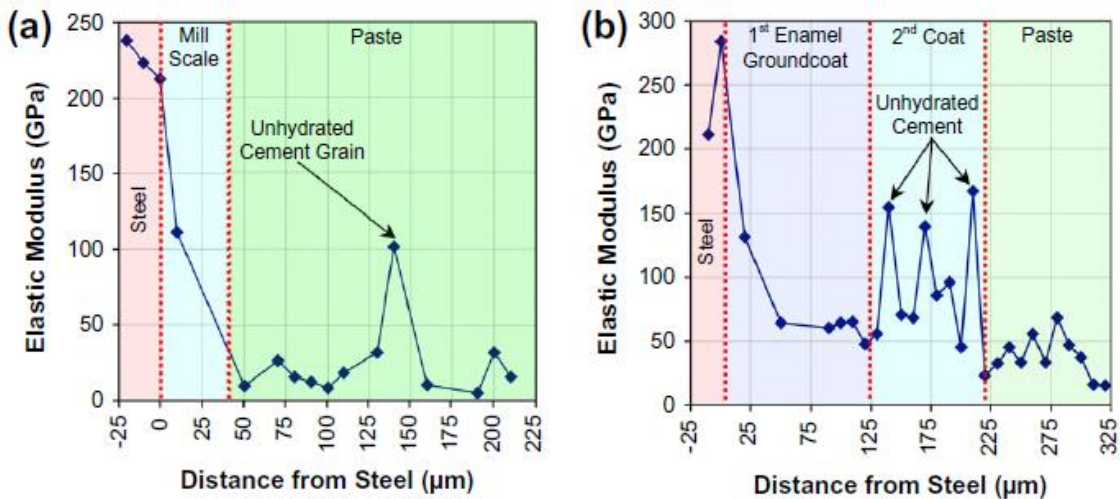
Figure 2.25: Elastic modulus measured across the ITZ of (a) uncoated and (b) coated steels using nano-indentation (Allison *et al.*, 2012)
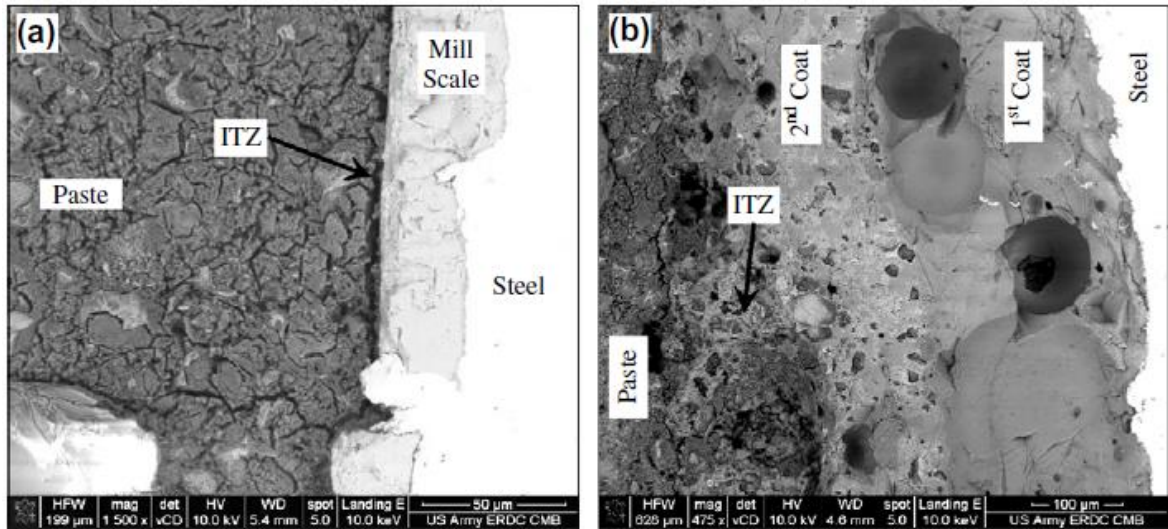
Figure 2.26: (a) SEM micrograph of uncoated steel and ITZ, (b) SEM micrograph of coated steel and ITZ (Allison *et al.*, 2012).

2.6 SUMMARY OF LITERATURE

The steel-concrete bond is considered to be the weak link in the reinforced concrete composite. It is important to analyze the properties at steel-concrete interface as it contributes to durability and long-term serviceability of reinforced concrete structures.

While doing literature survey, it is observed that limited amount of work has been published on characterization of properties at steel-concrete interface. This is due to the difficulty in measuring the microstructure properties at steel-concrete interface non-destructively. However, few researchers used advanced concrete cutting tools, sophisticated grinding and polishing machines which reduced the damages to steel-concrete interface. It was observed that a reliable method of sample preparation technique is yet to be developed where there is minimal damage to steel-concrete interface. The common tool used to characterize the properties of SCI is SEM and EDS. Few researchers also used nano-indentation techniques to characterize steel-concrete interface at nano level. In addition, as a part of indirect measurement, the quality of steel-concrete interface was assessed through bond strength which was measured using pullout test.

It is observed in the literature that steel-concrete interface is characterized by slightly higher w/c ratio, and eventually a higher porosity. The porosity at steel-concrete interface is uneven and differs from point to point along the periphery of steel bar, with several microns to few millimeters in thickness for different kinds of concrete. Because of the higher porosity, the interfacial zone is characterized by existence of larger crystals, predominantly of calcium hydroxide. However, steel with good concrete adhesion can be protected from corrosion by the presence of calcium hydroxide crystals at steel-concrete interface. The porosity or porous zone thickness is sensitive to w/c ratio, supplementary cementitious materials, strength of concrete, amount of compaction and type of cement.

The w/c ratio and porosity at steel-concrete interface are directly proportional, as w/c ratio increases, porosity at the interface increases. With limited research findings it is observed that, the addition of supplementary cementitious materials reduces the porosity at steel-concrete interface. Few research articles report that addition of supplementary cementitious material have negligible or no effect on porosity at steel-concrete interface. A detailed investigation is essential to understand the effect of supplementary cementitious materials on the properties of steel-concrete interface.

Nano level exploration of steel-concrete interface has provided much better understanding about expansive pressure developed due to corrosion process. At some point in corrosion process, it was noticed that corrosion products occupy porous space at steel-concrete interface and push the cement paste near the interface. Once the corrosion products reach solid concrete surface, the expansive pressure will be developed. Nano-indentation techniques are even useful in measuring the advanced mechanical properties such as hardness properties and elastic modulus of rust layer around steel-concrete interface. The hardness and elastic modulus properties of cement paste or hydration products at steel-concrete interface was not explored systematically by the researchers.

Some of the researchers interpreted the quality of steel-concrete interface by bond strength of reinforced concrete using pullout test. The porosity at steel-concrete interface has direct effect on the bond strength of reinforced concrete. Researchers reported that as

porosity around steel-concrete interface increased, the bond strength reduced significantly. Compressive strength of concrete has positive impact on bond strength, as compressive strength increases, bond strength increase significantly and the increase in bond strength was more apparent in the small diameter reinforcement bars. The bond strength and corrosion of reinforcing steel has peculiar relation. Some of the authors reported that corrosion of a limited degree (0.5 – 3%) increased the bond strength of reinforced concrete. However, it was also reported that bond strength significantly reduced as the corrosion level increased from certain level (more than 3%).

Many researchers tried and achieved some level of success in increasing the bond strength and corrosion resistance of reinforced concrete by incorporating mineral admixtures in to the concrete mix. Researchers reported that pH of the pore solution significantly decreased when mineral admixtures were added to the concrete mix. However, the reduced value of pH in pore solution is still higher than the value of the pH which required for inducing corrosion.

2.7 GAPS IDENTIFIED IN THE LITERATURE

- The porous zone thickness around steel-concrete interface is an important parameter in assessing the service life of structures through service life prediction models. Many researchers are assuming a constant value of porous zone thickness around steel-concrete interface without any experimental verification.

- Researchers have already explored the significance of mineral admixtures or mineral admixed cements on enhancing the mechanical properties of concrete. However, the influence of mineral admixtures or mineral admixed cements on the microstructure properties of steel-concrete interface in reinforced concrete is still not very well defined. Also, the effect of mineral admixtures or mineral admixed cements on the porous zone thickness around the steel-concrete interface is so far not investigated systematically.

- The positive effect of mineral admixtures on bond strength of reinforced concrete has been reported by many researchers by making use pullout test. But the effect towards the improvement in microstructure properties of steel-concrete interface has not been addressed in a systematic manner.

- A limited amount of literature is available on the variation of porous zone thickness of steel-concrete interface after marine environment exposure of reinforced concrete structures. A detailed and systematic analysis of porous zone thickness variation from corrosion initiation to till corrosion cracking is essential in service life prediction of reinforced concrete structures exposed to marine environment.

In the present investigation the above mentioned gaps in the literature are being properly addressed. Objectives of the present study will fill the literature gaps and provide better understanding about the engineering properties of steel-concrete interface.

2.8 OBJECTIVES OF THE PRESENT INVESTIGATION

- To investigate the significance of types of cements (OPC, PPC and PSC) on the engineering properties of steel-concrete interface by employing advanced characterizing techniques such as Scanning Electron Microscopy (SEM), Energy Dispersive X-ray Spectroscopy (EDS) and Nano-Indentation.
- To determine the effect of curing duration on compressive strength, ultimate bond strength and microstructure properties of steel-concrete interface produced with OPC, PPC and PSC concrete.

- To investigate the effect of marine environment on porous zone thickness of steel-concrete interface and ultimate bond strength of reinforced concrete.

CHAPTER - 3

EXPERIMENTAL METHODOLOGY

This chapter provides detailed information about the properties of materials used for the experimental work, mix design, different tests conducted on fresh and harden properties of concrete. The methodology of sample preparation for scanning electron microscopic study, measurement of PZT around SCI, energy dispersive spectroscopy analysis and nano-indentation study are described.

3.1 RAW MATERIALS AND THEIR PROPERTIES

The materials required for the study are collected and tests were carried out to determine their physical, chemical and mineralogical properties. The properties of these materials were determined in the laboratory as per standard specifications.

3.1.1 Types of cements used

Three kinds of commercially available cements, ordinary Portland cement (OPC), Portland pozzolana cement (PPC) and Portland slag cement (PSC) were used in the present study. The chemical and physical properties of OPC, PPC, and PSC are tabulated in Table 1. The grading curves of OPC, PPC and PSC is presented in Figure 3.1.

3.1.2 Coarse aggregate

Locally available crushed stone coarse aggregate of maximum size of 20 mm was used in this study. The aggregates were composed of a mixture of rounded and angular aggregates. The various properties of aggregates are determined as per IS 2386 (Part III, IV):1963 and the specifications are checked as per IS 383:2016 requirements. The physical properties of coarse aggregates are presented in Table 3.2. The grading curve of coarse aggregates is presented in Figure 3.1.

Table 3.1: Physical and chemical properties of OPC, PPC, PSC

Compound	OPC (%)	PPC (%)	PSC (%)
SiO_2	20.5	29.2	27.5
Al_2O_3	5.3	9.6	10.5
Fe_2O_3	4.6	4.0	3.2
CaO	62.2	43.5	45.6
MgO	0.8	1.2	3.5
SO_3	2.3	2.6	2.0
Loss on ignition	2.3	2.6	2.0
Specific gravity	3.15	2.94	3.03
Blaine Fineness (m^2/kg)	300	343	360

Table 3.2: Physical properties of coarse aggregates

Sl. No	Property		Value
1	Specific gravity		2.72
2	Bulk density	Loose	1333 kg/m^3
		Compacted	1567 kg/m^3
3	% of voids		47.1 %
4	Moisture content		Nil
5	Water absorption		0.5%
6	Flakiness		12%
7	Elongation		7%

3.1.3 Fine aggregate

Locally available river sand conforming to zone-II according to IS 383: 2016, passing through 4.75 mm sieve was used. The properties of sand such as fineness modulus and specific gravity were determined as per IS 2386-1963 (Part I). The properties of fine

aggregate are shown in Table 3.3. The grading curve of fine aggregates is plotted and the same is presented in Figure 3.1.

Table 3.3: Physical properties of fine aggregate

Sl. No	Property		Value
1	Specific gravity		2.56
2	Bulk density	Loose	1436 kg/m^3
		Compacted	1700 kg/m^3
3	% of voids		38.2 %
4	Moisture content		Nil
5	Water absorption		1%
6	Fineness modulus		3.14
7	Silt content		1.1%

3.1.4 Superplasticizer

The super plasticizer, Master Glenium 51 of chemical manufacturer company BASF was used in the present investigation, which was a high-performance super plasticizer based on PCE (poly carboxylic ether). The properties of Master Glenium 51 are given in Table 3.4.

Table 3.4: Properties of superplasticizer

Aspect	Light brown liquid
Relative density	1.08 ± 0.01 at 25ºC
pH	≥6

3.1.5 Water

The tap water was used for concrete mixing. The suitability of tap water was confirmed by the chemical analysis and the same is presented in Table 3.5. The tap water used was of drinking standards and the same was confirmed by chemical analysis according to IS 10500 – 2012 specifications.
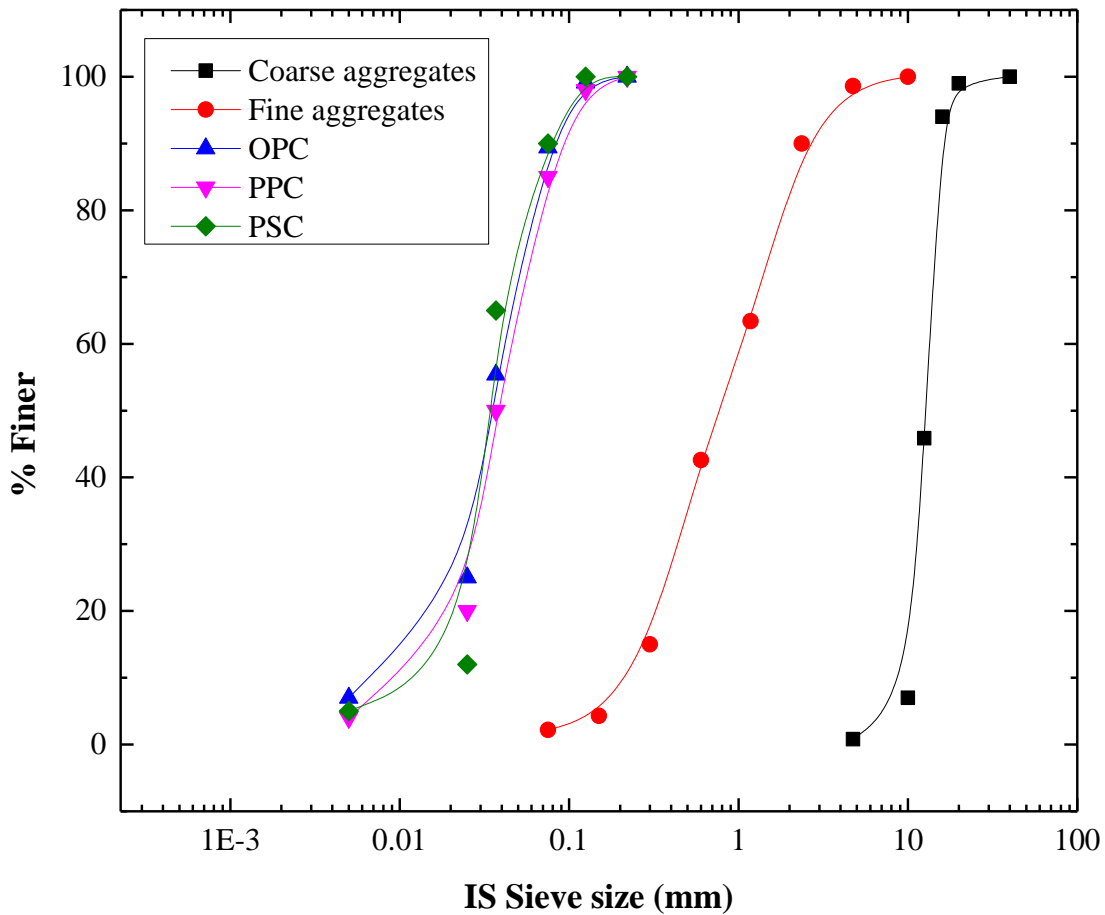
Figure 3.1 Grading curve of coarse aggregates, fine aggregates, OPC, PPC and PSC

Table 3.5: Chemical analysis of tap water

Sl. No.	Parameters	Values	Limit specified in IS 10500 - 2012
1	pH	7.2	6.5-8.5
2	Sulphates	12.5 mg/l	<250 mg/l
3	Iron	0.13 mg/l	<0.30 mg/l
4	Alkalinity	95 mg/l of $CaCO_3$	<200 mg/l of $CaCO_3$
5	Chlorides	7.43 mg/l	<250 mg/l
6	Dissolved oxygen	6 mg/l	4-14 mg/l
7	Solids	42 mg/l	<500 mg/l
8	Total hardness	41 mg/l	<200 mg/l

3.1.6 Reinforcement bars

In the present investigation 10 mm deformed steel bars (Fe 500) were used as reinforcement bars. The ribs of the reinforcement bars were helical is nature and same kind of ribbed bars were used for all the tests in the present study. Freshly procured steel bars according to the required sizes are used in producing RC without any prier treatment to the steel bars (as received condition).

3.2 MIX PROPORTION AND TEST METHODS

The concrete mix was designed according to IS 10262-2009 specifications to have desired compressive strength of M40 grade with w/c ratio of 0.4. The details of concrete mix proportions are given in Table 3.6. The same mix proportion was followed for the production of OPC, PPC, and PSC concrete.

Table 3.6: Mix proportion of concrete

Mixture proportions for M40 grade concrete					
Water (kg/m^3)	Cement (kg/m^3)	Fine aggregate (kg/m^3)	Coarse aggregate (kg/m^3)	SP	w/c
152	380	816.64	1104.77	0.5%	0.40

w/c – water cement ratio, SP – superplasticizer (0.5% of cement content)

3.2.1 Production of concrete

In the present investigation it was aimed to produce good workable concrete with slump of 75-85 mm. In order to achieve desired slump, PCE based superplasticizer Master Glenium 51 was used. The optimum content of superplasticizer was determined by trial methods. The superplasticizer dosage of 1% of cement content was used as the initial trial dosage. The resultant mix had bleeding and setting problems. Hence, the dosage was reduced to 0.5% of cement content, which yielded good workable concrete with required slump.

The production of good workable and quality concrete depends on the mixing time as well as method of mixing sequence. In order to determine optimum time and mixing sequence, different trial mixes were tried.

Trial mix 1

Sequence 1: Initially, sand and fine aggregates were poured into the concrete mixer of capacity 120 kg and thoroughly mixed for two minutes.

Sequence 2: Course aggregates were added to the mixer and mixed for one more minute.

Sequence 3: Then, superplasticizer was mixed with entire quantity of water and added to the concrete mixer and mixed for next five minutes before testing the fresh properties of concrete. The total mixing time was eight minutes for trial mix 1.

Trial mix 1, yielded a good workable mix with slump of 60 mm without bleeding or segregation. However, the slump value has fallen short than the required one. This made to try for an alternative mixing sequence.

Trial mix 2

Sequence 1: First sequence is identical to trial mix 1, sand and fine aggregates were poured into the concrete mixer and thoroughly mixed for two minutes.

Sequence 2: The coarse aggregates were then added to the concrete mixer and mixed for one more minute.

Sequence 3: About 50 to 60% of the water was first added to the mix and mixed for three minutes.

Sequence 4: Then, the remaining water was mixed with superplasticizer and added to the concrete mixer and mixed for next four minutes. The total mixing time was ten minutes for trial mix 2.

The resulting mix was an excellent workable mix with a slump of 80 mm. The increased mixing time and timely addition of superplasticizer resulted in increased slump value compared to trial mix 1.

The ingredients of concrete were mixed as mentioned in trial mix 2 in order to produce a good workable and quality concrete, and the sequence of mixing was followed every time for concrete production.

3.2.2 Measurement of compressive strength

Cubical specimens of size $100 \times 100 \times 100$ mm were prepared and were tested for compressive strength measurement at 7, 14, 28, 56 and 90 days of curing periods. The

compressive strength test was carried out according to the specification given in IS 516, 1959.

3.3.3 Measurement of ultimate bond strength

To assess the ultimate bond strength, cubical specimens of size $100 \times 100 \times 100$ mm were prepared and provision was made to place a single reinforcement bar (Fe 500) at the center of the cubical specimen as presented in Figure 3.2. The ultimate bond strength was measured by pullout test according to the specifications detailed in IS 2770 - 1967 (Part-I) and reaffirmed in 2007.
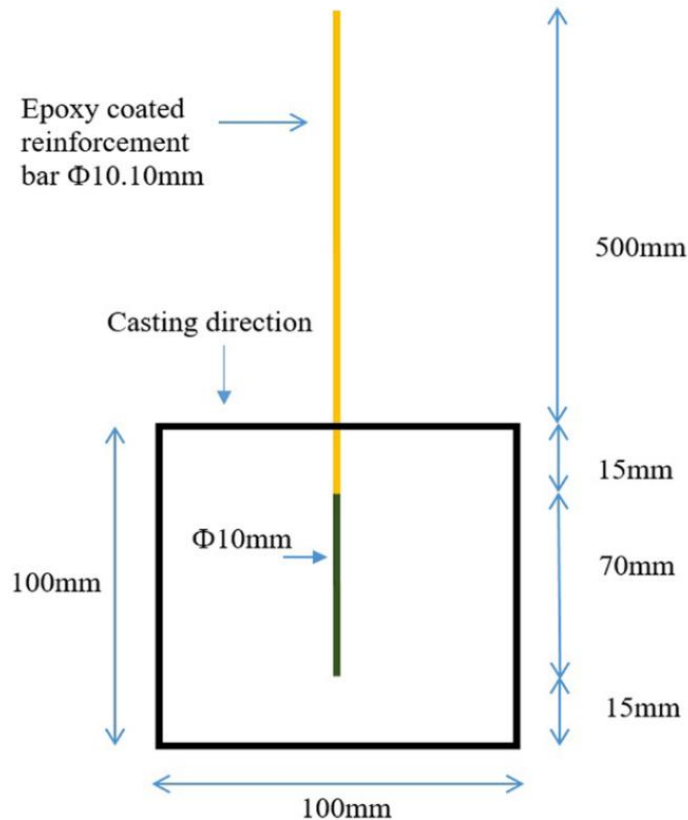
Figure 3.2: Schematic representation of sample used for bond strength measurement

3.3 SAMPLE PREPARATION FOR SCANNING ELECTRON MICROSCOPIC STUDY

3.3.1 Preparation of RC samples for SEM study

The sample preparation of RC samples for SEM analysis is a challenging process. It is a science and art to produce a flat polished surface with minimal damages to SCI. There are two main stages involved in sample preparation for SEM analysis. The first stage is cutting of RC samples into suitable size and the second is grinding and polishing.

3.3.1.1 Cutting of RC samples into suitable size

For laboratory studies, researchers used different sizes of RC samples. For example, Chen *et al.*, (2018) used prism samples of size $150 \times 150 \times 300$ mm, Kenny and Katz (2015) used prism samples of size $150 \times 150 \times 270$ mm, Tayfun A Soylev and François (2003) used prism samples of size $150 \times 150 \times 200$ mm, Zhao *et al.*, (2011) used $150 \times 150 \times 300$ mm size prism samples. Horne, Richardson and Brydson (2007) and Glass *et al.*, (2001) not mentioned the sample sizes. In order to cut and obtain relatively small RC sample for SEM analysis, researchers used diamond saw cutters (Glass *et al.*, 2001b; Kenny and Katz, 2015; Chen *et al.*, 2018). However, speed of diamond saw cutters was not mentioned by any of the researchers. It is a common and easy practice to cut large sections with high-speed diamond saw cutters of speed 2000 – 3500 rpm. The measurement of PZT at SCI may be compromised due to the use of high-speed diamond saw cutters for cutting RC samples. If RC sample size is larger, it is proposed to take the desired size of core along with the reinforcement bar. Further, cored samples can be easily cut using slow speed precision diamond saw cutters of cutting speed 30 – 300 rpm. For SCI analysis, the requirement is a few millimeters of properly adhered concrete around the reinforcement bar.

It is also important to select desired size of the core. The core size depends on the SEM's sample holder dimensions and sample holder of low-speed precision diamond saw cutter. In order to maintain a safe working distance in SEM's vacuum chamber, most of the

SEM's restrict the thickness of the specimens. Maximum dimensions of specimens for SEM analysis may be less than 35 mm diameter and 10 mm thick cylindrical specimens and it can be varied depending upon SEM sample holder capability and safe working distance in SEM's vacuum chamber.

In the present study core of 32 mm was selected. The cube size of $100 \times 100 \times 100$ mm were cast with a single reinforcement bar of 10 mm diameter at center as shown in Figure 3.2. A core section of 32 mm diameter along with reinforcement bar was obtained as shown in Figure 3.3 (b). For the firm grip, 'C' clamps were used to clamp the cube which ensures the safe working of core cutter as shown in Figure 3.3 (a). Once the cores were obtained, the next step was to cut the cores to get flat cross-sections without much damage to SCI. To ensure this, obtained cores along with reinforcement bars were encased within 40 mm Polyvinyl chloride (PVC) pipes. And then 8 mm gap was filled by epoxy resin hardener (Acrylic powder and resin-based hardener) as shown in Figure 3.3 (c). The epoxy resin hardener ensures firm grip while cutting the cores for getting the required thickness.

(a)   (b)   (c)
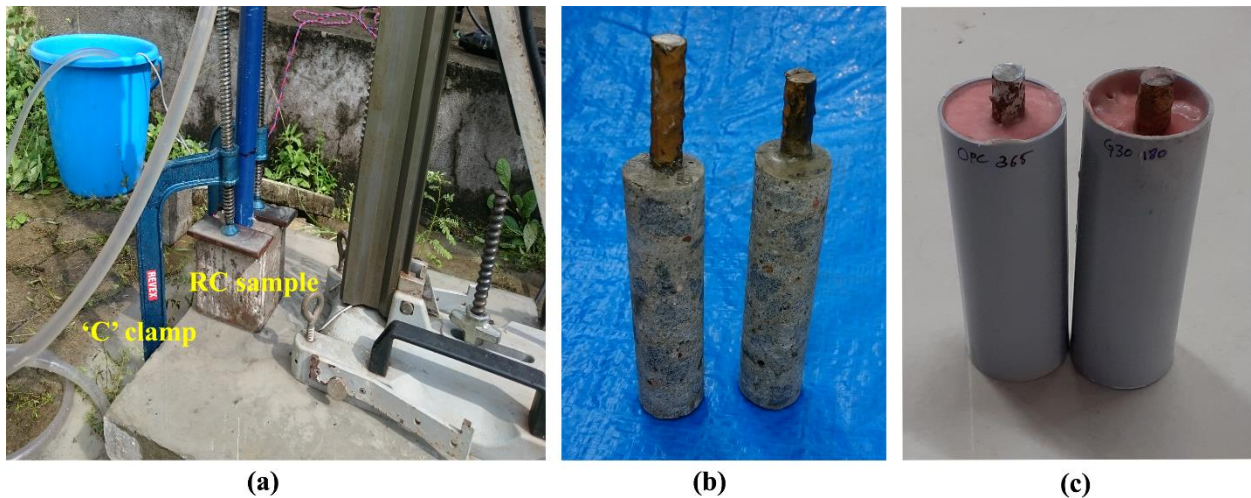
Figure 3.3: Core cutting of reinforced concrete sample, (a) 'C' clamps for safe working of core cutter, (b) 32 mm diameter cored reinforced concrete (RC) sample and (c) 32 mm cores encased within PVC pipe along with epoxy resin hardener

The step of cutting the cores for cross-section analysis is of prime importance. Two ways of cutting methods were illustrated in the present study. The first one is high-speed diamond saw cutter, with a speed of 3200 rpm. The second was a low-speed precision diamond saw cutter with speed of 100 rpm. Types of cutters used for cutting the cored reinforced concrete samples are shown in Figure 3.4. For high-speed diamond saw cutter, water was used as a lubricant, which also controls the heat generated during cutting. High-speed diamond saw cutter was having a blade thickness of 3 mm and the time required to cut the reinforced concrete cores was about 10 seconds. However, for low-speed precision diamond saw cutter, oil was used as a lubricant, the blade thickness was 0.4 mm and the time required to cut the reinforced concrete cores was about 5 hours. The significance of speed of cutting tool and thickness of specimen obtained from RC sample on the properties of SCI are studied and the same is discussed in chapter 4.

(a)   (b)

Figure 3.4: Two types of cutters used for cutting the cored reinforced concrete samples, (a) high speed diamond saw cutter and (b) low-speed precision diamond saw cutter

3.3.1.2 Grinding and polishing

Once RC specimens were cut to the desired size, next process is grinding and polishing to obtain a flat polished surface. Before starting the grinding process, specimens were moulded with ultralow viscosity epoxy. Further, the epoxy was dried at three different temperatures (90°C, 80°C and 60°C) to study the drying shrinkage cracks. For grinding the specimens, silicon carbide papers of grades P320, P600, and P1000 were used. For polishing the specimens, a diamond paste of particle size 0.25 μm and 0.15 μm were used (non-aqueous solution type). The grinding duration, polishing duration and pressing force were studied and the same is discussed in chapter 4.

3.3.2 Vibration analysis during cutting of RC samples

From the literature, it was understood that major damage to SCI occurred during the cutting process of RC samples to obtain a relatively small specimen for SEM analysis (Glass *et al.*, 2001a; Horne, Richardson and Brydson, 2007; Angst *et al.*, 2017). In order to understand the vibrations generated during the cutting process, vibration sensors interfaced with Arduino board were fixed to the sample. Arduino board is an open-source electronics platform based on easy-to-use hardware and software which senses the inputs from many sensors.

Vibration sensors interfaced with Arduino board are basically used for vibration analysis. The vibration sensor used in the study is presented in Figure 3.5 (a). The schematic circuit diagram of the vibration sensor is presented in Figure 3.5 (b). Vibration sensor has two blocks, SW420 vibration module followed by a comparator (LM393). Through potentiometer, the sensitivity threshold can be adjusted. For adjusting the sensitivity and measurement of vibrations during the cutting process, a program was written and the same was executed with the help of Arduino-Beta software (version 1.9.0 – beta).

A line diagram of vibration analysis during sample cutting is presented in Figure 3.6. Figure 3.7 shows vibration sensor (SW420) attached to the sample and connected to the Arduino board (before cutting the sample). Figure 3.8 shows the sample while cutting

and vibration sensor (SW 420) attached to the specimen for the measurement of vibrations during the cutting process.

The sensor works in the following way. When the sensor or module is stable, the circuit gets turned on and the output will be high (no vibrations). When the movement or vibration occurs, circuit gets briefly disconnected and the output will be low. During vibration, the comparator response changes from 0V to 5V (volts) and vice versa. Duration taken by the comparator to vary from 0 to 5 volts or vise-versa will be recorded as strength of vibration. Longer the vibrations, longer will be the disconnectedness and higher will be the strength of vibration. Strength of vibration is a relative measurement of duration of disconnectedness because of vibrations during the cutting process. The extent of vibrations during the high-speed diamond saw cutting and low-speed precision diamond saw cutting process and its influence on engineering properties of SCI are discussed in chapter 4.
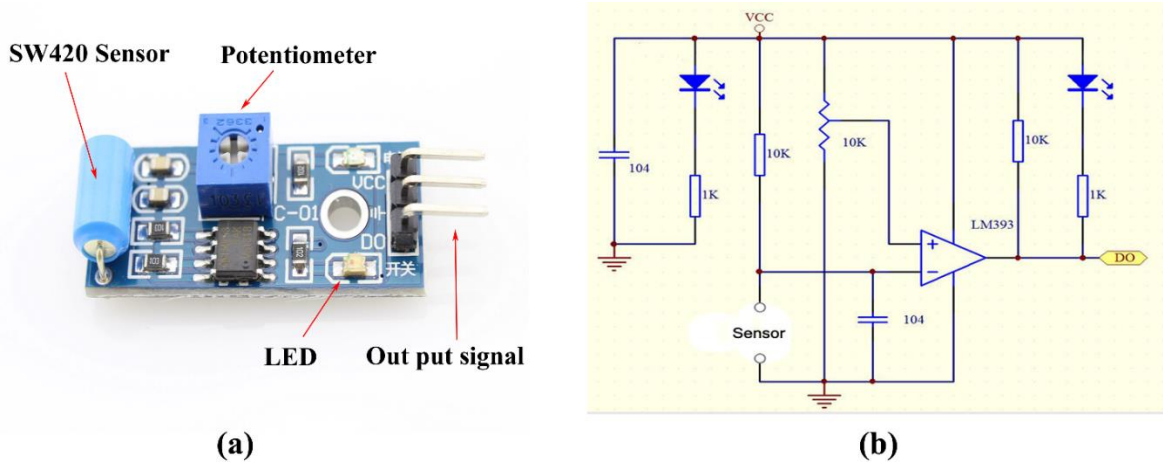
Figure 3.5: (a) Vibration sensor (SW420) and (b) schematic circuit diagram of vibration sensor (SW420)
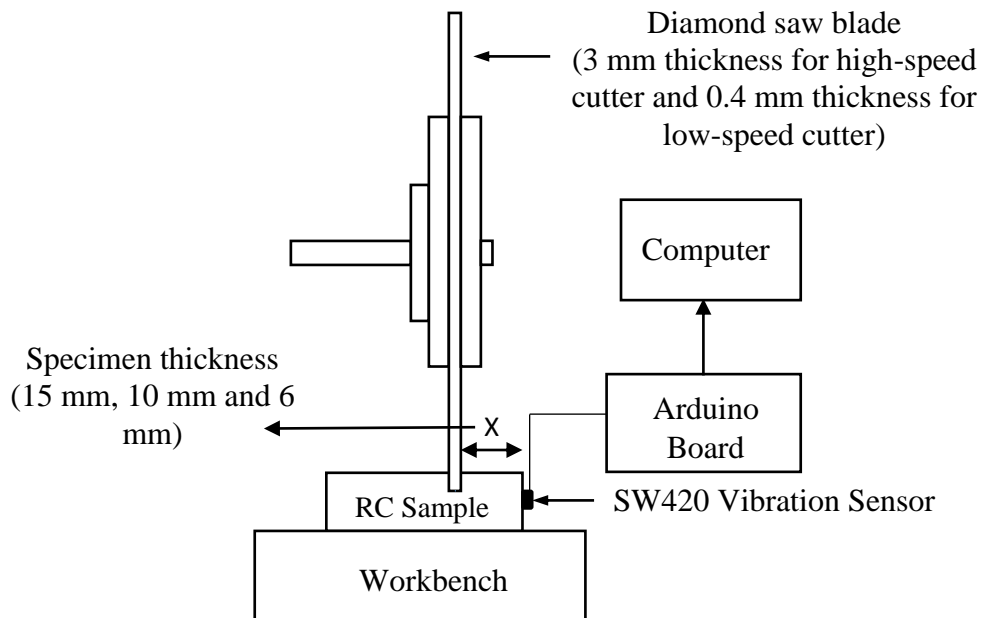
Figure 3.6: Line diagram of cutting the sample and vibration analysis
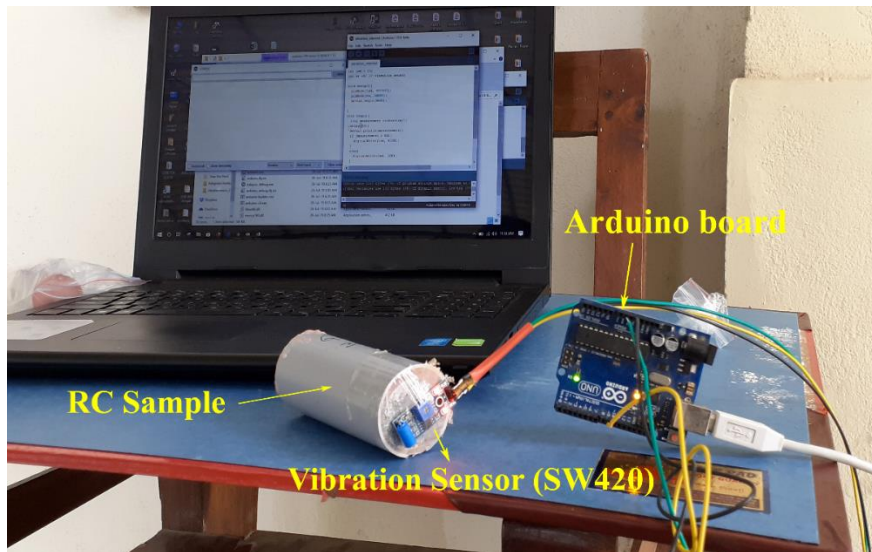
Figure 3.7: SW420 Vibration Sensor attached to the sample and connected to the Arduino board

Figure 3.8: Sample cutting while vibration sensor (SW 420) attached to the RC sample

3.4 LOCATION OF BSE IMAGES AROUND STEEL-CONCRETE INTERFACE

Before taking the SEM images, the samples were gold sputtered in a vacuum container. The BSE images were taken at 12 spots around SCI in the clockwise direction, and the same is illustrated in Figure 3.9. A fixed magnification of ×500 was kept constant for all BSE images for consistent measurements in image analysis. The pixel size of the SEM images was 1,024 (width) by 768 (height) pixels, the working distance was 6.9 mm, and the excitation energy was 15 kV.
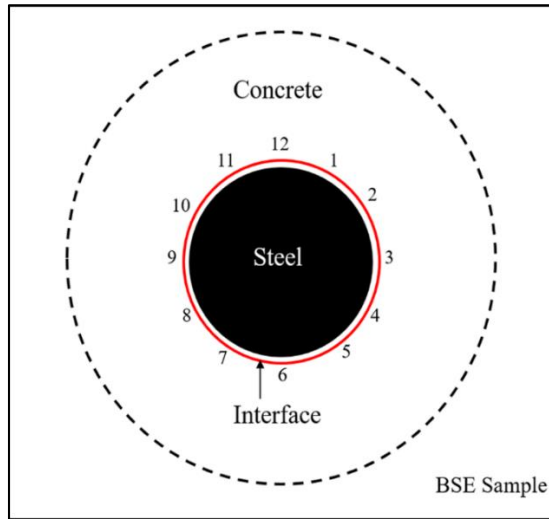
Figure 3.9: Location of BSE images acquired around SCI (each number represents one spot)

3.5 MEASUREMENT OF POROUS ZONE THICKNESS AROUND STEEL-CONCRETE INTERFACE

Figure 3.10 (a) shows a representative BSE image of OPC concrete at 28-day of water curing. Figures 3.11 (a) and Figures 3.12 (a) show the BSE images of PPC and PSC concrete, respectively, at 28 days of water curing. The different elements of RC, such as steel, aggregates, hydrates, and pores or voids can be identified with respect to contrast difference in BSE images (Scrivener *et al.*, 1986; Wong, Head and Buenfeld, 2006; Chen *et al.*, 2019). The contrast variation in BSE images is a function of mean atomic numbers of individual elements, such as steel, hydration products, aggregates, and pores in RC. To begin with, the individual elements of RC in Figure 3.10 (a) were manually selected and the grayscale histograms of individual elements were extracted, which is presented in Figure 3.10 (b). Figure 3.11 (b) and Figure 3.11 (b) show the grayscale histograms of individual elements of PPC and PSC concrete, respectively.

The bright part in Figure 3.10 (a) represents steel because of its high atomic number. Pores or voids appear dark in the BSE images because electrons get trapped in the voids and less reflection is received. The contrasts of hydration products and aggregates are

72

between these two extreme phases. The histograms in Figure 3.10 (b) show the grayscale range of individual phase, and the x-axis represents the color scale ranging from 0 to 255 (no unit). It can be observed that grayscale ranges of steel and pores do not overlap, which makes it easy to differentiate the borderline between steel and pores. However, it is challenging to differentiate the borderline between hydrates in the cement paste and pores because of the overlaps of grayscale ranges. It is necessary to adopt a consistent and dependable method to differentiate the borderline among the cement paste and pores with an appropriate grayscale threshold value.
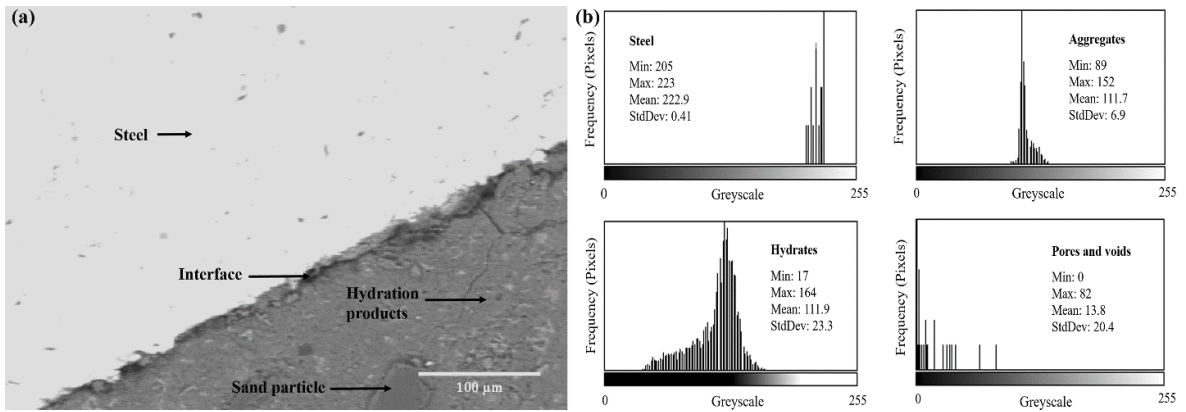
Figure 3.10: (a) BSE image showing a typical SCI of 28-day cured OPC concrete and (b) histogram of each phase showing grayscale range from 0–255
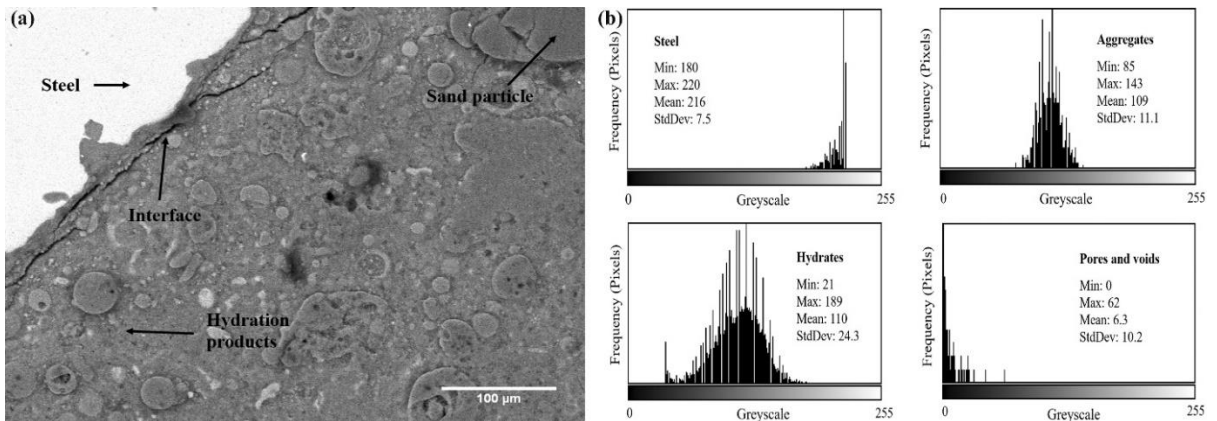
Figure 3.11: (a) BSE image showing a typical SCI of 28-day cured PPC concrete and (b) histogram of each phase showing grayscale range from 0–255
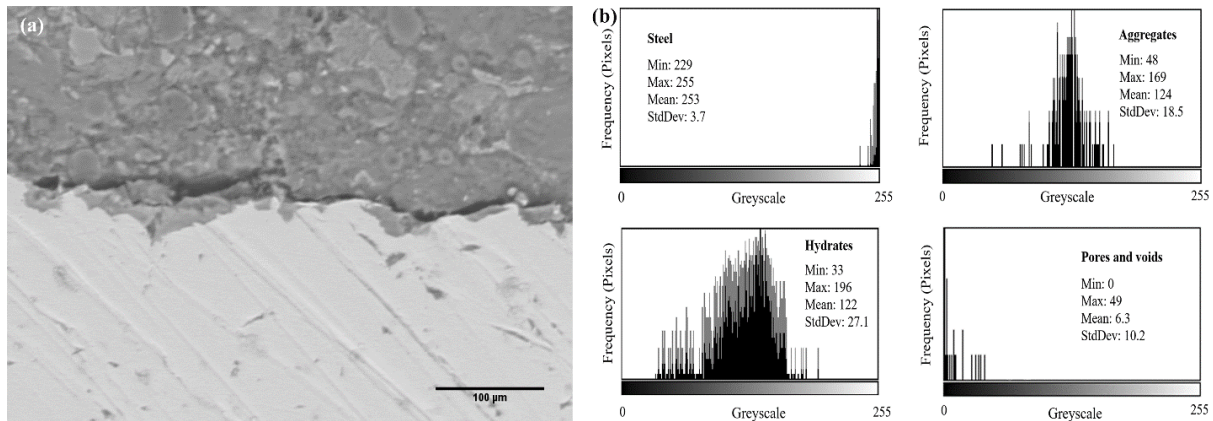
Figure 3.12: (a) BSE image showing a typical SCI of 28-day cured PSC concrete and (b) histogram of each phase showing grayscale range from 0–255

One of the common methods used was manual thresholding, because of which the features of important regions can be shown. Few researchers suggested different techniques to differentiate the borderline between the cement paste and pores in BSE images (Scrivener *et al.*, 1986; Wong, Head and Buenfeld, 2006; Yang, 2006). Scrivener *et al.* (1986) proposed a tangent slope thresholding method to identify the borderline between pores and cement paste. Wong, Head and Buenfeld (2006) also proposed an effective method to characterize the borderline between pores and cement paste in BSE images. However, in RC, SCI boundary needs to be distinguished from steel as well as cement paste. Only a few researchers proposed a technique to distinguish the porous zone from steel and cement paste at SCI (Kenny and Katz, 2012; Chen *et al.*, 2018). An effective and reliable method was proposed by Chen *et al.* (2018) in which the pixels with a gray value of 42 or below were considered pores or voids. After thresholding the BSE images with a grayscale value of 42, the porous zone was identified, and then the thickness of porous zone was measured.

Similarly, in the present study, the pixels with a grayscale value below 42 were also considered as pores with respect to the gray value of 42, and thresholding was performed in ImageJ software. The BSE image in Figure 3.10 (a) was selected for thresholding with a grayscale value of 42, and Figure 3.13 (a) shows the post-thresholding BSE image.

Now, the clear image showing the porous zone between steel and concrete can be seen along with small pores. Once the thresholding was performed, the BSE image was adjusted upright for PZT measurement. The rotation and PZT measurements are shown in Figure 3.13 (b).

A total of 30 measurements were considered, and the mean value was considered as PZT. The minimum value and maximum values are the lowest and highest PZT measurements of three samples at Spot 1. The mean value is the average of 90 measurements (30 measurements for each sample) for a particular grade of concrete. Spots 1–12 for each sample were assigned clockwise with an angle difference of 30°, the spot marking started immediately after the sample preparation was over. The measured mean value 10.56 μm can be considered as the representative PZT for the BSE image shown in Figure 3.10 (a). The same technique of thresholding and PZT measurements was followed for all the BSE images. For example, for OPC at 28 days of curing, a total of 36 images (3 specimens × 12 spots) were considered for image analysis. Furthermore, the average of three values at each spot was reported as the mean PZT at all 12 spots.

The PZT for OPC, PPC, and PSC concrete were measured around SCI at 12 spots for 28-day and 90-day curing. Figure 3.14 shows the four representative BSE images of OPC concrete at 28-day curing at Spots 3, 6, 9, and 12. Figure 3.15 shows the post-thresholding BSE images at Spots 3, 6, 9, and 12. After thresholding, the PZT in BSE images were adjusted upright and arranged parallel for convenience in comparison of results. It can be seen that PZT is not uniform around the steel bar. In Figure 3.15, the mean PZT is 8.16 μm at Spot 12, 10.59 μm at Spot 3, 18.66 μm at Spot 6, and 4.52 μm at Spot 9.

The measurements shown in figure (b) from top to bottom are:

12.01 μm
8.61 μm
5.20 μm
15.81 μm
14.41 μm
19.81 μm
10.41 μm
5.80 μm
16.61 μm
12.01 μm
21.01 μm
26.92 μm
3.00 μm
11.71 μm
11.71 μm
14.11 μm
3.60 μm
4.80 μm
7.51 μm
10.21 μm
9.01 μm
7.51 μm
6.60 μm
6.00 μm
8.71 μm
12.61 μm
9.91 μm
11.41 μm
8.11 μm
3.75 μm
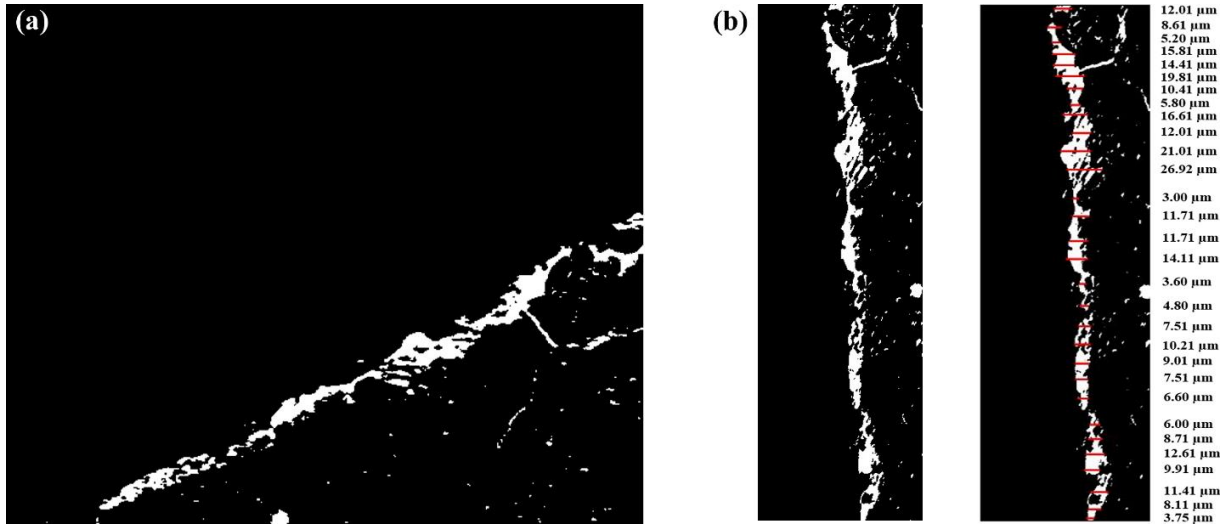
Figure 3.13: (a) BSE image after thresholding with gray value of 42 and (b) upright rotation and porous zone thickness measurements

Steel

Steel
Interface
Concrete
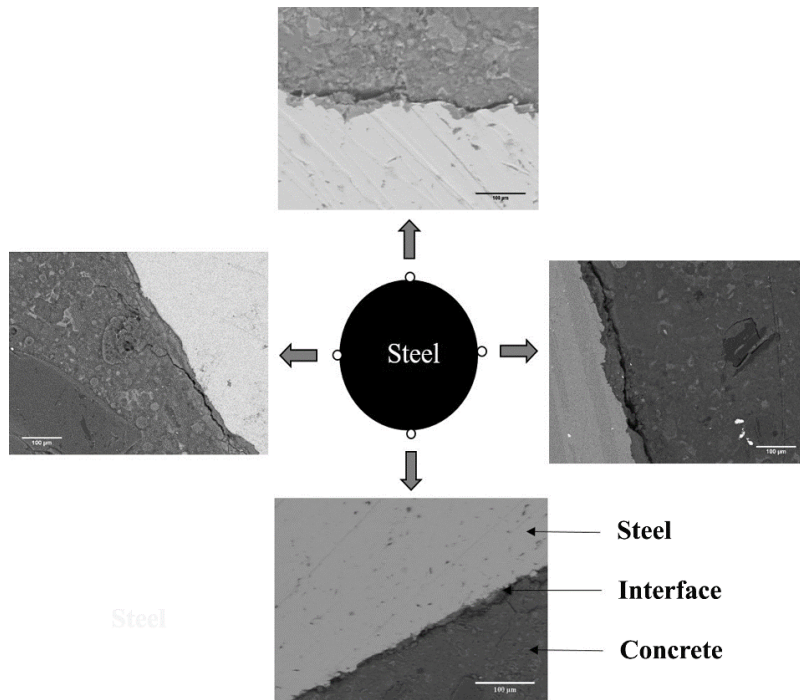
Figure 3.14: BSE images around SCI for OPC sample at 28 days of curing
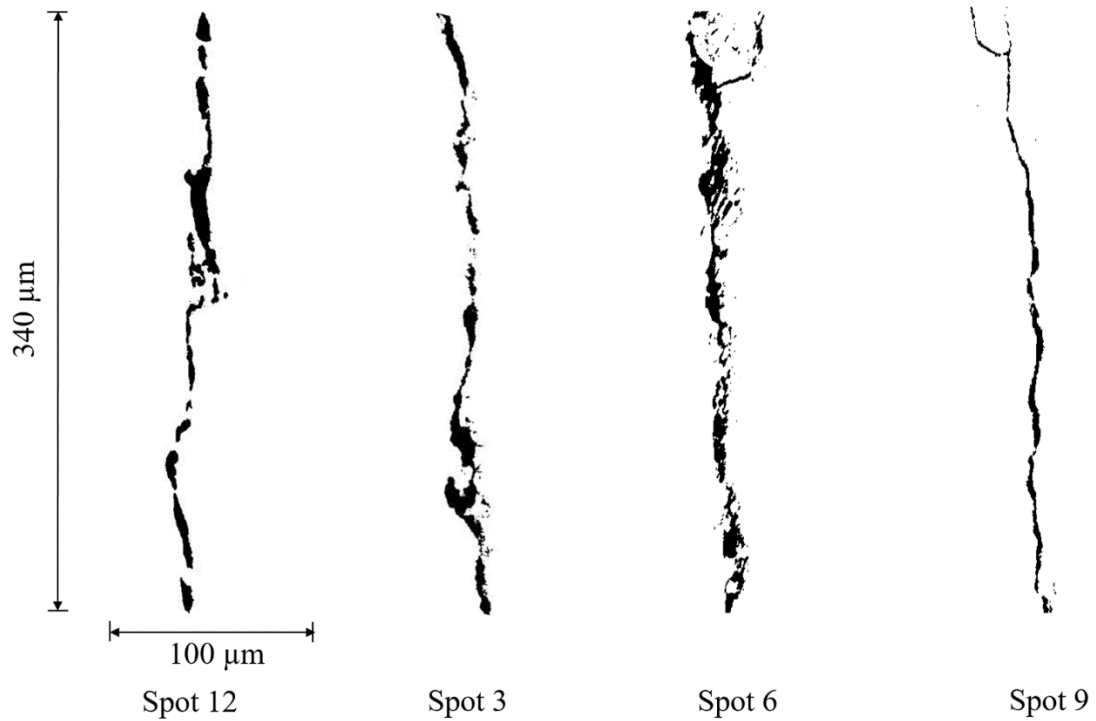
Figure 3.15: Post-thresholding BSE images at Spots 3, 6, 9 and 12 for OPC sample at 28 days of curing

3.6 EDS MEASUREMENT AROUND STEEL-CONCRETE INTERFACE

The EDS analysis records the atomic weight percentages of all the hydration products. This primarily involves gathering a number of spectra for quantitative analysis. The data from EDS analysis can be presented in the form of atomic ratio plots (Escalante-Garcia, Mendoza and Sharp, 1999; Hiremath and Yaragal, 2017a, 2017b). The atomic ratio plots were presented by taking the mean values of six individual EDS points around SCI for each sample. The locations of representative EDS points around the steel-concrete are graphically shown in Figure 3.16. A total of six locations around SCI were considered. EDS points away from the steel surface with distances of 20, 40, and 60 μm were also measured.
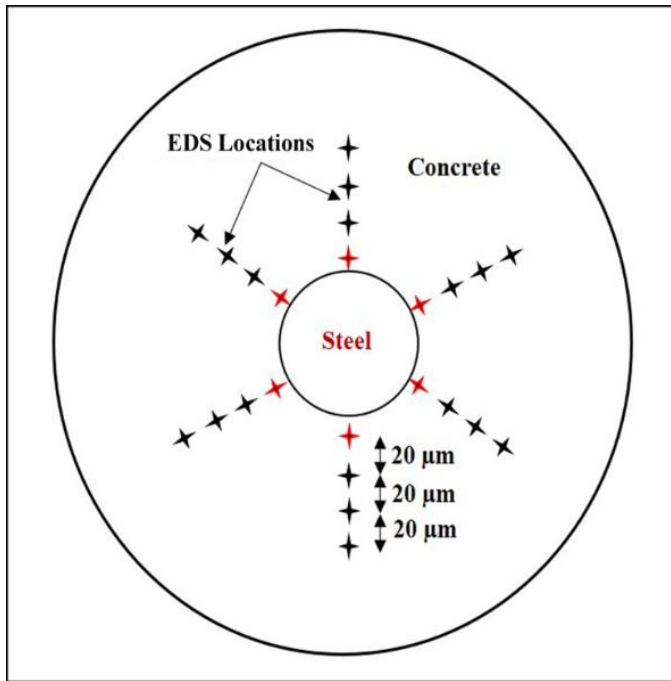
Figure 3.16: Representative locations of EDS points around SCI

Figure 3.17 shows the representative EDS points as spectrum 1 and 2, which are 0 and 20 µm away from the steel surface, respectively. The calcium/silicon (Ca/Si) ratios from EDS points were calculated to plot the atomic ratio plots. The mean value of six locations was considered, and the same is presented as one value of the Ca/Si ratio in atomic ratio plots. For example, at SCI (approximately at 0 µm), six points were measured and are shown as red in colour (Figure 3.16). From EDS measurements, the corresponding values of Ca/Si ratios were calculated for six locations, and the mean value was presented as Ca/Si ratio in atomic ratio plots at 0 µm from SCI. The same method of presenting the mean value of Ca/Si ratio was followed for 20, 40, and 60 µm distance from SCI.
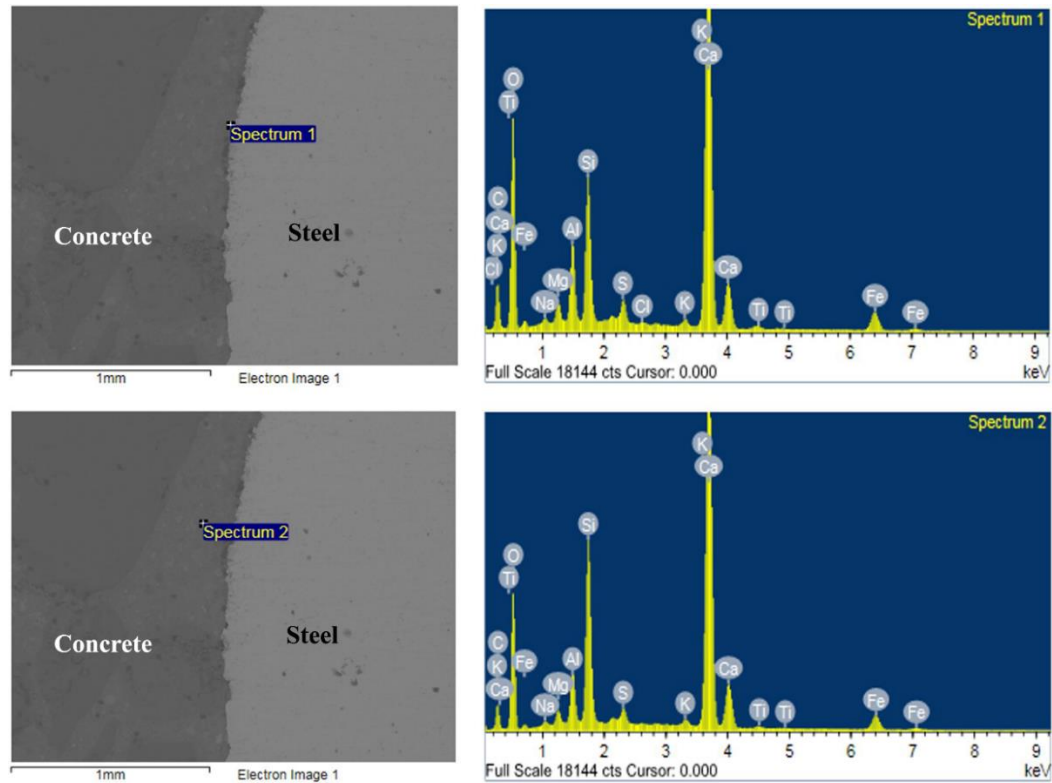
Figure 3.17: EDS points at SCI (Spectrum 1 is at 0 μm and Spectrum 2 is at 20 μm away from the steel surface) of OPC 28-day water-cured sample

3.7 NANO-INDENTATION MEASUREMENT AROUND STEEL-CONCRETE INTERFACE

Nano-indentation is an advanced technique used to measure the nanomechanical properties at the level of nanoscale. This is an effective and dominant tool to discover the materials microstructural and nano-structural elastic properties, hardness and creep properties. To improve the macro mechanical properties of concrete, it is important to study the mechanical properties at the micro and nanostructure level. This technique works on a basic theme that a very tip indenter with known properties and geometry is allowed to indent on the face material and examining the mechanical performance of the material from the reaction of the tip (Davydov, Jirásek and Kopecký, 2011; Hu and Li, 2015). The indenter used should be much rigid than the testing specimen. For the cement-based materials, Berkovich tip was used which has a three-sided pyramid that seems

much trouble-free to grind. After the indenter comes in contact with the specimen surface, the rate of loading was kept constant with 2 mN/s until the load reached the maximum load of 50 mN (Wang, Wang and Liu, 2004). Then the load was held at its maximum for 5 seconds before unloading at the same constant rate. In order to avoid the influence of adjacent indents on the measured values, a distance of 10 μm in parallel direction was programmed.

To characterize SCI, a series of indents were made in the interface region between steel and concrete to measure its mechanical properties at the nano level. The modulus of elasticity and hardness properties around SCI were studied as a function of distance from the steel surface towards bulk denser concrete. The representative indentation points around SCI (at six locations) are presented in Figure 3.18. The red marked points (Figure 3.18) represent '0 μm' (approximately) on SCI and the next set of points were 20 μm, 40 μm and 60 μm away from the steel surface. A total of 24 points were selected around SCI and at each point, 5 number of indentations were obtained for better accuracy. Overall, 120 indentations were obtained for each specimen to analyze the modulus of elasticity and hardness properties around SCI.
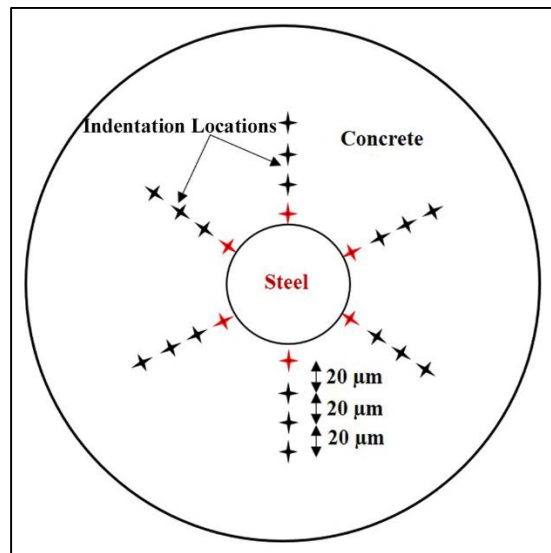
Figure 3.18: Schematic representation of indentation points around SCI

3.8 EXPOSURE OF REINFORCED CONCRETE SAMPLES TO MARINE ENVIRONMENT

The marine environment was fashioned by adding 3.5% NaCl to tap water. The RC samples after 90 days of water curing were exposed to simulated marine environment for a period of 90, 180, 360 and 720 days. Once the desired duration of exposure was finished, the samples were taken out of aggressive media and kept for surface drying for four hours before testing. The corrosion analysis of OPC, PPC and PSC concrete were assessed through linear polarization resistance technique. The effect of marine environment exposure on corrosion resistance and ultimate bond strength between steel and concrete was measured after each exposure period. After exposing the RC samples to marine environment, changes in microstructure properties at SCI, especially the PZT was analyzed for OPC, PPC and PSC concrete.

3.9 SERVICE LIFE PREDICTION THROUGH MEASURED VALUES OF POROUS ZONE THICKNESS

The service life of RC samples exposed to marine environment was predicted using mathematical model proposed by El Maaddawy and Soudki (2007). The model considers the PZT as one of the important parameters while predicting the time from corrosion initiation to corrosion cracking. The input parameters for the mathematical models are diameter of the steel reinforcing bar (10 mm), PZT (μm), poisson's ratio of concrete (0.15), corrosion current density (μA/cm^2), characteristic compressive strength of concrete (f_{ck} = 40 MPa), concrete creep coefficient (1.6) and clear cover of the specimen (15 mm). By considering the above input parameters, the time from corrosion initiation to corrosion cracking was calculated.

CHAPTER – 4

FACTORS OF SAMPLE PREPARATION TECHNIQUES ON THE ENGINEERING PROPERTIES OF STEEL-CONCRETE INTERFACE

The method of RC sample preparation for SEM analysis may damage the properties of SCI, especially the PZT. The main influencing factors which can damage the properties of SCI are tool used for cutting RC samples and the process of grinding and polishing. In the present study, the effect of speed of cutting tool used to cut the RC samples and its influence on the properties of SCI are discussed. The high-speed diamond saw cutter used had a speed of 3200 rpm and low-speed precision diamond saw cutter had a speed of 100 rpm. In order to assess the damage to SCI due to speed of cutting tool, vibrations analysis was performed using vibration sensor interfaced with Arduino.

4.1 EFFECT OF SPEED OF CUTTING TOOL, GRINDING AND POLISHING OF RC SAMPLE ON THE PROPERTIES OF STEEL-CONCRETE INTERFACE

4.1.1 Speed of cutting tool

After the cores along with reinforcing steel is obtained (as shown in Figure 3.3), the cored samples were slice cut using high-speed diamond saw cutter (3200 rpm) and low-speed precision diamond saw cutter (100 rpm).

Figure 4.1 shows the samples cut with a high-speed diamond saw cutter. It can be observed that the high-speed diamond saw cutter can easily disturb the interfacial properties. Apart from the speed of cutter, thickness of specimen obtained from the cored sample also influences the damage incurred to SCI. It was observed that as thickness of the specimen reduces, there found be significant damage to SCI. In Figure 4.1 (c), specimen thickness was 6 mm and damage in terms of cracks around SCI were

significant. Comparatively, 15 mm and 10 mm thick specimens had less damage to SCI. Such kinds of cracks at SCI can be seen in some of the research articles in the literature (Monteiro, Gjorv and Mehta, 1985; Zayed, 1991; Wong *et al.*, 2010).

(a)   (b)   (c)
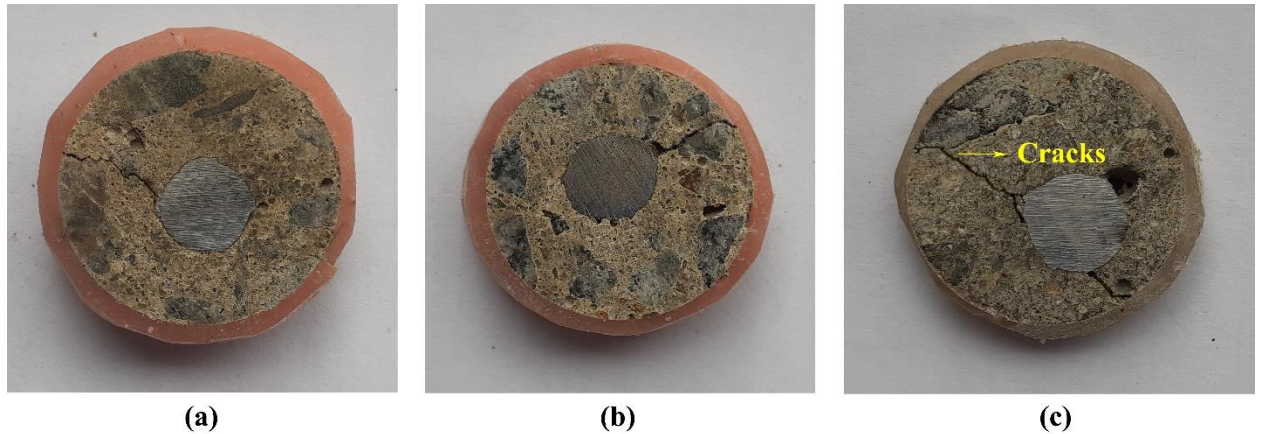
Figure 4.1: Samples cut with high-speed diamond saw cutter, (a) 15 mm thick, (b) 10 mm thick and (c) 6 mm thick

Figure 4.2 shows RC samples cut with a low-speed precision diamond saw cutter. It can be observed that damage to SCI was negligible when compared to high-speed diamond saw cutter. As the cutter speed was only 100 rpm, vibrations during cutting were very less when compared to high-speed diamond saw cutter. Figure 4.2 (a), (b) and (c) shows the specimens of thickness 15 mm, 10 mm and 6 mm, respectively. As the thickness of specimen reduces, small cracks were generated around SCI. Because of the reduced specimen thickness, the concrete thickness surrounding the steel reduces which will affect the bond between concrete and steel.
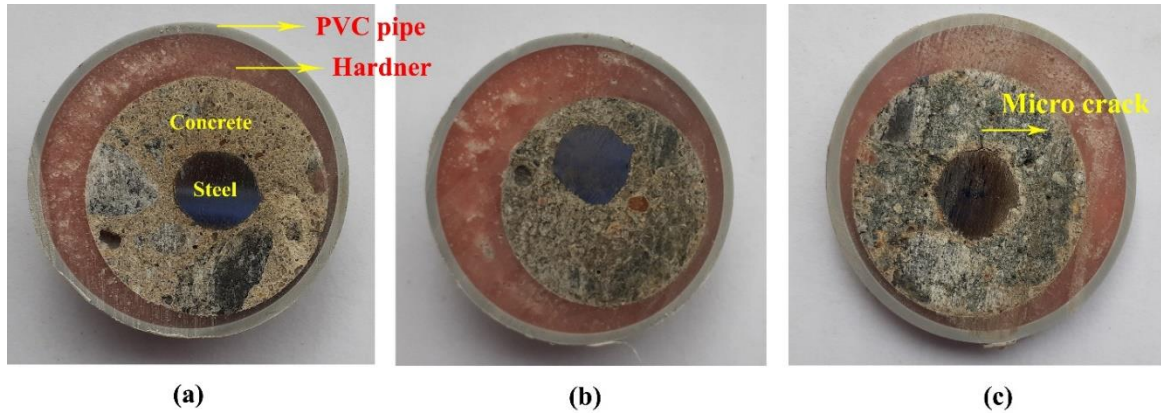
Figure 4.2: Samples cut with low-speed precision diamond saw cutter, (a) 15 mm thick, (b) 10 mm thick and (c) 6 mm thick

4.1.2 Grinding and polishing

Once RC specimens were cut to the desired size, next process is grinding and polishing to obtain a flat polished surface. Before starting the grinding process, specimens were moulded with ultralow viscosity epoxy. A vacuum was applied for a period of two hours in order to force the epoxy to go into the pores. Due to this process, the pores at SCI will appear dark in BSE images and help in image analysis during PZT measurement. Followed by that, specimens were left to harden under room temperature ($27 \pm 2°C$) for 24 hours. The next process was oven drying of epoxy and care needs to be taken as overheating might induce micro-cracks around SCI due to differences in the thermal expansion of concrete constituents and steel (Zayed, 1991; Glass *et al.*, 2001b; Horne, Richardson and Brydson, 2007). In literature, researchers reported a maximum temperature of up to 90°C and a duration of 1 – 2 hours as oven drying temperature after epoxy impregnation (Glass *et al.*, 2001b; Glass and Reddy, 2002; Horne, Richardson and Brydson, 2007). At 90°C, it is observed that there are few drying shrinkage cracks as shown in Figure 4.3 (a) and 4.3 (b), which incurred due to differences in thermal expansion of heterogeneous materials in concrete. In order to avoid development of any drying shrinkage cracks, different drying temperatures such as 80°C and 60°C were tried for a period of 1 hour. As can be seen in Figure 4.3 (c), drying shrinkage cracks can be

84

avoided by oven drying the epoxy impregnated specimens at about 60°C for a period of one hour. Hence, for further studies, epoxy drying temperature of 60°C was considered.

(a)	(b)	(c)
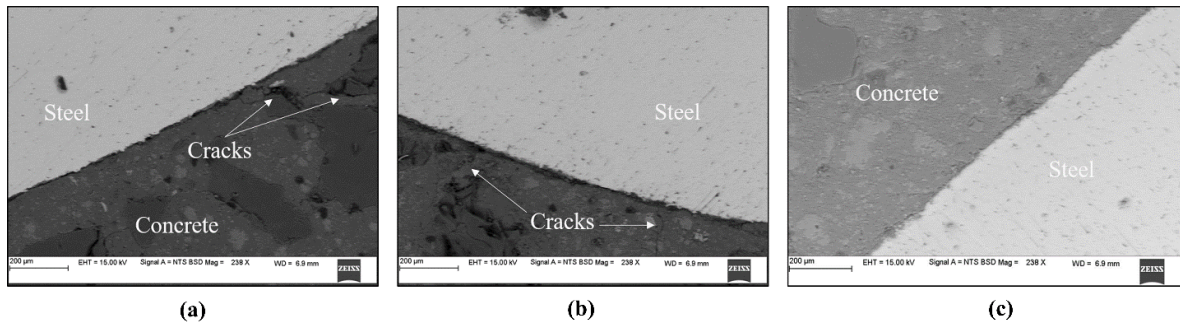
Figure 4.3: SEM images of drying shrinkage cracks observed after oven drying at (a) 90 °C, (b) 80 °C and (c) 60 °C

After oven drying specimens at 60°C, any kind of unevenness on the surface was removed by grinding and polishing process. A polishing machine which controls the speed, time and polishing pressure was used for the process of grinding and polishing. To obtain a flat polished surface, three grinding and two polishing steps were performed. For grinding the specimens, silicon carbide papers of grades P320, P600, and P1000 were used. For polishing the specimens, a diamond paste of particle size 0.25 μm and 0.15 μm were used (non-aqueous solution type).

It is important to take care of deformation incurred to steel bars during grinding and polishing process. To achieve this challenging task, many attempts with different grinding periods and polishing forces were conducted. The first step in the grinding process was found to be particularly important in this investigation as damaged surface is ground off and the newly exposed surface is kept intact. Figure 4.4 (a) and (b) shows two specimens with a grinding duration of 1 minute and 3 minutes, respectively. Both the specimens were ground with P320 silicon carbide grinding paper under a pressing force of 25 kN. Figure 4.4 (b) shows that over-grinding compromise the properties of SCI especially the porous zone thickness. During over grinding, ribs of steel bar deform and

important information get masked. Hence, grinding duration of one minute was considered for each grinding step.

(a)   (b)
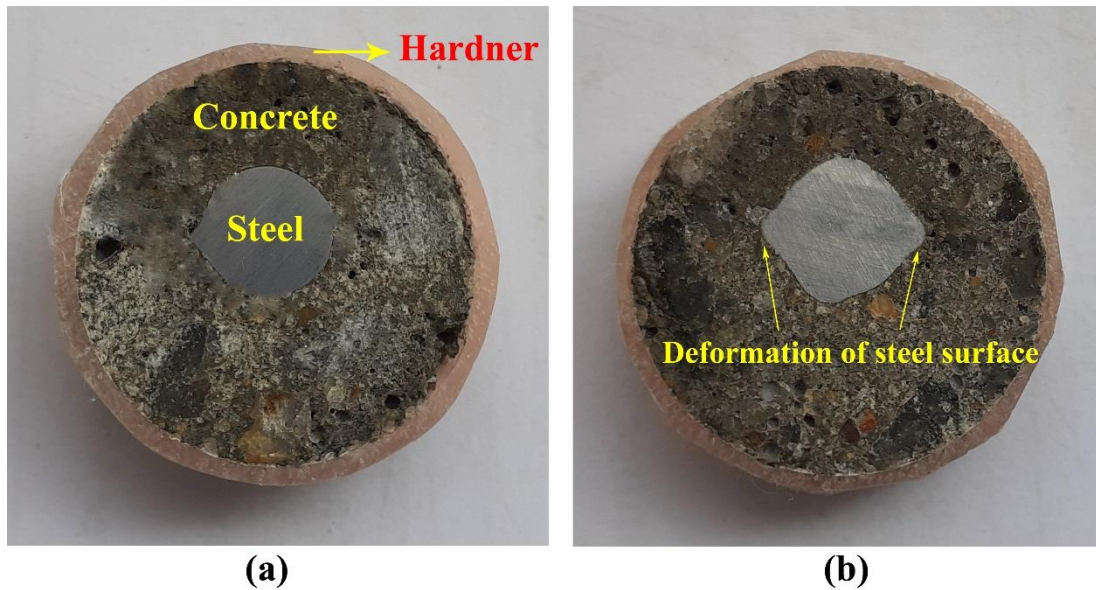
Figure 4.4: Specimens with different initial grinding duration time, (a) 1 minute and (b) 3 minutes

It is to be noted that, apart from grinding duration, the pressing force applied to the specimens during polishing process is also important. It was found after a few trials that pressing force needs to be less than 30 kN (Chen *et al.*, 2019; Goudar, B B Das and Arya, 2019). Figure 4.5 (a) and (b) shows the BSE images of specimens polished under a pressing force of 35 kN and 25kN, respectively. A non-smooth and unclear steel edge can be observed as the polishing force was 35 kN (Figure 4.5 (a)).

The higher polishing force will also lead to spalling of the steel surface and the spalled parts penetrate the epoxy resin filling the voids (Chen *et al.*, 2018). As the polishing force was reduced to 25 kN, the steel edge was found to be smoother with less spalling, that can be observed in Figure 4.5 (b). For further studies, the grinding and polishing pressure was considered as 25kN only.

<div align="center">(a)　　　　　　　　　　　　　　　(b)</div>
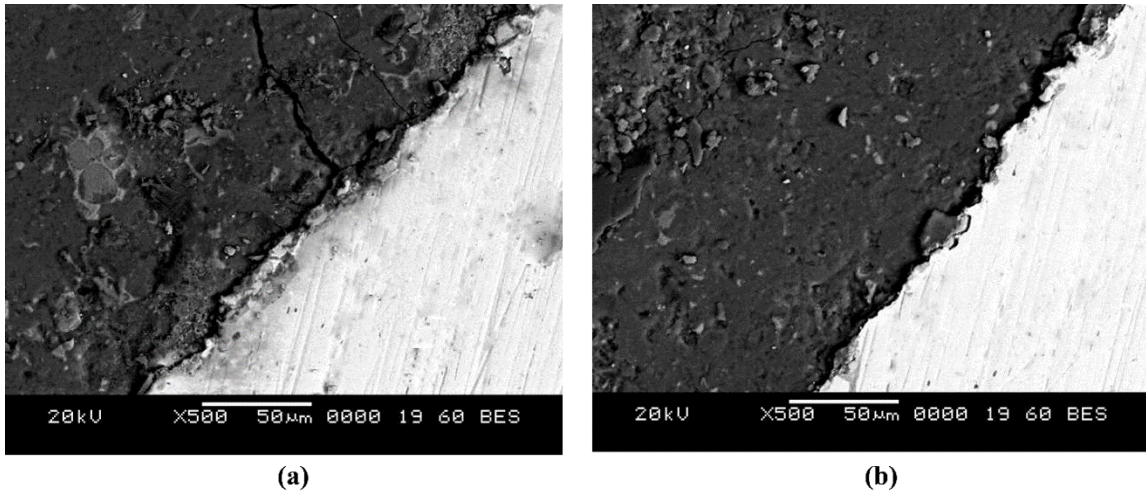
Figure 4.5: BSE images of specimens with different grinding and polishing pressing forces (a) 35 kN and (b) 25 kN

4.2 VIBRATION ANALYSIS DURING THE CUTTING OF RC SAMPLES

It was noticed that during the slice cutting process, vibrations were significantly higher for high-speed diamond saw cutter when compared to low-speed precision diamond saw cutter. To understand the vibrations during RC sample cutting and its effect on the damage to SCI, vibration analysis was carried out using vibration sensors interfaced with Arduino board.

Figure 4.6 and Figure 4.7 show the strength of vibrations recorded with respect to the time taken to cut the RC sample through high-speed diamond saw cutter and low-speed precision diamond saw cutter, respectively. Effect of speed of cutting tool and thickness of specimen obtained from RC sample were analyzed for vibrations generated during cutting. A total of six peaks can be observed in all the graphs. These six peaks represent a particular material or the interfaces between different components of the RC sample. Figure 4.8 shows the cross-section of RC cut specimen where different components and interfaces can be observed. Point 'A' is PVC pipe, point 'B' is the interface between hardener and concrete, point 'C' is the top portion of SCI, point 'D' is the bottom portion

of SCI, point 'E' is the interface between concrete and hardener and point 'E' is PVC pipe.

Once the saw blade starts to cut point 'A' that is PVC pipe, the vibrations started to appear and the same can be observed in Figure 4.8 as peak 'A'. Within no time saw blade cut the hardener-concrete interface and generated the second peak 'B'. As the hardness of concrete and hardener are different, there is variation in the strength of vibrations. When the interface between steel and concrete was encountered the vibrations increased significantly due to the hardness difference that can be seen as peak 'C'. These high vibrations during high-speed cutting damages SCI properties, especially the porous zone thickness (Zayed, 1991; Glass *et al.*, 2001a; Horne, Richardson and Brydson, 2007). Once the upper portion of SCI was cut vibrations become constant because steel is a homogeneous material. As saw blade encounters the bottom portion of SCI, again a strong vibration was recorded that can be seen as peak 'D'. However, strength of vibration for peak 'D' is little smaller as compared to peak 'C'. Steel is a harder material compared to concrete, as the diamond saw blade finishes cutting much harder steel, it then starts to cut the less hard concrete at the bottom portion of SCI, hence the strength of vibration is lesser at peak 'D' compared to peak 'C'. After peak 'D', there are small vibrations till peak 'E', which can be devoted to concrete and hardener interface. The hardener is a less hard material compared to concrete, and hence at the concrete-hardener interface, strength of vibrations is found to be lower. The final peak 'F' is the end of cutting the RC sample.

It can be observed that similar fashioned peaks were recorded for the low-speed precision diamond saw cutter. However, the strength of vibrations was significantly lesser when compared to the high-speed diamond saw cutter. During high-speed diamond saw cutting, as the thickness of the specimen reduces, the strength of vibration at SCI increased drastically which may be the reason for the generation of cracks at the interface (refer Figure 4.1). In the case of low-speed precision diamond saw cutting also the reduction in thickness of specimen increased the vibrations at SCI, but the intensity of vibrations was almost negligible when compared to high-speed cutting. Hence, it can be stated that

damage incurred to SCI is minimal during low-speed precision diamond saw cutting (refer Figure 4.2). Further, it is observed that at 6 mm specimen thickness, few micro-cracks were also noticed even when the sample is cut in a low speed diamond saw cutter. Hence, for further studies, a minimum specimen size of 10 mm was considered.
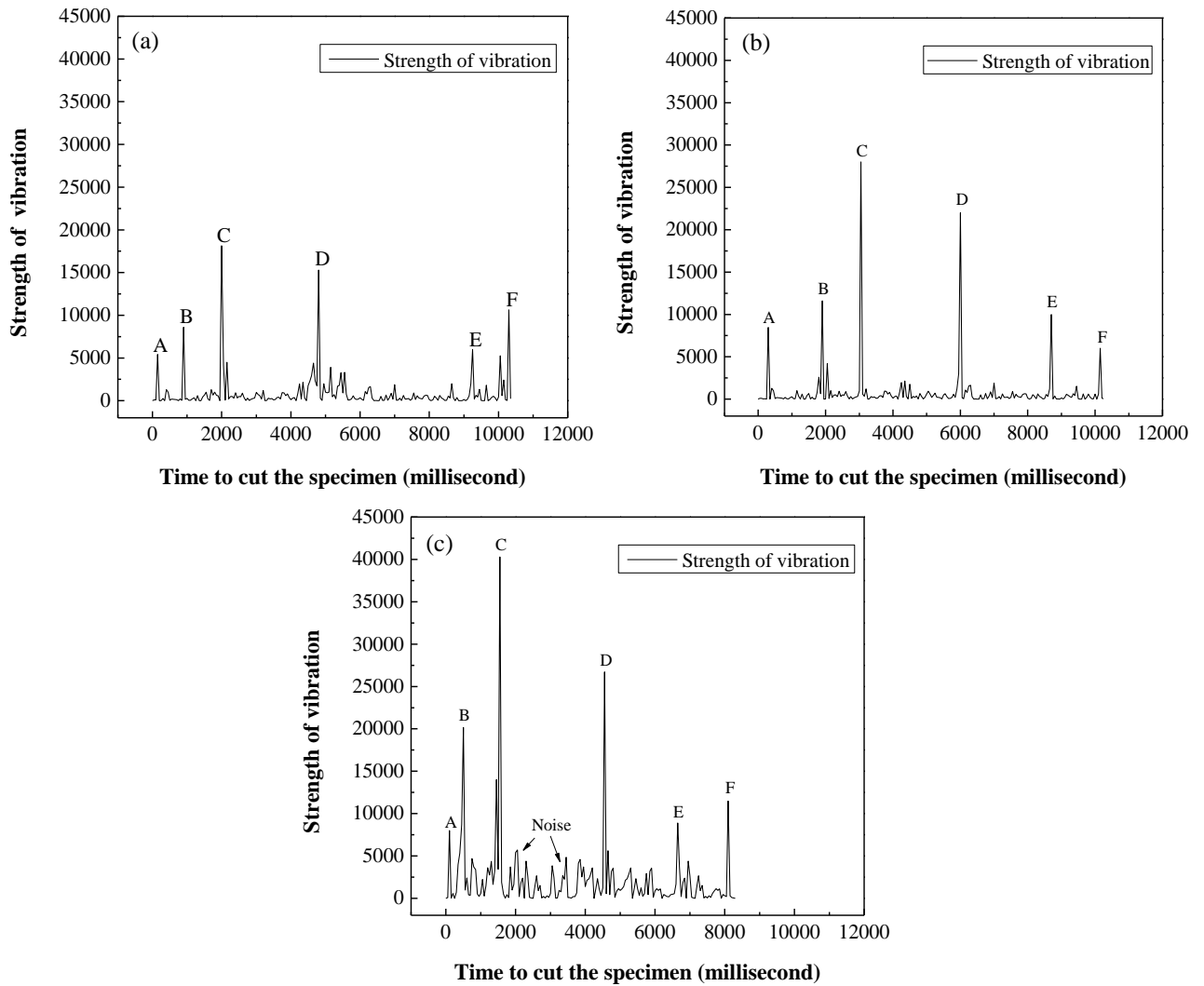
Figure 4.6: Strength of vibration with respect to the time taken to cut the (a) 15 mm thickness, (b) 10 mm thickness and (c) 6 mm thickness samples through high-speed diamond saw cutter
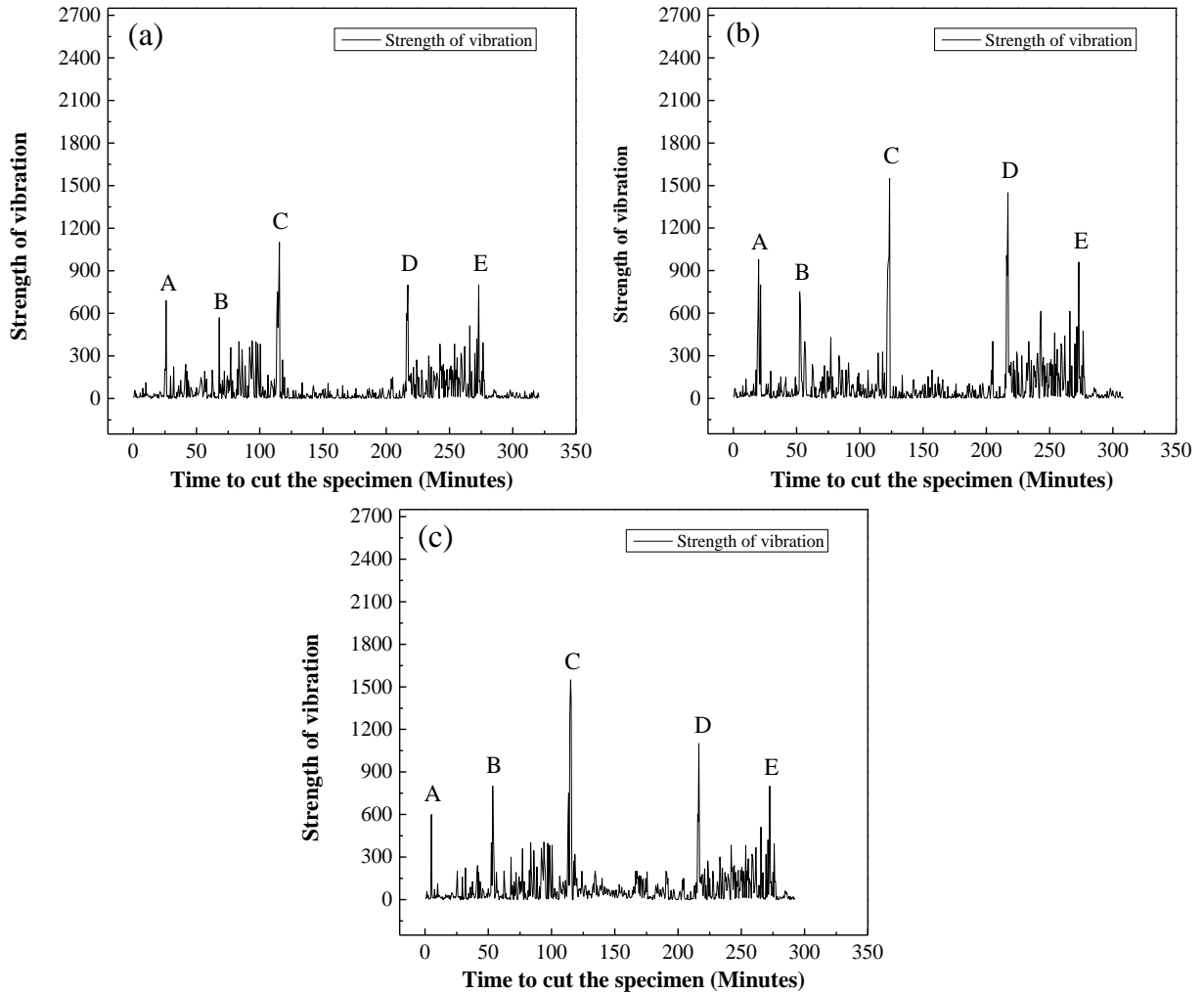
Figure 4.7: Strength of vibration with respect to the time taken to cut the (a) 15 mm thickness, (b) 10 mm thickness and (c) 6 mm thickness samples through low-speed precision diamond saw cutter
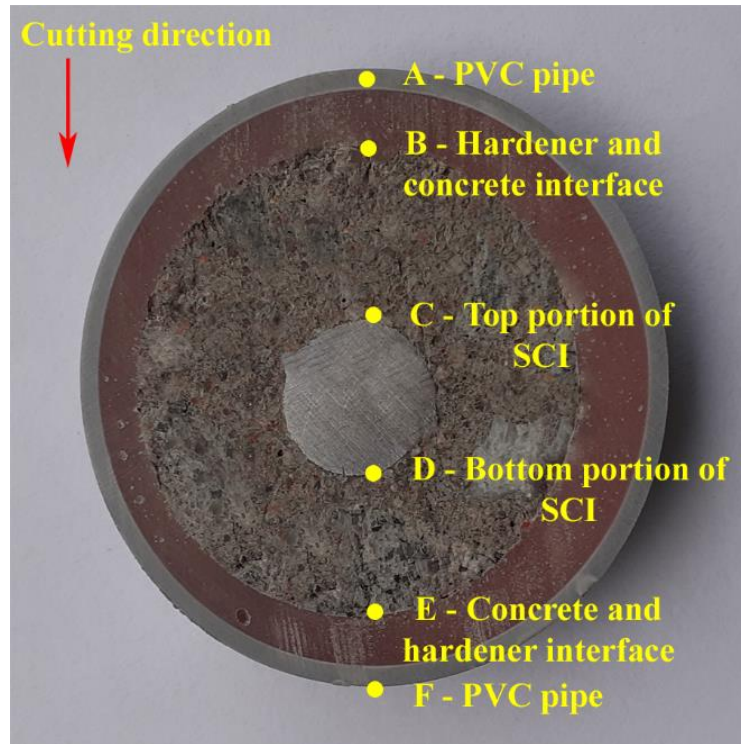
Figure 4.8: Cross-section of an RC cut specimen showing the different components and interfaces

4.3 EFFECT OF SPEED OF CUTTING THE SAMPLE ON THE POROUS ZONE THICKNESS OF STEEL-CONCRETE INTERFACE

The differences in measured PZT around SCI, when cut with a high-speed diamond saw cutter (3200 rpm) and low-speed precision diamond saw cutter (100 rpm) is presented in Table 4.1. An average of 30 measurements were considered to report the mean values of PZT at each spot in Table 4.1. It is to be noted that minimum and maximum values of PZT (in Table 4.1) are the minimum and maximum values within the 30 measurements (refer Figure 3.13b). The effect of two types of cutters (low-speed precision diamond saw cutter and high-speed diamond saw cutter) on the measured value of PZT can be observed in Figure 4.9.

Table 4.1: Porous zone thickness around SCI when RC sample was cut with a high-speed diamond saw cutter and low-speed precision diamond saw cutter

Location	PZT around SCI cut with a low-speed precision diamond saw cutter				PZT around SCI cut with a high-speed diamond saw cutter			
	Mean value (μm)	Standard deviation (μm)	Minimum value (μm)	Maximum value (μm)	Mean value (μm)	Standard deviation (μm)	Minimum value (μm)	Maximum value (μm)
Spot 1	11.22	5.32	4.31	21.66	26.54	5.21	5.89	34.68
Spot 2	08.34	3.44	6.34	18.72	16.25	3.41	8.45	25.33
Spot 3	10.59	4.56	2.79	22.74	21.33	2.14	6.13	30.25
Spot 4	12.61	6.12	4.12	21.86	17.31	5.14	4.12	25.87
Spot 5	15.12	4.33	6.32	28.41	16.32	6.22	10.21	28.20
Spot 6	18.66	5.29	3.02	26.92	28.91	4.37	9.65	42.44
Spot 7	08.32	3.34	6.33	15.62	11.93	2.35	8.34	28.47
Spot 8	16.87	2.61	1.84	20.47	32.24	3.18	13.22	46.78
Spot 9	04.52	1.59	1.28	17.27	14.17	1.17	5.01	20.98
Spot 10	06.82	2.36	3.02	10.66	15.54	2.68	6.74	26.74
Spot 11	07.12	3.33	2.16	11.22	11.26	4.22	5.78	18.88
Spot 12	08.16	4.34	1.69	20.86	18.69	3.16	7.06	29.36
Overall	**Average PZT from 12 spots: 10.69 μm**				**Average PZT from 12 spots: 19.16 μm**			
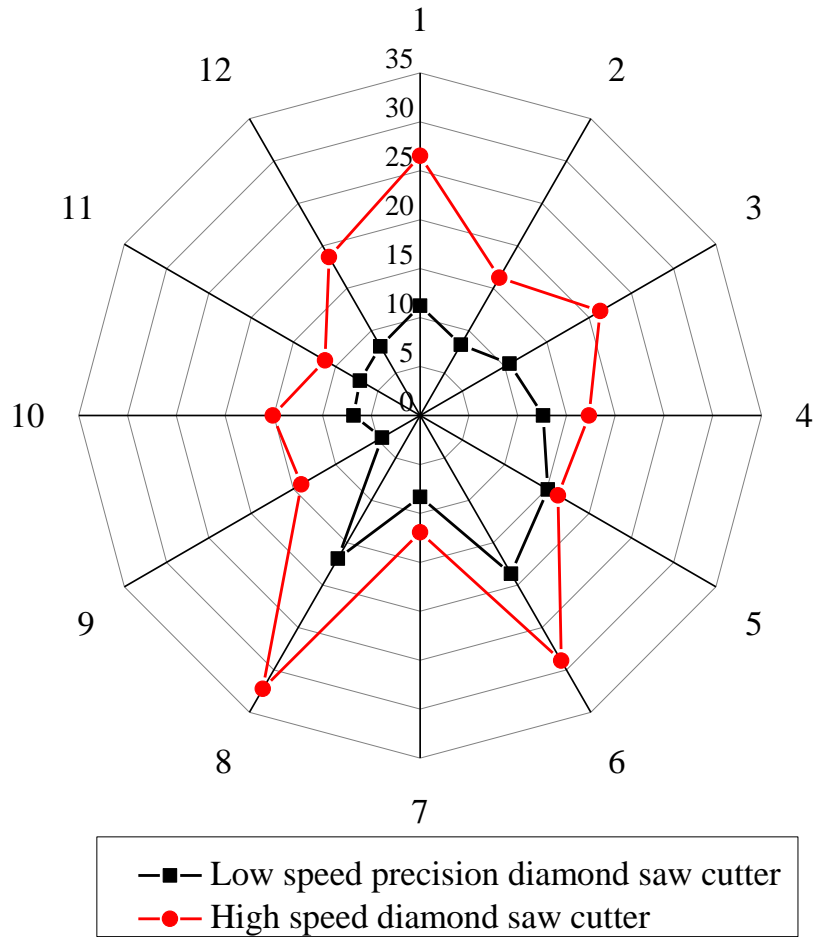
Figure 4.9: Variation of mean PZT (µm) at twelve spots around the steel bar cut with a low-speed precision diamond saw cutter and high-speed diamond saw cutter

For the same sample, the measured value of PZT for high-speed diamond saw cutter was comparatively more than the low-speed precision diamond saw cutter. The average value of PZT measured at twelve spots around SCI for low-speed precision diamond saw cutter and high-speed diamond saw cutter are 10.69 µm and 19.16 µm, respectively. The measured value of PZT around SCI increased by around 1.8 times when cutting the RC samples with a high-speed diamond saw cutter as compared to a low-speed precision diamond saw cutter. It can be observed that for high-speed diamond saw cutter, maximum values of PZT (at twelve spots) are quite higher than low-speed precision

diamond saw cutter. Amongst twelve spots, the maximum values of PZT of 46.78 μm was observed for high-speed diamond saw cutter, whereas, for low-speed precision diamond saw cutter it was found to be 28.41 μm. It prevails that RC samples cut with a high-speed diamond saw cutter will result in higher PZT around SCI. This can be attributed to the uncontrolled vibrations due to the variation in hardness values of steel and concrete. In addition, heat generated during high-speed diamond saw cutter may also aid to incorrect measurement of PZT around SCI. In case of low-speed precision diamond saw cutter, heat generated and vibrations are very less and hence damage associated with SCI was minimal.

4.4 EFFECT OF SPEED OF CUTTING THE SAMPLE ON NANO MECHANICAL PROPERTIES OF STEEL-CONCRETE INTERFACE

4.4.1 Variation in hardness property

The hardness and elastic modulus properties around SCI was studied by nano-indentation technique. Differences in measured values of hardness and elastic modulus around SCI when RC samples cut with a high-speed diamond saw cutter (3200 rpm) and low-speed precision diamond saw cutter (100 rpm) is analyzed. The nano-mechanical property, i.e. H-hardness, around SCI was measured at six locations as shown in Figure 3.18. Figure 4.10 shows the comparison of H-hardness values around the steel surface at a distance of 0 μm, 20 μm, 40 μm and 60 μm, when RC samples cut with a high-speed diamond saw cutter and low-speed precision diamond saw cutter. A progressive increase in hardness values were noticed away from the steel surface towards the bulk concrete, the presence of denser concrete increases the hardness value. Lower hardness at SCI (approximately at '0 μm') can be attributed to porous region formed because of the wall effect (Horne, Richardson and Brydson, 2007; Allison *et al.*, 2012; Xiao *et al.*, 2013).
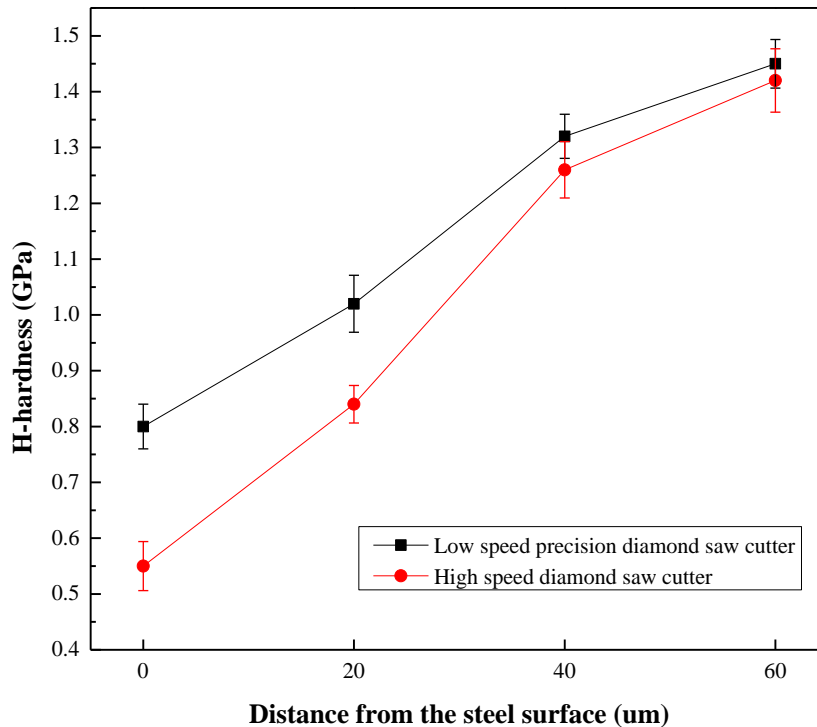
Figure 4.10: Comparison of H-hardness values around the steel surface at a distance of 0 μm, 20 μm, 40 μm and 60 μm, when the reinforced concrete samples cut with two types of cutters (Note: each point shows the mean value of 30 measurements)

For the same sample, measured H-hardness value at SCI when cutting with a high-speed diamond saw cutter was comparatively lesser when compared to low-speed precision diamond saw cutter. This can be attributed to uncontrolled vibrations produced due to the variation in hardness values of steel and concrete. Vibrations and heat generated during the slice cutting process loosen the surrounding porous concrete which resulted in lower hardness values at SCI (up to 40 μm) in nano-indentation testing. After 40 μm distance from the steel surface, hardness values become relatively constant for both high-speed diamond saw cutter and low-speed precision diamond saw cutter. The hardness value at the weakest point (at approximately 0 μm distance from steel surface) is 0.545 GPa and 0.810 GPa for high-speed diamond saw cutter and low-speed precision diamond saw cutter, respectively. In case of low-speed precision diamond saw cutter, heat generated

and vibrations were very less and damage associated to SCI was minimal, hence, average hardness value of 0.8 GPa can be considered as interface hardness between steel and concrete. It is to be noted that similar hardness values around steel-mortar interface were reported by other researchers (Wang *et al.*, 2009; Allison *et al.*, 2012; Zhao, Dai and Jin, 2012; Zhao *et al.*, 2016).

4.4.2 Variation in modulus of elasticity

The nano-elastic property, i.e. E-elastic modulus around SCI was measured at six locations as shown in Figure 3.18. The indents were 20 µm away in the perpendicular direction from the steel surface and 10 µm away from each other in the parallel direction, which does not influence each other with E-elastic modulus measurements (Wang *et al.*, 2009). Figure 4.11 shows the comparison of E-elastic modulus values around the steel surface at a distance of 0 µm, 20 µm, 40 µm and 60 µm, when the reinforced concrete samples cut with a high-speed diamond saw cutter and low-speed precision diamond saw cutter.

A progressive increase in E-elastic modulus values were noticed away from the steel surface towards the bulk concrete, presence of denser concrete away from the interface increases the E-elastic modulus values. Practically, mean E-elastic modulus values for calcium hydroxide was reported in the range of 35 - 40 GPa (Zacharda, Štemberk and Němeček, 2018). Even though, a large amount of calcium hydroxide was present around SCI (Page, 1975; Horne, Richardson and Brydson, 2007), measured modulus values were lower due to porous region formed because of the wall effect around SCI (Wang *et al.*, 2009; Allison *et al.*, 2012). However, presence of denser concrete away from the interface increases the modulus value.
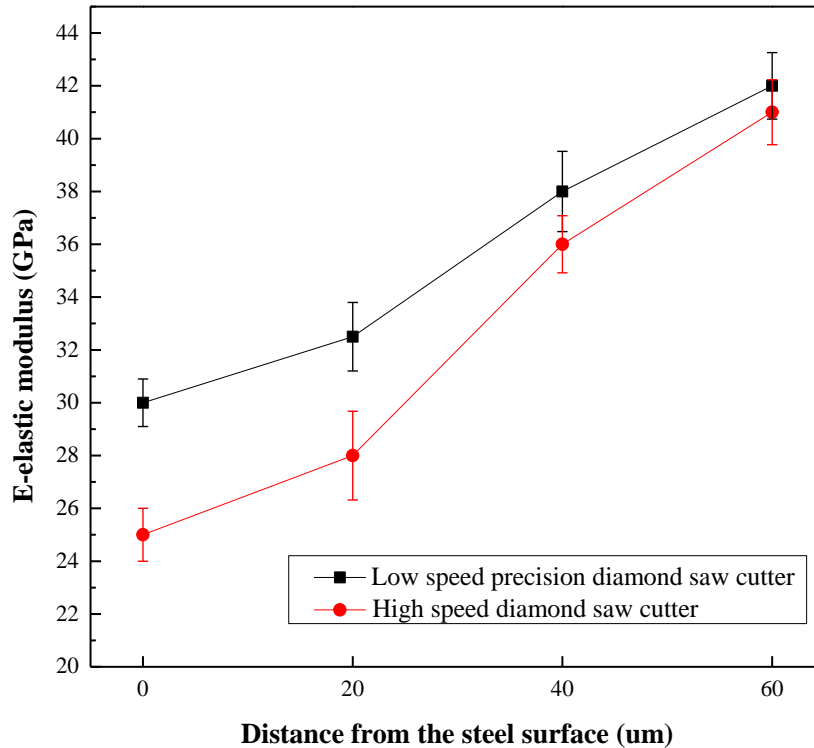
Figure 4.11: Comparison of E-elastic modulus around the steel surface at a distance of 0 μm, 20 μm, 40 μm and 60 μm, when the reinforced concrete samples cut with two types of cutters (Note: each point shows the mean value of 30 measurements)

The measured E-elastic modulus value at SCI, when cutting with a high-speed diamond saw cutter was relatively lesser as compared to specimens cut with a low-speed precision diamond saw cutter. The reduction in E-elastic modulus values of specimens cut with a high-speed diamond saw cutter may be attributed to the uncontrolled vibrations produced because of the variation in hardness values of steel and concrete. Up to a distance of 40 μm from the steel surface, there found to be a large difference in modulus values. After 40 μm distance from the steel surface, the E-elastic modulus values become fairly constant for both high-speed diamond saw cutter and low-speed precision diamond saw cutter. E-elastic modulus value at the weakest point (at approximately 0 μm distance from the steel surface) was 25 GPa and 30 GPa for the high-speed diamond saw cutter and low-speed precision diamond saw cutters, respectively. Similar E-elastic modulus

values around the steel-mortar interface were reported by Wang *et al.*, (2009) and Allison *et al.*, (2012). In case of low-speed precision diamond saw cutter, heat generated and vibrations were very less and damage associated to SCI was minimal, hence, average E-elastic modulus value of 30 GPa can be considered as interface modulus between steel and concrete.

4.5 STANDARD PROCEDURE OF SAMPLE PREPARATION TECHNIQUE FOR REDUCING THE DAMAGE TO STEEL-CONCRETE INTERFACE

To obtain a flat polished surface with minimal damage to SCI, following steps may be followed. If RC sample is large, it is recommended to take desired size of core along with the reinforcement bar as shown in Figure 3.3 (c) (Chapter 3). Once the cores were obtained, the next step is cutting the cores to get flat cross-sections without much damage to SCI. To ensure the minimal damage to SCI, obtained cores along with reinforcement bars were encased within 40 mm Polyvinyl chloride (PVC) pipes. And then 8 mm gap was filled by epoxy resin hardener (Acrylic powder and resin-based hardener) as shown in Figure 4.12 (d). The epoxy resin hardener ensures firm grip while cutting cores to obtain the cross-sections. As epoxy resin hardener sets (usually takes one hour), the next step is cutting the RC core along with PVC pipe and epoxy resin hardener.

A low-speed precision diamond saw cutter with cutting speed of 100 - 200 rpm should be used. The high-speed cutters will damage the properties of SCI. Also, as thickness of the specimen gets smaller, damage incurred to SCI will be higher. To avoid these artifacts, a minimum thickness of specimens must be 10 mm and can be considered more depending upon the requirements of SEM sample holder dimensions. The cross section of slice cut RC specimen can be observed in Figure 4.12 (f) which is 10 mm thick and 40 mm in diameter.

The next step is to mould the specimens with ultralow viscosity epoxy. The specimens should be moulded with ultralow viscosity epoxy under vacuum for a period of minimum two hours. Followed by that, specimens should be left to harden under room temperature (27 ± 2°C) for 24 hours. The next process is oven drying of epoxy and care needs to be

taken as overheating might induce micro-cracks around SCI. And to dry epoxy, a temperature of lower than 60 ℃ may be used for a period of 1 hour to avoid drying shrinkage cracks which causes due to the differences in thermal expansion of heterogeneous materials in concrete.

Further, specimens need to undergo a grinding and polishing process in an advanced polishing machine where polishing pressure can be controlled. The first three grinding steps with silicon carbide papers of different grades (P320, P600 and P1000) was set to three minutes (one minute for each step). And the two polishing steps using non-aqueous solutions with diamond particles of 0.25 μm and 0.15 μm were set to 2 minutes (one minute for each step). The grinding and polishing force was maintained at 25 kN. The sample after the grinding and polishing process need to be stored in desiccators till the day of SEM examination. For SEM observations, all the specimens in the present investigation were prepared in the same way. Based on the observations of this experimental research work, the factors that are vital for the sample preparation for a reinforced concrete sample along with the range of their values which should to be considered are summarized in Table 4.2.
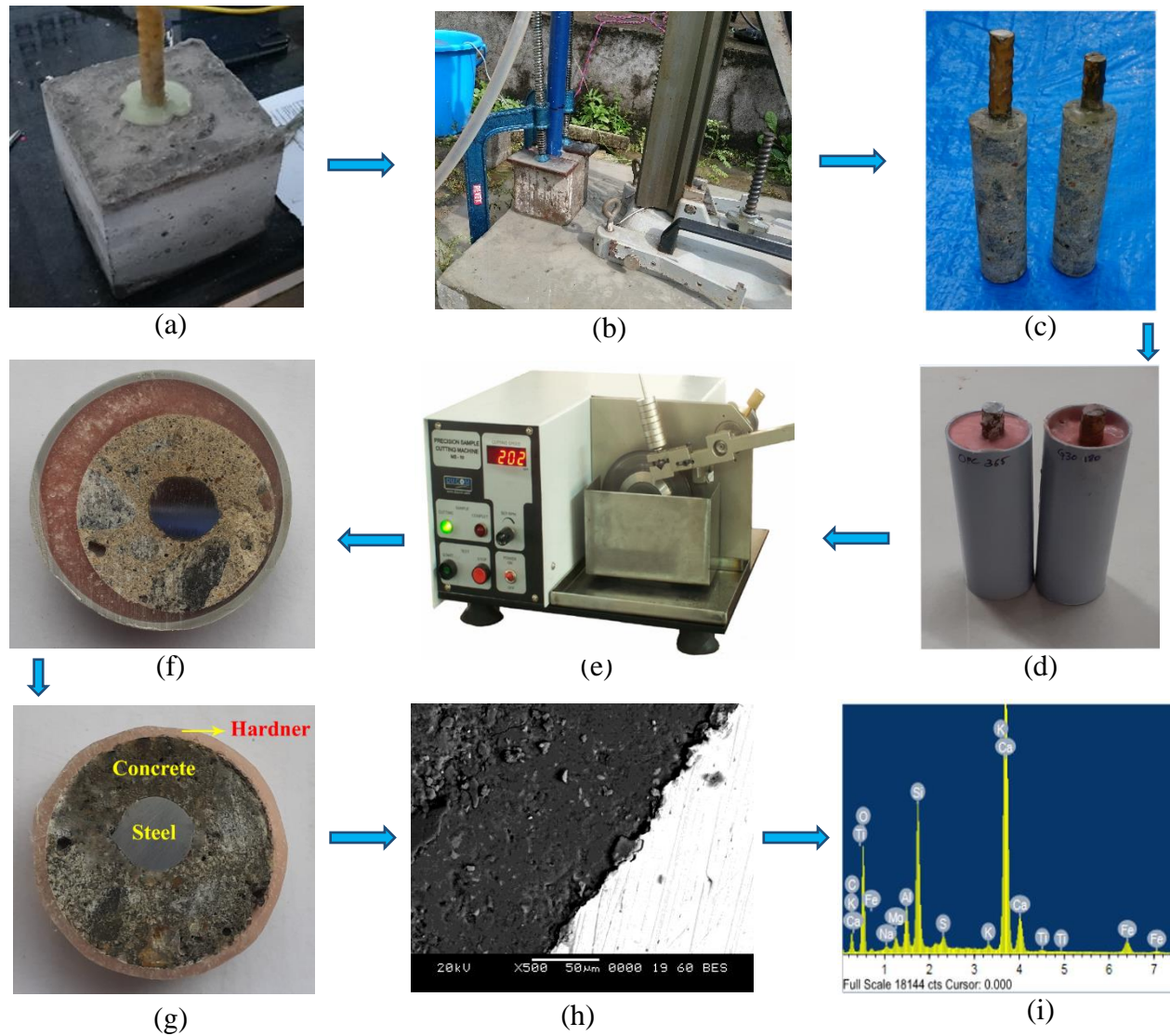
Figure 4.12: Standard procedure of sample preparation technique, (a) RC sample, (b) obtaining core, (c) 32 mm diameter cores along with reinforcement bar, (d) 32 mm cores encased within PVC pipe along with epoxy resin hardener, (e) low-speed diamond saw cutter to cut the samples, (f) cross section of the specimen, (g) grinding and polishing, (h) SEM image and (i) EDS elemental map

Table 4.2: List of factors that affect the sample preparation for a reinforced concrete sample

Sl. No.	Factors	Recommended values	Remarks
1	RC Sample collection	A desired size of concrete core along with reinforcement bar	The size of core depend upon the sample holder dimensions of SEM
2	Preparation of slices from cored RC samples	A low-speed precision diamond saw cutter of speed 100 – 200 rpm with blade thickness not more than 0.5 mm	High-speed diamond saw cutters will significantly damage the properties of SCI
3	Thickness of specimen	Larger the better, however, minimum thickness of slice need to be 10 mm	The maximum thickness of specimen may be varied depending upon safe working distance in SEM vacuum chamber
4	Vacuum impregnation of specimens with ultralow viscosity epoxy	Minimum two hours of epoxy impregnation under vacuum	Epoxy impregnated specimens should be left to harden at room temperature for 24 hours
5	Oven drying of epoxy impregnated specimen	The epoxy drying temperature should not be more than 60 °C for a period of 1 hour	Higher epoxy drying temperatures will induce drying shrinkage cracks at SCI
6	Grinding of specimens	Total grinding duration should be less than three minutes with silicon carbide papers of grades P320, P600 and P1000	Pressing force while grinding need to be less than 25 kN
7	Polishing of specimens	Total polishing duration should be less than two minutes with non-aqueous solution of diamond particles (0.25 µm and 0.15 µm)	Pressing force while polishing need to be less than 25 kN
8	Storage of specimens	Specimens should be stored in desiccators till the day of SEM examination	No contact of specimens with external environment till the day of SEM examination

CHAPTER – 5

INFLUENCE OF CURING DURATION ON THE PROPERTIES OF STEEL-CONCRETE INTERFACE

5.1 GENERAL

The influence of curing duration on compressive strength, ultimate bond strength and the properties of SCI are analysed. The changes in PZT and hydration products of SCI was investigated as a function of curing duration. The changes in the hydration products at SCI was investigated using EDS analysis. The relation between ultimate bond strength and PZT as well as Ca/Si ratio was investigated.

5.2 COMPRESSIVE STRENGTH DEVELOPMENT OF OPC, PPC, AND PSC CONCRETES

Figure 5.1 presents the compressive strength of OPC, PPC, and PSC concrete mixes which were water cured for 28, 56, 90, 180 and 360-days. Compressive strength increased in parallel with the increase in curing periods for all the mixes. However, the compressive strengths of PPC and PSC concrete mixes were lower during the initial curing periods (up to 90-days curing) compared with OPC concrete mixes, which can be attributed to the faster hydration rate of OPC mixes compared with PPC and PSC concrete mixes. However, as the curing period increased beyond 90-days, because of pozzolanic reactions, strength gains of PPC and PSC concrete mixes were comparable with OPC concrete mixes. If 28-days of water curing is considered as a reference point for strength indication, OPC concrete mixes had 5.9 and 11.7 % higher compressive strength than PPC and PSC concrete mixes, respectively. On the other hand, at 360-days of water curing, compressive strength of PSC concrete mixes was 4.5 % and 3.1 % higher than that of OPC and PPC mixes, respectively. The higher percentage increase in

compressive strength of PSC concrete is attributed to faster rate of pozzolanic reaction when compared to PPC mixes (Das, Singh and Pandey, 2011).
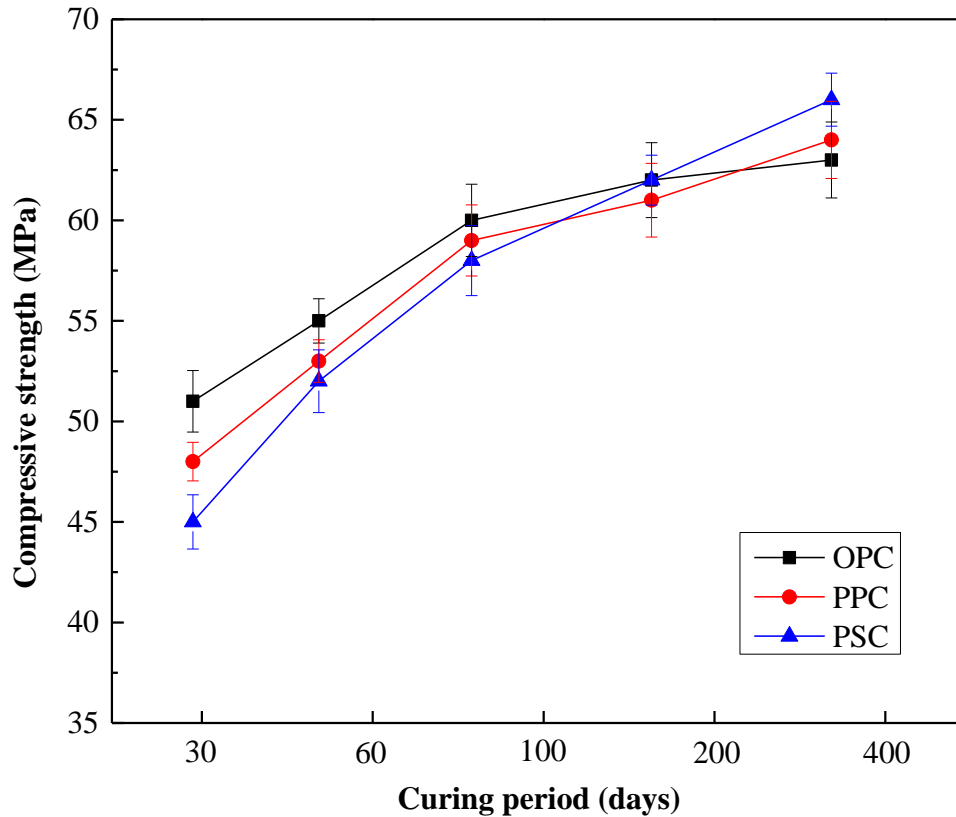
Figure 5.1: Compressive strength development of OPC, PPC and PSC concrete with respect to curing period of up to 360-days

5.3 ULTIMATE BOND STRENGTH DEVELOPMENT OF OPC, PPC, AND PSC CONCRETES

Figure 5.2 presents the ultimate bond strength of OPC, PPC, and PSC concrete mixes which were water cured for 28, 56, 90, 180 and 360-days. Curing period has a significant influence on the ultimate bond strength of RC. At 28-days of water curing, all the mixes showed similar ultimate bond strength values. However, for prolonged curing, PPC and PSC concrete mixes showed significant improvements in ultimate bond strength values.

As the curing period increased from 28 to 360 days, an increase in ultimate bond strength of 22.2 %, 27.2 %, and 29.5 % was observed for OPC, PPC, and PSC concrete mixes, respectively. The higher percentage of bond strength gain for PPC and PSC mixes can be attributed to the fineness of cement particles as well as pozzolanic reactions. At 90-days of curing, PSC concrete mixes showed 7.4 % and 2.1 % higher ultimate bond strength than OPC and PPC concrete mixes, respectively. Also, at 360-days of curing, PSC concrete mixes showed 9.1 % and 4.5 % higher ultimate bond strength than OPC and PPC concrete mixes, respectively. The higher percentage increase in ultimate bond strength of PSC concrete is attributed to faster rate of pozzolanic reaction compared to PPC concrete (Das, Singh and Pandey, 2011).
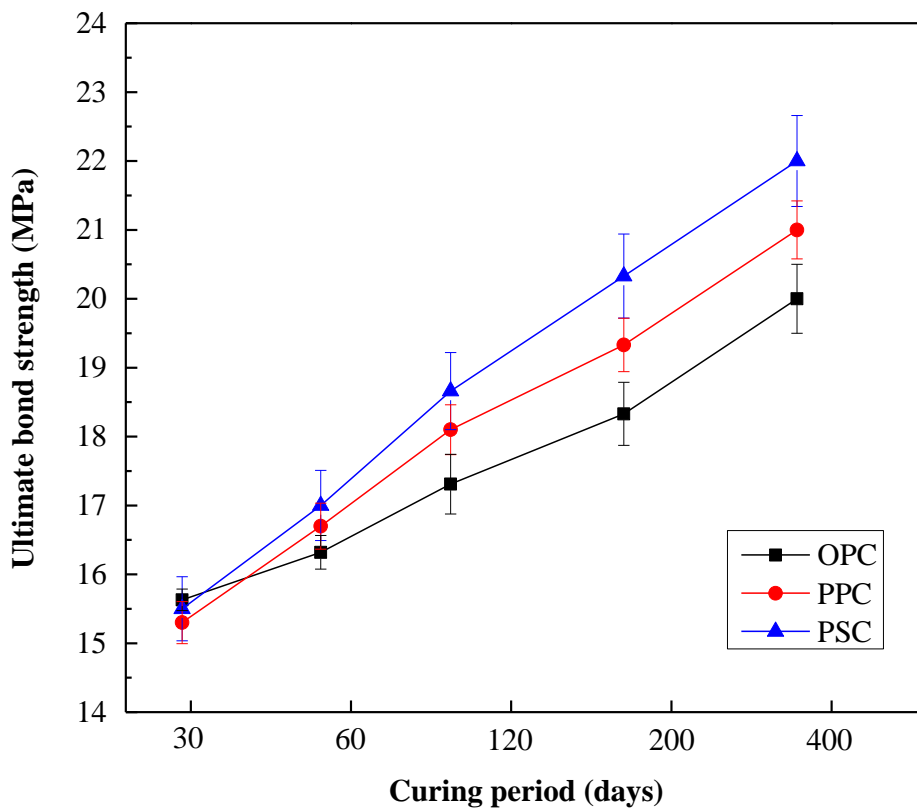
Figure 5.2: Ultimate bond strength development of OPC, PPC and PSC concrete with respect to curing period of up to 360-days

5.4 RELATIONSHIP BETWEEN COMPRESSIVE STRENGTH AND ULTIMATE BOND STRENGTH

The relationship between the ultimate bond strength (τ) and compressive strength (f_{ck}) of OPC, PPC, and PSC concrete samples are presented in Figure 5.3. It can be observed that there is a meaningful relationship between the compressive strength and ultimate bond strength for all three concrete mixes. As the compressive strength increases, the ultimate bond strength also increases significantly for OPC, PPC, and PSC concrete mixes. It can be noted from the regression analysis that there is a linear trend that fits very well with R^2 values of 0.9607, 0.9279 and 0.9678 for OPC, PPC, and PSC mixes, respectively. The linear equations obtained by regression analysis for OPC, PPC, and PSC concretes are given by equations (1), (2), and (3), respectively. It is to be noted that values of compressive strengths and ultimate bond strengths represented in Figure 5.3 are for the same concrete mixes at different curing ages.
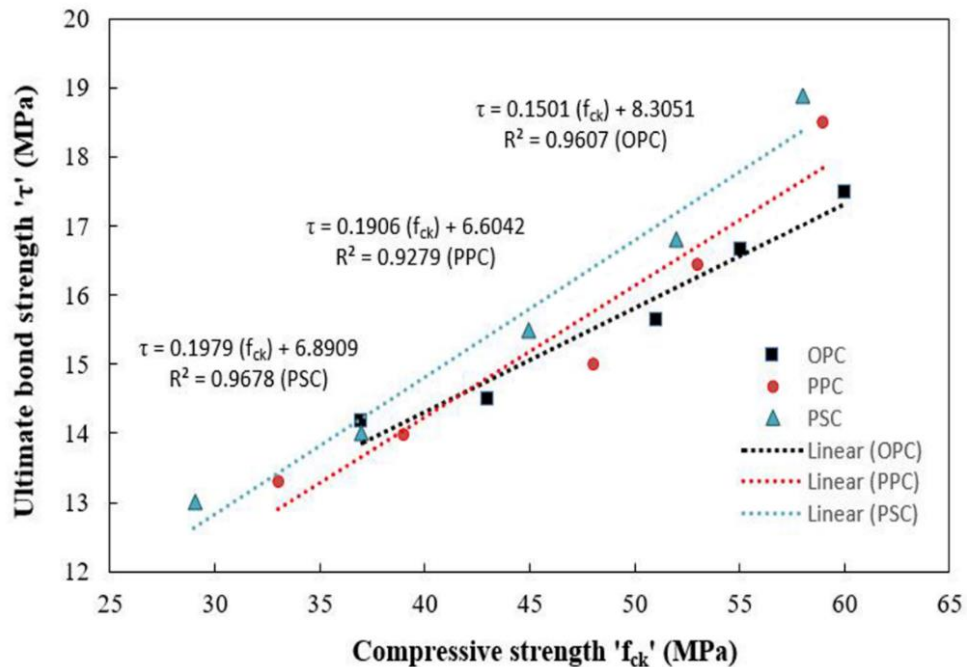
Figure 5.3: Relationship of bond strength and compressive strength of OPC, PPC, and PSC concrete

$$\tau = 0.1501\,(fck) + 8.3051 \tag{1}$$

$$\tau = 0.1906\,(fck) + 6.6042 \tag{2}$$

$$\tau = 0.1979\,(fck) + 6.8909 \tag{3}$$

5.5 EFFECT CURING DURATION ON POROUS ZONE THICKNESS AROUND STEEL-CONCRETE INTERFACE

Table 5.1 – 5.6 show the measured values of PZT of OPC, PPC and PSC concrete at twelve spots around SCI for 28, 90, 180 and 360-days water curing. The measurement of PZT from the BSE images was discussed in section 3.5 of chapter 3. The mean values of PZT shown in Tables 5.1 – 5.6 are the average of 30 measurements. The minimum and maximum values of porous zone thicknesses help to develop an accurate and dependable model to predict the time required to initiate corrosion cracking.

Figure 5.4 and 5.5 shows the spider chart of mean PZT of OPC, PPC, and PSC concrete at twelve spots around SCI for curing duration of up to 360-days. The reduction in PZT of all the mixes were noticed and with respect to curing period. It can be observed that mean PZT around the steel bar reduced because of the prolonged curing (up to 360-days). A similar fashion of reduction in PZT around SCI because of the prolonged curing was reported by Horne, Richardson and Brydson (2007). The variation in PZT around the steel bar was not uniform, which may be due to the wall effect (Chen *et al.*, 2019). At 28-days of curing, mean PZT values of OPC and PPC were comparable, and at the same time, PSC showed slightly higher values of PZT at few spots. As the curing period reached 90-days, the mean PZT of PSC concrete mixes was found to be reduced when compared with OPC and PPC concrete mixes. The reduction in PZT can be attributed to two factors, one being the fineness of PSC and the other being the faster rate of pozzolanic reaction, which might reduce the porosity at SCI. It was also found that prolonged curing up to 360-days has positive influence towards reducing PZT of all the mixes. The PSC and PPC concrete mixes showed relatively higher reduction in PZT when compared to OPC concrete mixes, which can be attributed to pozzolanic reactions.

Notably, PSC concrete showed significant reduction in PZT due to prolonged curing when compared to PPC concrete.

Table 5.1: Porous zone thickness of OPC Sample at 28-day and 90-days of curing

Location	Porous zone thickness of OPC Sample at 28-days of curing				Porous zone thickness of OPC Sample at 90-days of curing			
	Mean value (μm)	Standard deviation (μm)	Minimum value (μm)	Maximum value (μm)	Mean value (μm)	Standard deviation (μm)	Minimum value (μm)	Maximum value (μm)
Spot 1	11.22	5.32	4.31	21.66	6.32	2.31	4.02	18.34
Spot 2	8.34	3.44	6.34	18.72	7.51	2.44	2.62	22.31
Spot 3	10.59	4.56	2.79	42.74	12.05	1.14	3.13	20.66
Spot 4	12.61	6.12	4.12	21.86	13.25	6.62	4.12	28.69
Spot 5	15.12	4.33	6.32	28.41	6.32	1.22	2.32	10.63
Spot 6	18.66	5.29	3.02	26.92	16.79	4.37	3.16	20.88
Spot 7	8.32	3.34	6.33	15.62	7.49	5.32	4.18	28.47
Spot 8	3.14	0.61	2.31	6.12	5.34	3.18	3.66	20.26
Spot 9	4.52	1.59	1.28	7.07	4.07	0.24	2.18	9.65
Spot 10	6.8	2.36	3.02	10.66	5.11	1.26	2.66	8.41
Spot 11	7.12	3.33	2.16	11.22	6.41	1.88	3.78	15.36
Spot 12	8.16	4.34	1.69	20.86	8.69	2.16	5.06	25.64

Table 5.2: Porous zone thickness of OPC Sample at 180-day and 360-days of curing

Location	Porous zone thickness of OPC Sample at 180-days of curing				Porous zone thickness of OPC Sample at 360-days of curing			
	Mean value (µm)	Standard deviation (µm)	Minimum value (µm)	Maximum value (µm)	Mean value (µm)	Standard deviation (µm)	Minimum value (µm)	Maximum value (µm)
Spot 1	6.69	4.79	4.74	19.49	6.55	2.08	4.62	16.51
Spot 2	6.76	3.10	6.97	16.85	7.21	2.20	3.01	20.08
Spot 3	10.85	4.10	3.07	38.47	8.68	1.03	3.60	18.59
Spot 4	9.93	3.51	4.53	19.67	9.54	5.96	4.74	25.82
Spot 5	11.01	3.90	6.95	25.57	10.05	1.10	2.67	9.57
Spot 6	11.12	4.76	3.32	24.23	12.09	3.93	3.63	18.79
Spot 7	6.74	3.01	6.96	14.06	6.39	4.79	4.81	25.62
Spot 8	7.44	0.55	2.54	5.51	6.84	2.86	4.21	18.23
Spot 9	7.66	1.43	1.41	6.36	7.93	0.22	2.51	8.69
Spot 10	10.66	2.12	3.32	9.59	11.68	1.13	3.06	7.57
Spot 11	8.77	3.00	2.38	10.10	7.62	1.69	4.35	13.82
Spot 12	11.12	3.91	1.86	18.77	9.26	1.94	5.82	23.08

Table 5.3: Porous zone thickness of PPC Sample at 28-days and 90-days of curing

Location	Porous zone thickness of PPC Sample at 28-days of curing				Porous zone thickness of PPC Sample at 90-days of curing			
	Mean value (μm)	Standard deviation (μm)	Minimum value (μm)	Maximum value (μm)	Mean value (μm)	Standard deviation (μm)	Minimum value (μm)	Maximum value (μm)
Spot 1	10.66	4.88	3.25	19.33	5.88	1.93	3.76	15.59
Spot 2	6.22	2.66	5.66	15.36	6.98	2.04	2.45	18.96
Spot 3	13.54	5.36	4.21	25.36	11.21	0.95	2.93	30.57
Spot 4	10.11	3.22	3.66	24.21	12.32	5.54	3.86	20.14
Spot 5	18.14	5.89	4.36	32.33	10.58	1.02	2.17	7.62
Spot 6	15.97	4.66	5.87	24.88	12.35	3.66	2.96	17.75
Spot 7	7.66	2.34	2.55	14.11	6.97	4.45	3.91	24.20
Spot 8	5.13	1.31	2.34	10.36	4.55	2.66	3.43	17.22
Spot 9	2.33	0.36	2.01	10.25	3.79	0.20	2.04	8.20
Spot 10	8.77	3.25	4.21	18.66	10.66	1.05	2.49	17.15
Spot 11	11.32	2.33	3.33	26.33	5.96	1.57	3.54	13.06
Spot 12	6.11	1.78	2.55	16.88	11.34	1.81	4.74	21.79

Table 5.4: Porous zone thickness of PPC Sample at 180-days and 360-days of curing

Location	Porous zone thickness of PPC Sample at 180-days of curing				Porous zone thickness of PPC Sample at 360-days of curing			
	Mean value (μm)	Standard deviation (μm)	Minimum value (μm)	Maximum value (μm)	Mean value (μm)	Standard deviation (μm)	Minimum value (μm)	Maximum value (μm)
Spot 1	5.29	4.39	3.58	17.40	5.03	1.74	4.136	14.03
Spot 2	6.28	2.39	6.23	13.82	5.97	1.84	2.695	17.06
Spot 3	10.09	4.82	4.63	22.82	7.12	0.86	3.223	27.51
Spot 4	8.49	2.90	4.03	21.79	8.53	4.99	4.246	18.13
Spot 5	9.52	5.30	4.80	29.10	7.05	0.92	2.387	6.86
Spot 6	8.22	4.19	6.46	22.39	9.56	3.29	3.256	15.98
Spot 7	6.27	2.11	2.81	12.70	5.96	4.01	4.301	21.78
Spot 8	6.24	1.18	2.57	9.32	4.89	2.39	3.773	15.50
Spot 9	6.01	0.32	2.21	9.23	4.24	0.18	2.244	7.38
Spot 10	9.59	2.93	4.63	16.79	9.11	0.95	2.739	15.44
Spot 11	6.36	2.10	3.66	23.70	5.14	1.41	3.894	11.75
Spot 12	9.21	1.60	2.81	15.19	8.04	1.63	5.214	19.61

Table 5.5: Porous zone thickness of PSC Sample at 28-days and 90-days of curing

Location	Porous zone thickness of PSC Sample at 28-days of curing				Porous zone thickness of PSC Sample at 90-days of curing			
	Mean value (µm)	Standard deviation (µm)	Minimum value (µm)	Maximum value (µm)	Mean value (µm)	Standard deviation (µm)	Minimum value (µm)	Maximum value (µm)
Spot 1	8.65	4.15	3.53	13.72	5.80	1.53	2.36	10.65
Spot 2	11.63	2.26	1.92	20.01	6.89	1.61	3.40	15.32
Spot 3	8.21	3.66	3.11	18.01	11.05	0.75	3.24	25.98
Spot 4	7.30	2.74	2.33	17.19	12.15	4.38	3.66	20.36
Spot 5	16.33	3.21	2.73	22.95	10.44	0.81	2.06	16.31
Spot 6	11.31	3.96	3.37	17.66	6.34	2.89	2.81	15.09
Spot 7	13.68	2.71	2.30	25.68	6.87	3.52	3.72	20.57
Spot 8	6.32	2.14	1.82	10.25	4.49	2.10	1.12	14.64
Spot 9	1.11	0.08	0.07	5.21	3.73	0.16	1.94	6.97
Spot 10	6.32	3.11	2.64	13.25	10.51	0.83	3.34	14.58
Spot 11	13.58	1.98	1.68	18.69	5.88	1.24	3.36	11.10
Spot 12	10.14	2.40	2.04	16.98	11.18	1.43	4.50	18.52

Table 5.6: Porous zone thickness of PSC Sample at 180-days and 360-days of curing

Location	Porous zone thickness of PSC Sample at 180-days of curing				Porous zone thickness of PSC Sample at 360-days of curing			
	Mean value (μm)	Standard deviation (μm)	Minimum value (μm)	Maximum value (μm)	Mean value (μm)	Standard deviation (μm)	Minimum value (μm)	Maximum value (μm)
Spot 1	5.22	3.74	4.02	12.35	4.54	1.68	2.67	9.37
Spot 2	6.21	2.03	2.19	18.01	5.39	1.77	3.84	13.48
Spot 3	9.95	3.29	3.55	16.21	7.66	0.83	3.66	22.86
Spot 4	7.51	2.47	2.66	15.47	7.52	4.82	4.14	17.92
Spot 5	9.41	2.89	3.11	20.66	6.18	0.89	2.33	14.35
Spot 6	6.71	3.56	3.84	15.89	5.97	3.18	3.18	13.28
Spot 7	5.18	2.44	2.62	23.11	5.38	3.87	4.20	18.10
Spot 8	5.04	1.93	2.07	9.23	3.51	2.31	1.27	12.88
Spot 9	6.36	0.07	0.08	4.69	5.92	0.18	2.19	6.13
Spot 10	8.76	2.80	3.01	11.93	6.23	0.91	3.77	12.83
Spot 11	5.29	1.78	1.92	16.82	4.6	1.36	3.80	9.77
Spot 12	8.06	2.16	2.33	15.28	6.75	1.57	5.09	16.30
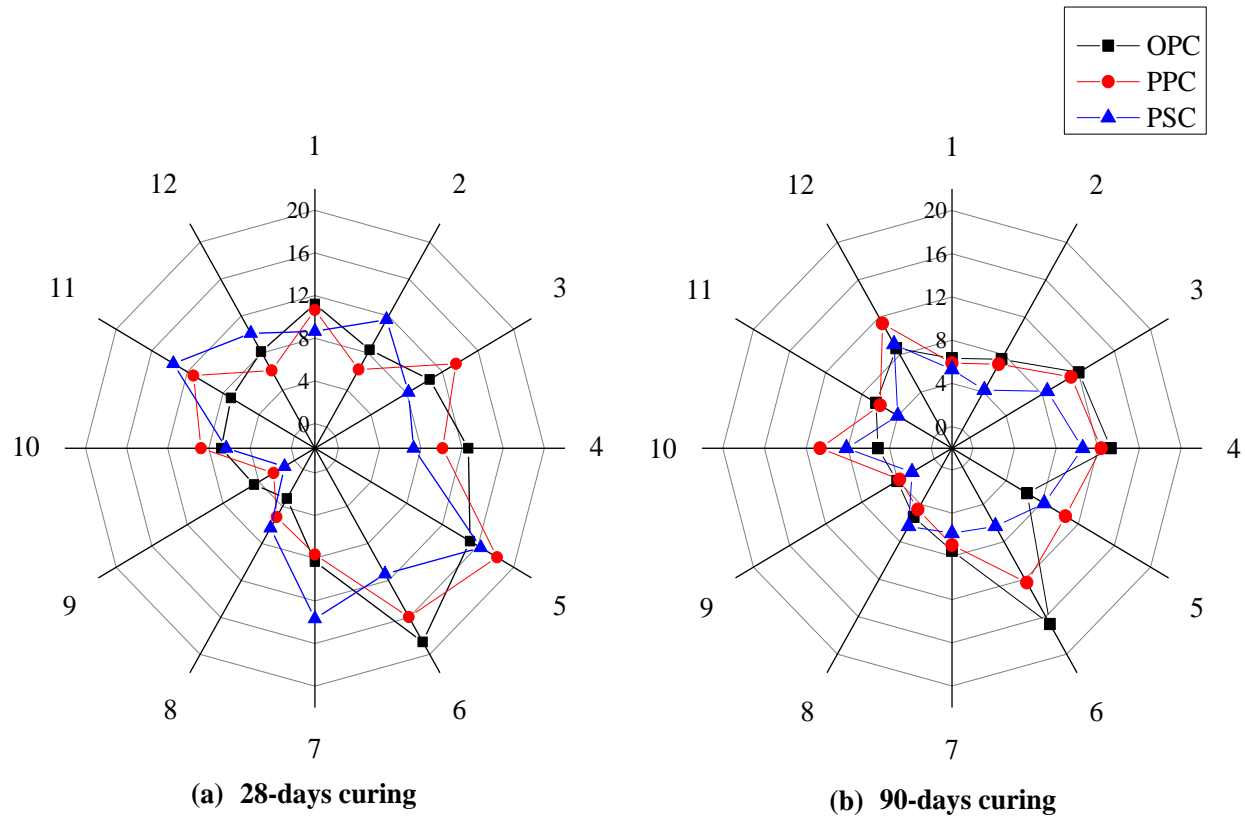
Figure 5.4: Variation of mean porous zone thickness (μm) of OPC, PPC and PSC concrete at twelve spots around the steel bar at (a) 28-days of curing and (b) 90-days of curing

(c) 180-days curing　　　　**(d) 360-days curing**
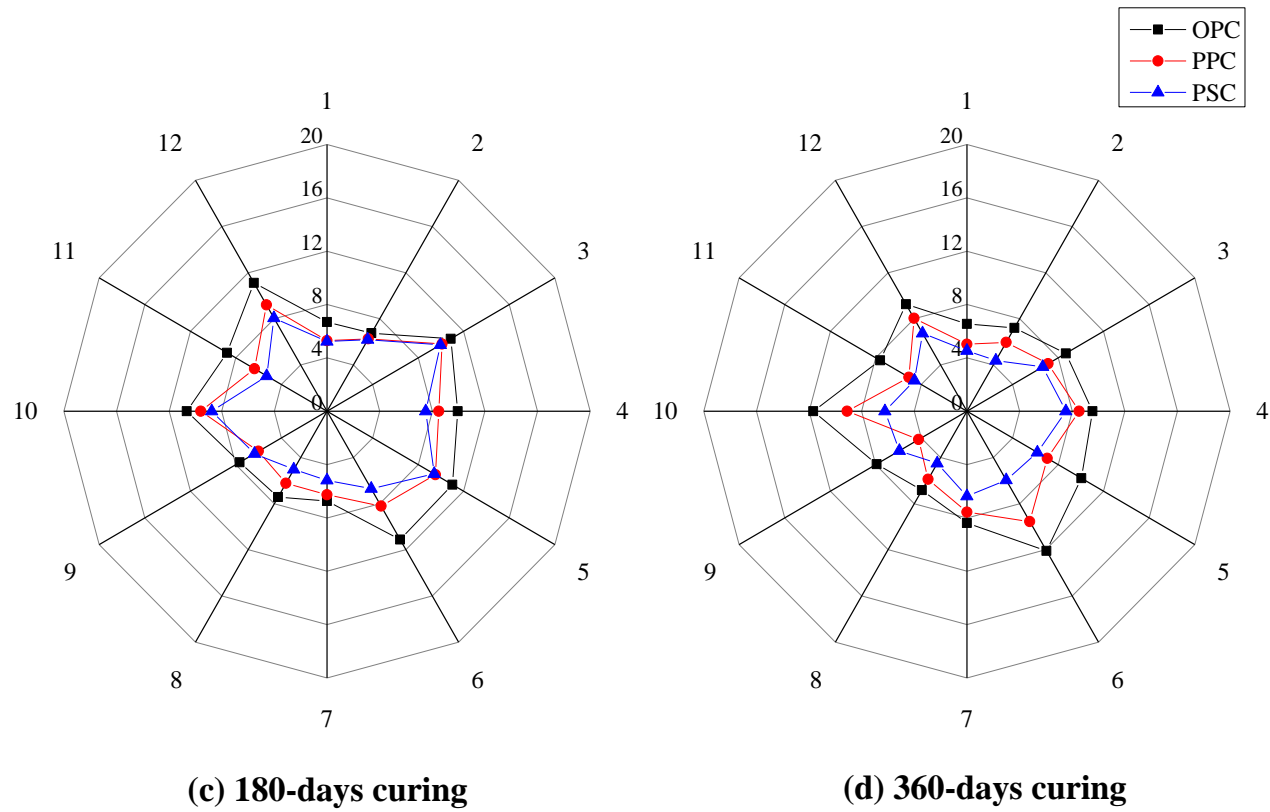
Figure 5.5: Variation of mean porous zone thickness (μm) of OPC, PPC and PSC concrete at twelve spots around the steel bar at (c) 180-days of curing and (d) 360-days of curing

5.6 EFFECT CURING DURATION ON THE EDS ANALYSIS AROUND STEEL-CONCRETE INTERFACE

The EDS analysis was carried out to identify the hydration compounds formed at SCI. From the EDS analysis, percentage atomic weights of different elements, such as carbon, oxygen, magnesium, aluminum, silicon, potassium, calcium, and iron, that were present in the mix were recorded and are listed in Tables 5.7 – 5.14 for 28, 90, 180 and 360-days of water curing with respect to distance from the steel surface. The representative spectrum of predominant calcium peaks and comparatively lesser silicon peaks with other phases of hydration products of OPC concrete at 28-days of curing can be seen in Figure 3.17 (Chapter 3). It was reported by many researchers that there was preferential formation of calcium hydroxide at SCI (Horne, Richardson and Brydson, 2007; C. L. Page, 2009; Kenny and Katz, 2012; Yu, François and Gagné, 2016). The presence of calcium hydroxide at SCI was confirmed by SEM images as well as EDS analysis in the present study. The atomic weights of the calcium/silicon (Ca/Si) ratio are an indication of the presence of calcium hydroxide or calcium silicate hydrate (C-S-H). It was reported that if the Ca/Si ratio is more than 1.7, it signifies the occurrence of calcium hydroxide. On the other hand, if the Ca/Si ratio is in the range of 0.7–1.7, it signifies the occurrence of C-S-H gel (Bentz, Stutzman and Garboczi, 1992; Isu, Ishida and Mitsuda, 1995; Escalante-Garcia, Mendoza and Sharp, 1999; Hiremath and Yaragal, 2017b). Considering this factor argued by previous researchers, the atomic ratio plots of the Ca/Si ratio (calculated from Tables 5.7 – 5.14) with respect to distance from steel were plotted for 28, 90, 180 and 360-days of water curing, which is presented in Figure 5.6. After 28-days of water curing, the Ca/Si ratio at SCI for OPC, PPC, and PSC concrete was 2.88, 2.44, and 2.40, respectively. These high values of Ca/Si ratios signify the presence and preferential formation of calcium hydroxide at SCI. It is of note that as the distance from the steel surface increases toward the bulk concrete, the Ca/Si ratio decreases, which signifies a decrease in calcium hydroxide content or increase in the formation of C-S-H gel. It was observed that Ca/Si at SCI is sensitive to prolonged curing period. As the curing period increased from 28-days to 360-days, there found to be significant reduction

in Ca/Si ratio of all the mixes. The reduction in Ca/Si ratio signifies the reduction in calcium hydroxide content at SCI.

Table 5.7: EDS elemental analysis of OPC, PPC and PSC concrete at a distance of '0 μm' from SCI after 28-days and 90-days of water curing

Elements	OPC		PPC		PSC	
	Atomic (%)		Atomic (%)		Atomic (%)	
	28-days curing	90-days curing	28-days curing	90-days curing	28-days curing	90-days curing
O	55.44	58.12	51.21	56.72	55.83	52.44
Al	1.78	2.06	2.38	1.95	2.25	3.06
Si	3.18	3.66	3.31	3.86	3.47	4.14
Mg	0.69	0.72	0.82	0.63	0.41	0.22
K	0.15	0.21	0.04	0.12	0.21	0.08
Ca	9.18	9.67	8.14	8.27	8.35	8.58
Fe	0.94	0.72	0.86	0.62	0.92	0.6
C	28.64	24.84	33.24	27.83	28.56	30.88
Ca/Si	**2.887**	**2.642**	**2.459**	**2.242**	**2.406**	**2.172**

Table 5.8: EDS elemental analysis of OPC, PPC and PSC concrete at a distance of '0 μm' from SCI after 180-days and 360-days of water curing

Elements	OPC		PPC		PSC	
	Atomic (%)		Atomic (%)		Atomic (%)	
	180-days curing	360-days curing	180-days curing	360-days curing	180-days curing	360-days curing
O	54.25	56.12	54.36	55.25	54.24	56.45
Al	2.40	2.1	1.48	1.87	2.71	3.22
Si	3.58	4.16	4.18	4.29	4.59	5.02
Mg	0.82	0.92	0.68	0.71	0.45	0.38
K	0.14	0.16	0.12	0.1	0.12	0.07
Ca	9.32	10.42	9.62	9.05	9.86	9.65
Fe	0.96	0.96	0.86	0.86	0.6	0.6
C	28.53	25.16	28.7	27.87	27.43	24.61
Ca/Si	**2.603**	**2.505**	**2.201**	**2.110**	**2.148**	**1.922**

Table 5.9: EDS elemental analysis of OPC, PPC and PSC concrete at a distance of '20 μm' from SCI after 28-days and 90-days of water curing

Elements	OPC		PPC		PSC	
	Atomic (%)		Atomic (%)		Atomic (%)	
	28-days curing	90-days curing	28-days curing	90-days curing	28-days curing	90-days curing
O	52.25	55.12	56.42	52.36	57.22	56.51
Al	2.67	2.82	4.05	4.85	3.82	4.21
Si	4.02	4.32	4.46	4.94	4.91	5.12
Mg	0.58	0.45	0.02	0.31	0.62	0.27
K	0.02	0.04	0.03	0.12	0.17	0.06
Ca	8.89	9.17	9.76	9.8	10.24	9.58
Fe	0.12	0.03	0.01	0.02	0.08	0.01
C	31.45	28.05	25.25	27.6	22.94	24.24
Ca/Si	**2.211**	**2.123**	**2.188**	**1.984**	**2.086**	**1.871**

Table 5.10: EDS elemental analysis of OPC, PPC and PSC concrete at a distance of '20 μm' from SCI after 180-days and 360-days of water curing

Elements	OPC		PPC		PSC	
	Atomic (%)		Atomic (%)		Atomic (%)	
	180-days curing	360-days curing	180-days curing	360-days curing	180-days curing	360-days curing
O	55.24	51.54	55.14	52.57	54.22	54.35
Al	2.81	2.95	5.35	1.88	2.54	4.05
Si	4.34	4.39	4.87	4.44	5.12	5.46
Mg	1.14	0.02	0.12	0.12	0.55	0.58
K	0.07	0.02	0.07	0.07	0.04	0.02
Ca	9.33	9.88	10.55	9.02	10.55	10.18
Fe	0.04	0.01	0.22	0.02	0.05	0.08
C	27.13	31.19	23.68	31.88	26.93	25.28
Ca/Si	**2.310**	**2.251**	**2.166**	**2.032**	**2.061**	**1.864**

Table 5.11: EDS elemental analysis of OPC, PPC and PSC concrete at a distance of '40 μm' from SCI after 28-days and 90-days of water curing

Elements	OPC		PPC		PSC	
	Atomic (%)		Atomic (%)		Atomic (%)	
	28-days curing	90-days curing	28-days curing	90-days curing	28-days curing	90-days curing
O	52.57	56.22	55.47	52.55	55.31	54.33
Al	1.88	1.86	4.65	5.68	5.37	6.21
Si	4.24	4.72	4.52	4.7	5.16	5.42
Mg	0.12	0.91	0.14	0.33	0.21	0.34
K	0.07	0.10	0.03	0.12	0.01	0.2
Ca	8.99	9.64	8.87	8.72	10.34	9.88
Fe	0.02	0.01	0.01	0.01	0.01	0.04
C	32.11	26.54	26.31	27.89	23.58	23.58
Ca/Si	**2.120**	**2.042**	**1.962**	**1.855**	**2.004**	**1.823**

Table 5.12: EDS elemental analysis of OPC, PPC and PSC concrete at a distance of '40 μm' from SCI after 180-days and 360-days of water curing

Elements	OPC		PPC		PSC	
	Atomic (%)		Atomic (%)		Atomic (%)	
	180-days curing	360-days curing	180-days curing	360-days curing	180-days curing	360-days curing
O	55.32	55.21	52.33	55.44	53.21	55.47
Al	2.04	2.12	4.28	5.22	5.74	6.43
Si	4.68	4.96	5.11	5.54	5.71	5.92
Mg	0.32	0.85	0.94	0.47	0.14	0.22
K	0.04	0.04	0.22	0.11	0.07	0.04
Ca	9.76	9.87	9.74	10.02	10.55	10.55
Fe	0.04	0.08	0.04	0.02	0.04	0.07
C	27.8	26.87	27.an 34	23.18	24.54	21.3
Ca/Si	**2.085**	**1.990**	**1.906**	**1.809**	**1.848**	**1.782**

Table 5.13: EDS elemental analysis of OPC, PPC and PSC concrete at a distance of '60 µm' from SCI after 28-days and 90-days of water curing

Elements	OPC Atomic (%)		PPC Atomic (%)		PSC Atomic (%)	
	28-days curing	90-days curing	28-days curing	90-days curing	28-days curing	90-days curing
O	51.44	54.36	52.88	58.21	52.44	56.77
Al	2.12	2.16	5.22	6.44	6.84	8.64
Si	4.58	4.91	4.75	5.04	5.38	5.56
Mg	0.24	0.41	0.11	0.23	0.28	0.11
K	0.03	0.01	0.03	0.31	0.22	0.04
Ca	8.26	8.71	8.43	8.61	9.17	9.39
Fe	0.01	0.01	0.01	0.02	0.01	0.01
C	33.32	29.43	28.57	21.14	25.66	19.48
Ca/Si	**1.803**	**1.774**	**1.775**	**1.708**	**1.704**	**1.689**

Table 5.14: EDS elemental analysis of OPC, PPC and PSC concrete at a distance of '60 µm' from SCI after 180-days and 360-days of water curing

Elements	OPC Atomic (%)		PPC Atomic (%)		PSC Atomic (%)	
	180-days curing	360-days curing	180-days curing	360-days curing	180-days curing	360-days curing
O	55.24	52.36	55.55	54.21	55.65	52.47
Al	4.24	4.54	5.65	5.78	6.22	7.54
Si	5.95	6.24	6.23	6.47	6.38	7.12
Mg	0.13	0.21	0.24	0.11	0.17	0.41
K	0.04	0.04	0.05	0.04	0.06	0.07
Ca	10.68	10.87	10.49	10.61	10.22	11.23
Fe	0.01	0.07	0.03	0.02	0.03	0.07
C	23.71	25.67	21.76	22.76	21.27	21.09
Ca/Si	**1.795**	**1.742**	**1.684**	**1.640**	**1.602**	**1.577**
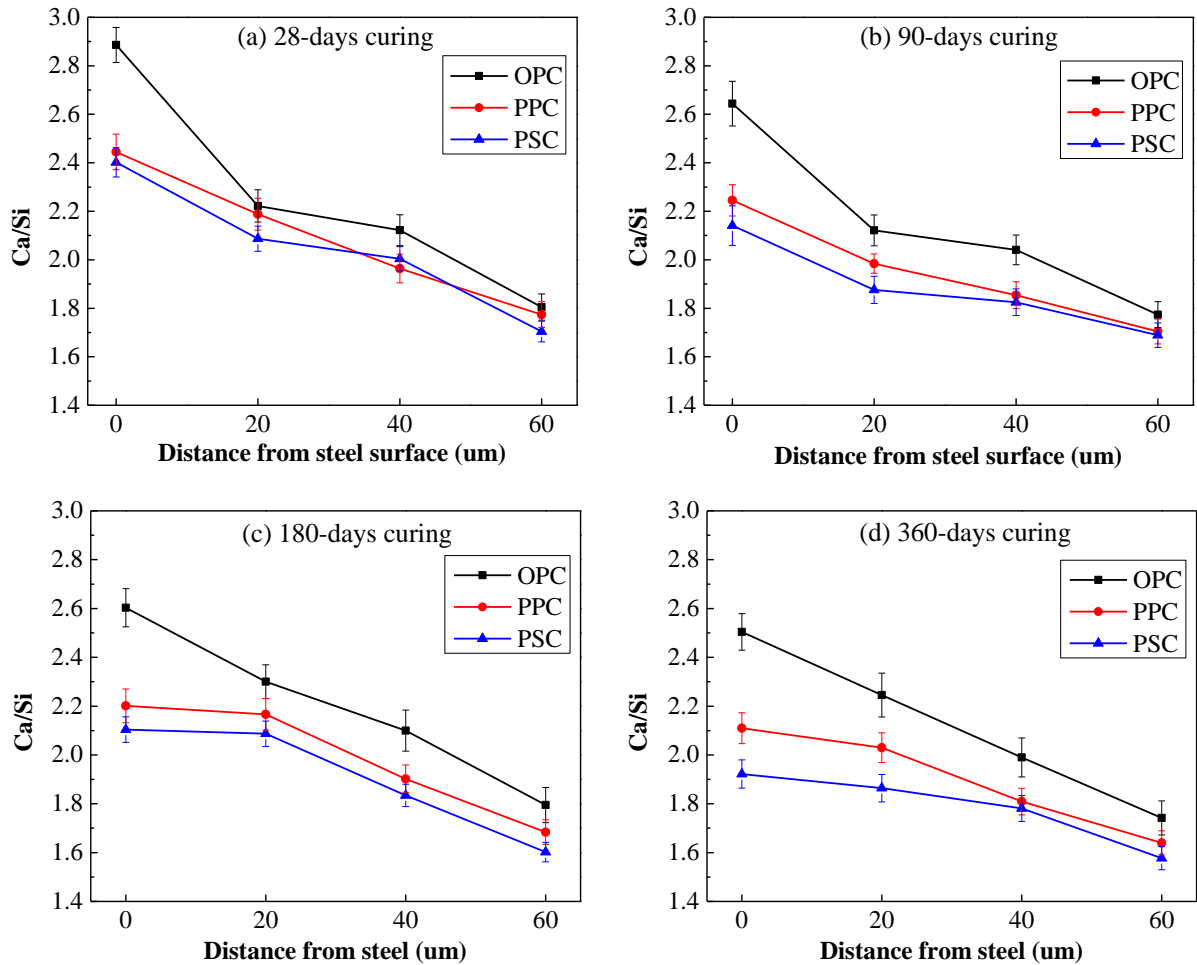
Figure 5.6: Plot of Ca/Si ratio with respect to distance from the steel surface for (a) 28-days of curing, (b) 90-days of curing, (c) 180-days curing and (d) 360-days curing

It can be observed that the value of the Ca/Si ratio considered at SCI for PPC and PSC concrete is comparatively less than OPC concrete. This can be attributed to the pozzolanic reaction that consumes calcium hydroxide at SCI. Similarly, after 28-days of water curing, the values of the Ca/Si ratio for PPC and PSC concretes reduced considerably, which can be justified from the advancement of the pozzolanic reaction and possible formation of more secondary C-S-H gel, which strengthens the interfacial transition zone. A similar trend that showed a reduction of calcium hydroxide content away from SCI toward the bulk concrete was reported by doing BSE image analysis

(Horne, Richardson and Brydson, 2007). Prolonged curing up to 360-days is found to be beneficial to the properties of SCI especially the reduction in Ca/Si ratio, that is with the reduction in calcium hydroxide, interfacial transition zone between steel and concrete gets strengthened.

5.7 ULTIMATE BOND STRENGTH AND POROUS ZONE THICKNESS

The OPC concrete showed a relatively smaller mean PZT at 28-days of curing as compared to PPC and PSC concretes. A similar trend was also observed in ultimate bond strength values for OPC concrete, which was found to be slightly higher than for PPC and PSC concrete. At 90-days of curing, OPC concrete showed minimal changes in mean PZT values. However, the changes in mean values of PZT of concrete with PPC and PSC were found to be quite significant at 90-days of curing, which can be attributed to pozzolanic reactions in PPC and PSC concrete. Further reduction in PZT was noticed due to prolonged curing up to 360-days. As compared with OPC and PPC, PSC concrete at 360-days showed a significant reduction in mean PZT values (refer Figure 5.5). It was also observed that ultimate bond strength values were found to be higher for PSC concrete compared with PPC and OPC concrete at 360-days of curing. Reduction in PZT might be one of the many reasons for increased ultimate bond strength of all the mixes at 360-days of prolonged curing. A similar kind of observation is reported by the previous researcher (Horne, Richardson and Brydson, 2007) confirming the results of the present investigation.

5.8 RELATIONSHIP BETWEEN ULTIMATE BOND STRENGTH AND Ca/Si RATIO

The ultimate bond strength values for different types of concrete were plotted with the measured values of the Ca/Si ratio at '0 μm' distance from steel surface are presented in Figure 5.7 and Figure 5.8 for 28, 90, 180 and 360-days of curing. It can be noted from the figure that the Ca/Si ratio has influence on the ultimate bond strength of concrete. The Ca/Si ratio at 28-days of water curing was 2.88, 2.45, and 2.40, and the corresponding

ultimate bond strength was 15.6, 15.3, and 15.5 MPa for OPC, PPC, and PSC concrete, respectively. At 90-days of curing, the Ca/Si ratios were 2.64, 2.14, and 2.07, and the corresponding ultimate bond strengths were 17.3, 18.5, and 18.9 MPa for OPC, PPC, and PSC, respectively. Furthermore, at 360-days of curing, the Ca/Si ratios were 2.50, 2.11, and 1.92, and the corresponding ultimate bond strengths were 19.3, 21.1, and 22.1 MPa for OPC, PPC, and PSC, respectively. With the decrease in the value of the Ca/Si ratio (which is also a function of curing time), the ultimate bond strength value was found to be increased. This is noticeable for all three types of cement.
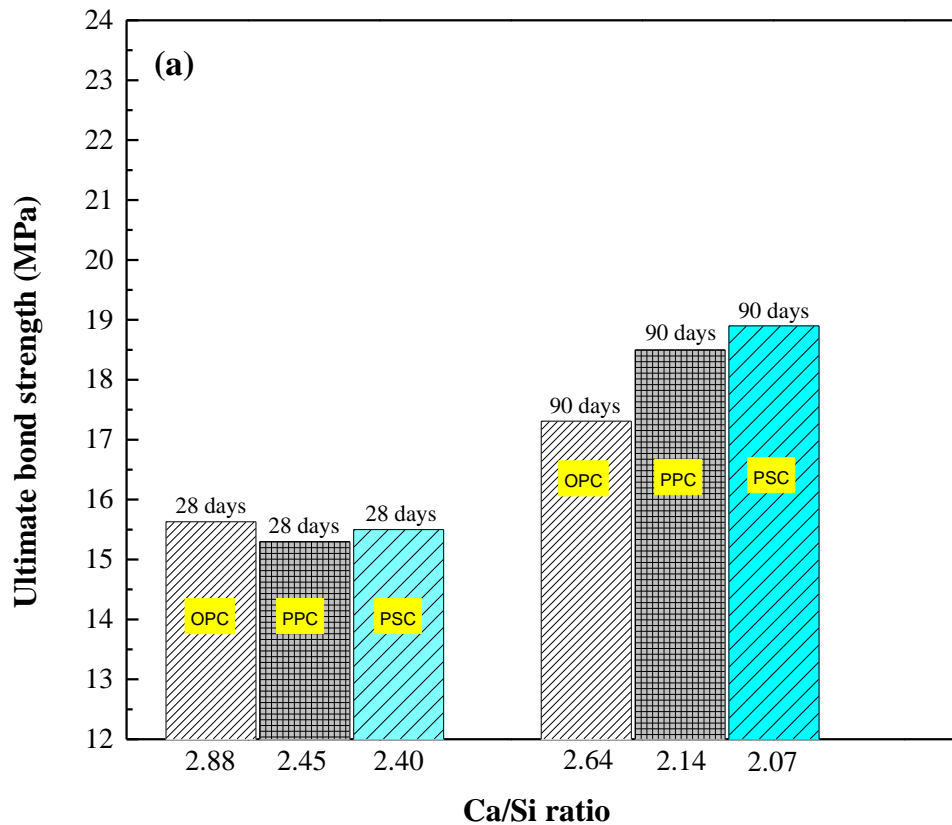
Figure 5.7: Ultimate bond strength and Ca/Si ratio at SCI (0 μm distance) for 28 and 90-days of water curing
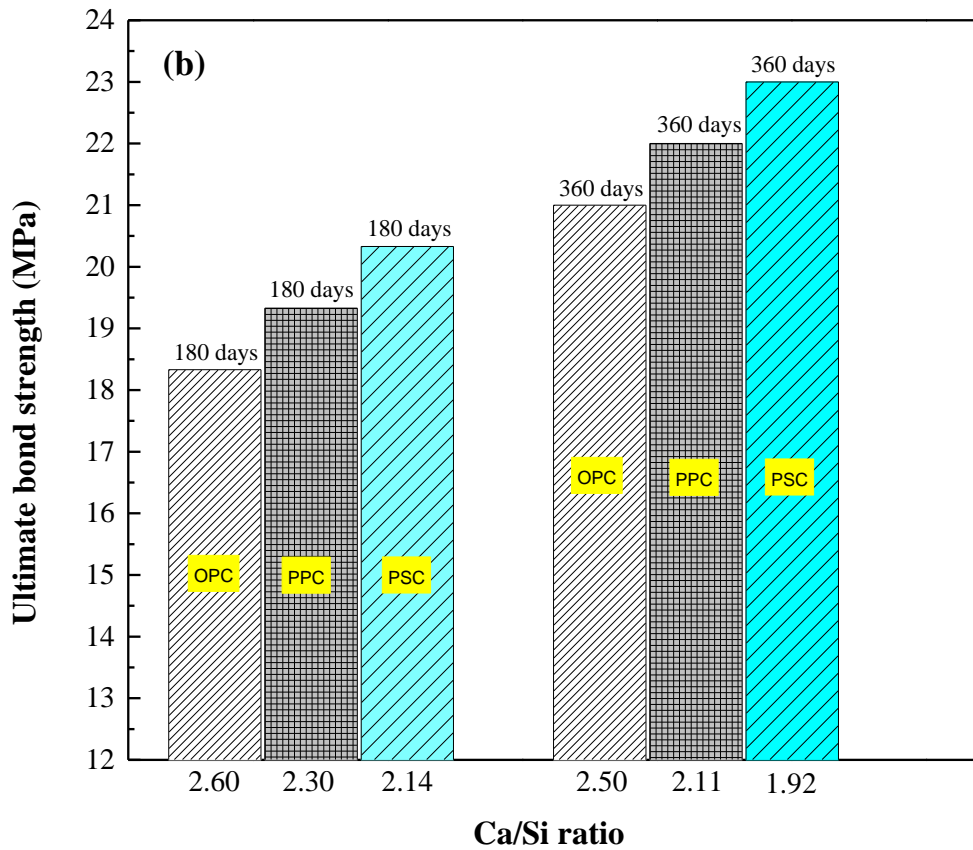
Figure 5.8: Ultimate bond strength and Ca/Si ratio at SCI (0 µm distance) for 180 and 360-days of water curing

The reduction of the Ca/Si ratio can be attributed to the conversion of calcium hydroxide to the final products of hydration (Zayed, 1991; Turk, Karatas and Ulucan, 2010) or to a possibility that unhydrated cement particles react to curing and convert to hydration products (Horne, Richardson and Brydson, 2007). With respect to the development of compressive strength for different types of concrete, it can be noted that OPC attained the highest value at 28-days as well as 90-days curing periods, which can be attributed to the macro-level properties of concrete. On the other hand, the ultimate bond strength for OPC at 28-days of curing was higher than PPC and PSC. With passage of curing time, at 90, 180 and 360-days of curing, PPC and PSC surpassed OPC, and PSC attained the

highest value of ultimate bond strength. This can be attributed to the micro-level property for concrete, where the ultimate bond strength is directly influenced by the Ca/Si ratio at SCI, however, compressive strength, being a macro-level property, does not get very influenced by the Ca/Si ratio.

5.9 THE RELATION BETWEEN Ca/Si RATIO AND NANO-MECHANICAL PROPERTIES OF STEEL-CONCRETE INTERFACE

For few samples, nano-indentation study was carried out to measure the nanomechanical properties such as E-elastic modulus and H-hardness around SCI. OPC 28-day cured samples were chosen for nanomechanical analysis.

Figure 5.9 shows the variation in H-hardness and Figure 5.10 shows E-elastic modulus with respect to Ca/Si ratio as a function of distance from the steel surface. A progressive increase in hardness values were noticed away from the steel surface towards the bulk concrete, the presence of denser concrete increases the hardness value. Lower H-hardness and E-elastic modulus values at SCI (approximately at '0 μm') can be attributed to porous region formed because of the wall effect (Horne, Richardson and Brydson, 2007; Allison et al., 2012; Xiao et al., 2013). However, a steady increase in both H-hardness and E-elastic modulus values were noticed as moved away from the steel surface towards the bulk concrete. The presence of denser concrete away from the interface increases both H-hardness and E-elastic modulus values. It is to be noted that average H-hardness and E-elastic modulus values at SCI ('0 μm' distance from steel surface) were 0.8 GPa and 30 GPa, respectively.

The value of Ca/Si ratio was maximum (2.887) near the steel surface, which signifies the presence of calcium hydroxide. The Ca/Si ratio gradually reduces as moved away from the steel surface towards the bulk concrete. It may be interpreted that, as Ca/Si ratio decreases, both H-hardness and E-elastic modulus values increases at SCI. However, higher value of Ca/Si ratio at SCI signifies the presence of calcium hydroxide (Bentz, Stutzman and Garboczi, 1992; Isu, Ishida and Mitsuda, 1995; Escalante-Garcia, Mendoza

and Sharp, 1999; Zhang *et al.*, 2017), and the mean E-elastic modulus values for calcium hydroxide was reported in the range of 35 - 40 GPa (Wang *et al.*, 2009; Allison *et al.*, 2012; Zacharda, Štemberk and Němeček, 2018). In the present case, the average E-elastic modulus value at SCI ('0 µm' distance from the steel surface) was measured to be 30 GPa. Besides the high concentration of calcium hydroxide at the interface, reduction in values of E-elastic modulus and H-hardness was attributed to the porous nature of SCI (Horne, Richardson and Brydson, 2007; Zhao *et al.*, 2016).
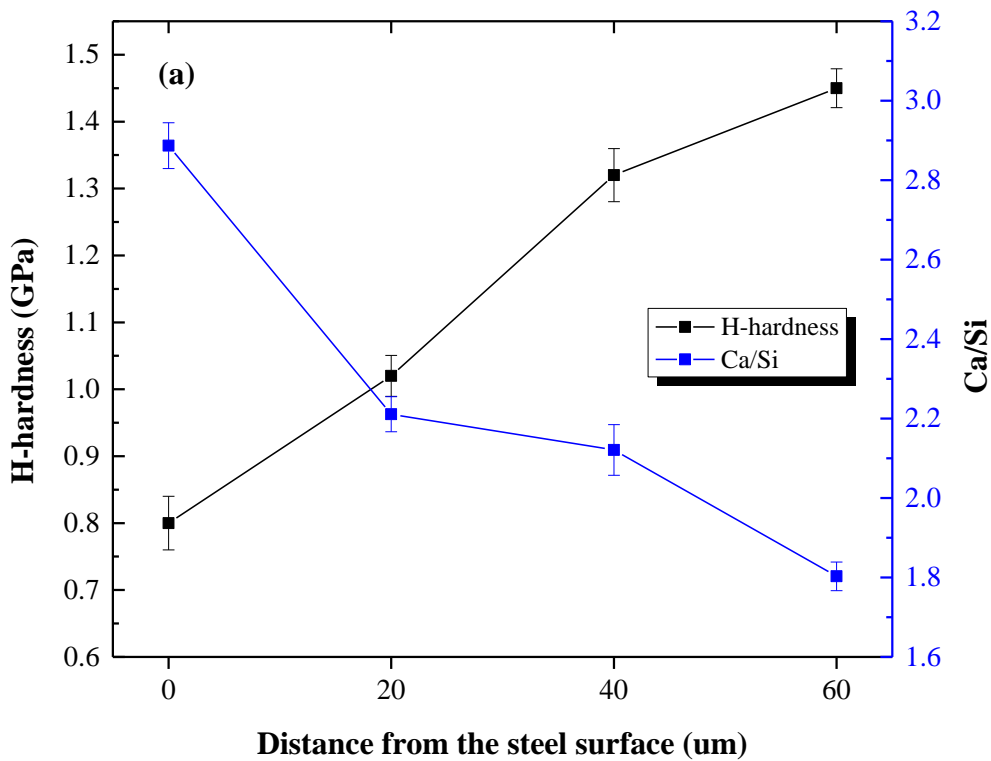
Figure 5.9: Variation in H-hardness with respect to Ca/Si ratio as a function of distance from the steel surface
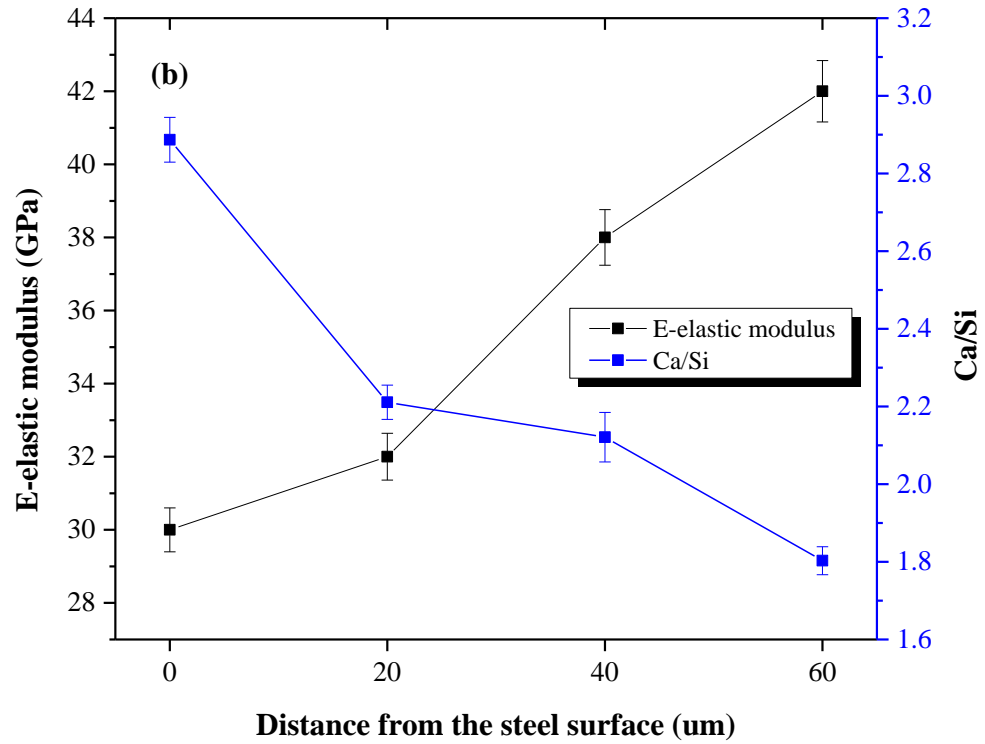
Figure 5.10: Variation in E-elastic modulus with respect to Ca/Si ratio as a function of distance from the steel surface

CHAPTER – 6

EFFECT OF MARINE ENVIRONMENT ON ULTIMATE BOND STRENGTH AND ENGINEERING PROPERTIES OF STEEL-CONCRETE INTERFACE

6.1 GENERAL

In this section, the effect corrosion behavior on ultimate bond strength of OPC, PPC and PSC concretes is examined in simulated marine environment (3.5 wt.% NaCl) for the period up to 720-days. The microstructure study of SCI was carried out to understand the corrosion effect on PZT and the corrosion product layer thickness was measured by image analysis of back scattered electron (BSE) images. Also, the service life prediction of corroded reinforced concrete samples was carried out using measured values of PZT.

6.2 EFFECT OF CORROSION ON ULTIMATE BOND STRENGTH OF OPC, PPC AND PSC CONCRETE MIXES AFTER EXPOSURE TO MARINE ENVIRONMENT

Figure 6.1 shows a typical linear polarization resistance plots for OPC, PPC and PSC concretes after 90-days exposure to simulated marine environment (3.5 wt.% NaCl). These corrosion plots clearly show that the active-passive transition of steel for the different types of concretes. Corrosion kinetics parameters such corrosion current density and corrosion rate were calculated using Tafel extrapolation methods for different exposure period. Figure 6.2 and 6.3 show the corrosion current density and corrosion rate with respect to exposure period for OPC, PPC and PSC concretes, respectively. It is found that corrosion current density and corrosion rate increases for all three types concretes as the exposure period increased. It is noticed that PSC and PPC concrete showed a quite lower corrosion rate as compared to OPC concrete. The corrosion rate for

720-days of exposure are observed about 0.714 mmpy, 0.502 mmpy and 0.431 mmpy for OPC, PPC and PSC concretes, respectively. There is an increase of 14.2 %, 10.9 % and 8.36 % in corrosion rate of OPC, PPC and PSC concretes at 720-days of exposure when compared to control concrete. The PSC concrete showed more resistance to marine environment when compared to PPC and OPC. This can be attributed to the fineness of PSC cement and faster pozzolanic reactions which produces useful secondary C-S-H gel which is responsible for dense microstructure (Das, Singh and Pandey, 2011). Also, the PSC concrete showed comparatively lower porous zone thickness when compared to PPC and OPC concrete before exposing the samples to marine environment (i.e., after 90-day curing). The lower porous zone thickness and reduced Ca/Si ratio signifies denser microstructure of SCI, which might be the reason for lower corrosion rates of PSC concrete.
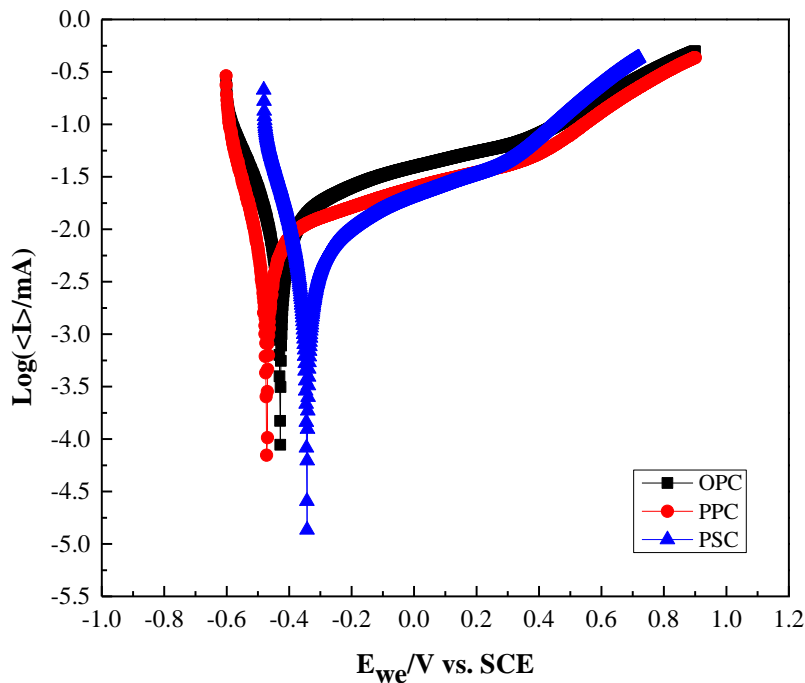
Figure 6.1: A typical linear polarization resistance plot for OPC, PPC and PSC concrete after 90-days exposure to marine environment
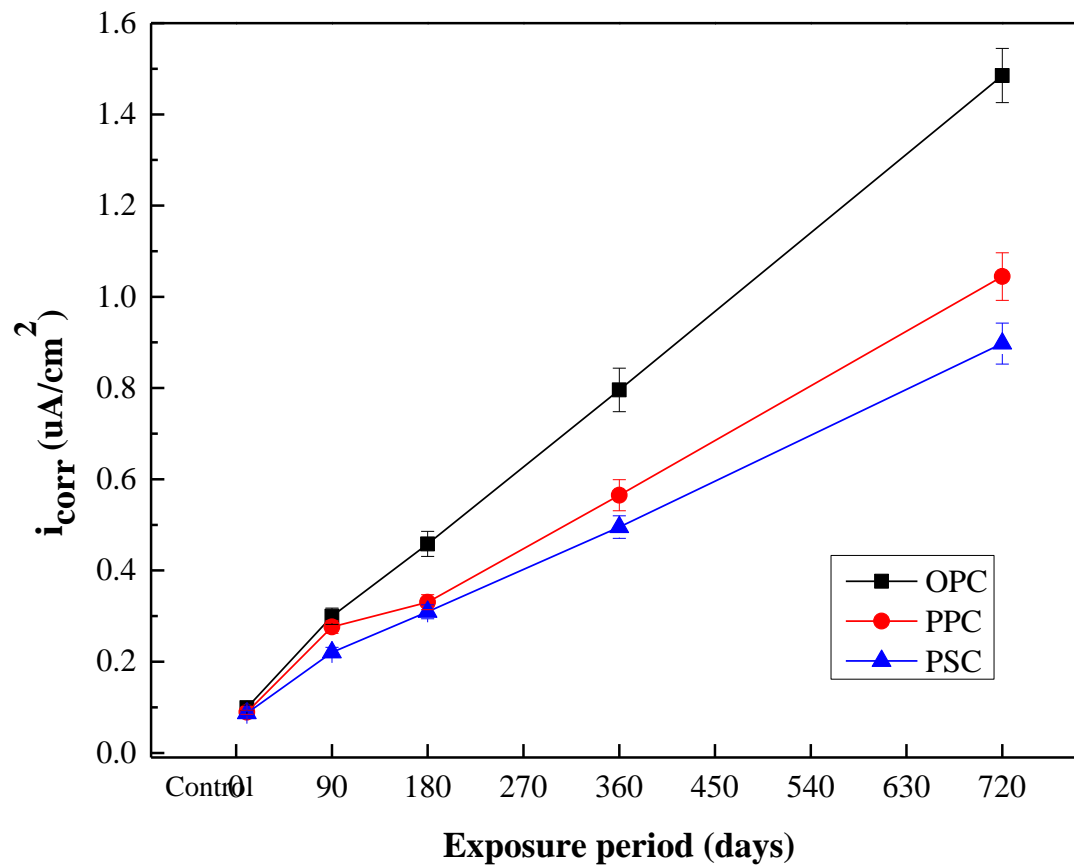
Figure 6.2: Corrosion current density for OPC, PPC and PSC concrete exposed to marine environment for different exposure periods

The relationship between the corrosion rate (CR) and exposure period (t) in marine environment of OPC, PPC, and PSC concretes samples was analyzed by regression analysis. As the exposure period increases, the corrosion rate also increases significantly for OPC, PPC, and PSC concrete mixes. It can be noted from the regression analysis that there is a linear trend that fits very well with R^2 values of 0.999, 0.9928 and 0.9982 for OPC, PPC, and PSC concrete mixes, respectively. The linear equations obtained by regression analysis for OPC, PPC, and PSC concretes are given by equations (4), (5), and (6), respectively. These relations are developed for M40 grade concrete with water to

cement ratio of 0.40. For more details about the mix proportion of concrete refer Table 3.6 (chapter 3).

$$CR\,(OPC) = \mathbf{0.0009}\,(t) + \mathbf{0.0503} \tag{4}$$

$$CR\,(PPC) = \mathbf{0.0006}\,(t) + \mathbf{0.052} \tag{5}$$

$$CR\,(PSC) = \mathbf{0.0005}\,(t) + \mathbf{0.0499} \tag{6}$$
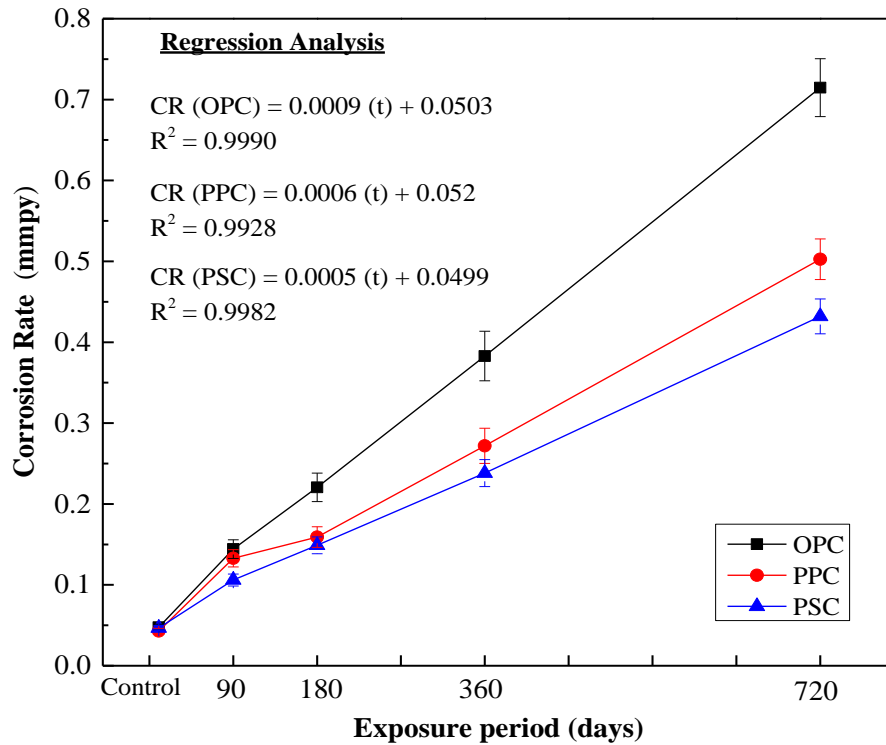
Figure 6.3: Corrosion rate of OPC, PPC and PSC concrete exposed to marine environment for 90, 180, 360 and 720-days (CR – Corrosion rate)

Figure 6.4 show the rate of corrosion and ultimate bond strength of OPC, PPC and PSC concretes exposed to marine environment for different durations. It is observed that up to 360 days of marine environment exposure, the ultimate bond strength of all three types of concretes increased when the corrosion rate increased. It is noticed that the ultimate bond strength significantly reduced for OPC and PPC concretes at 720-days of exposure. At 720-days exposure, rate of corrosion was higher and that might have produced cracks at

SCI which might be the reason for reduced ultimate bond strength for OPC and PPC concrete ((Fang *et al.*, 2004, 2006). However, the ultimate bond strength of PSC concrete did not show similar trend as of OPC and PPC concretes for 720-days of exposure. A trivial improvement in ultimate bond strength even after 720-days of exposure for the PSC concrete was observed. It could be due to continued hydration process and formation of corrosion products at SCI was inadequate to induce the corrosion cracks and hence increased the friction during the pullout test, which resulted in increased ultimate bond strength of PSC concrete.
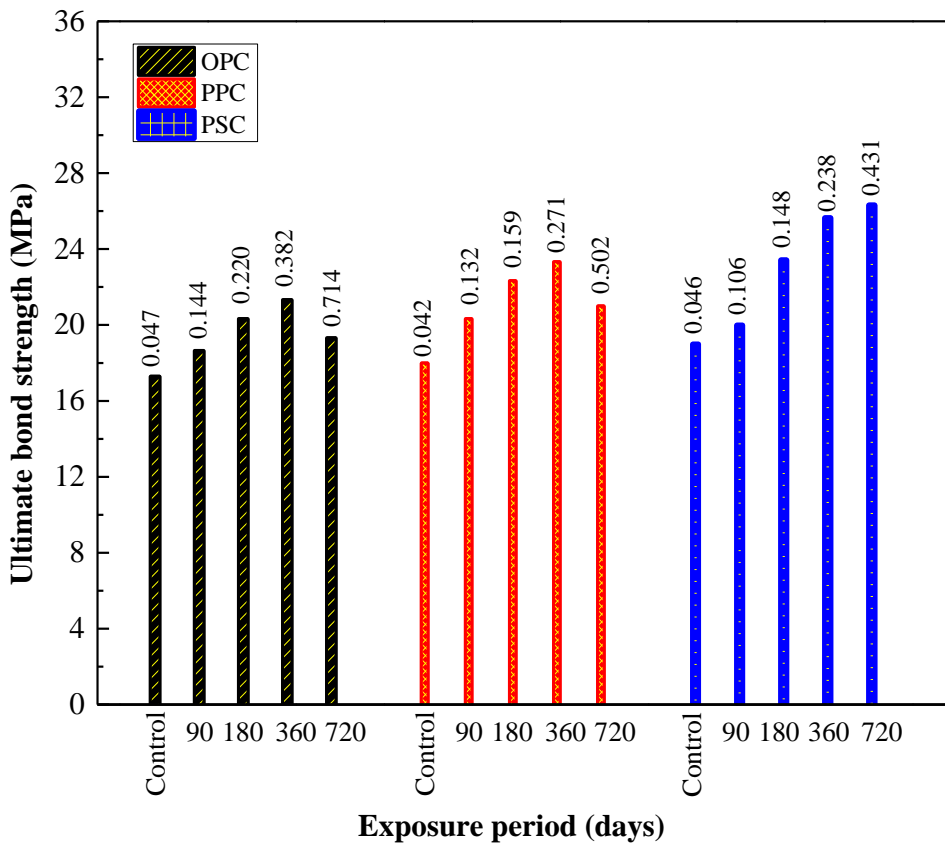
Figure 6.4: Ultimate bond strength variation with respect to exposure period and rate of corrosion (the values shown above the bars are corrosion rates expressed in mmpy)

6.3 EFFECT OF MARINE ENVIRONMENT ON THE PROPERTIES OF STEEL-CONCRETE INTERFACE

Microstructure of SCI influence corrosion intiation of steel and directly govern corrosion-induced cracking of RC structures. The microstructure study of SCI was carried out after exposing the RC samples to marine environment. The extent of formation of corrosion products at SCI was alanyzed. It is to be noted that cross-sections in the samples were randomly selected for SEM study of corrosion products distribution. Figure 6.5 shows the representative SEM image and EDS elemental analysis map of PSC concrete exposed to marine environment for 360-days. In the concrete part of SCI, a sharp peak of 'Fe' and small peaks of 'Ca', 'Si' and other elements of hydration products can be observed in EDS elemental map. This signifies that a small amount of corrosion products started to accumulate at the porous region of SCI. Which might be one of the contributing factor for increased ultimate bond strength of PSC concrete after 360-days of marine environment exposure. A small and continious crack were observed near SCI, which could be the artifact of slice cutting process during the sample preparation technique.
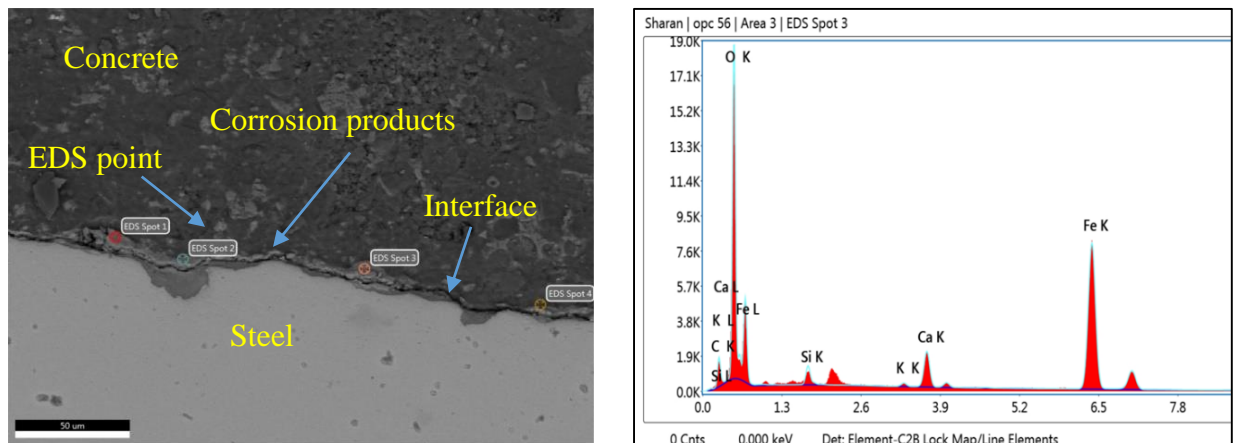
Figure 6.5: SEM image and EDS elemental map of concrete exposed to marine environment for 180 days

Figure 6.6, 6.7 and 6.8 show the SEM images of OPC, PPC and PSC concretes, respectively which are exposed to marine environment for different periods. The distribution of corrosion products is not unifirm at SCI due to non uniform porous zone thickness. However, the service life prediction models assumes a uniform distribution of corrosion products (Liu, 1996b; Hime, Backus and Li, 1999; Bhargava *et al.*, 2005; Chen and Mahadevan, 2008).

(a) 90-days

(b) 180-days

(c) 360-days

(d) 720-days
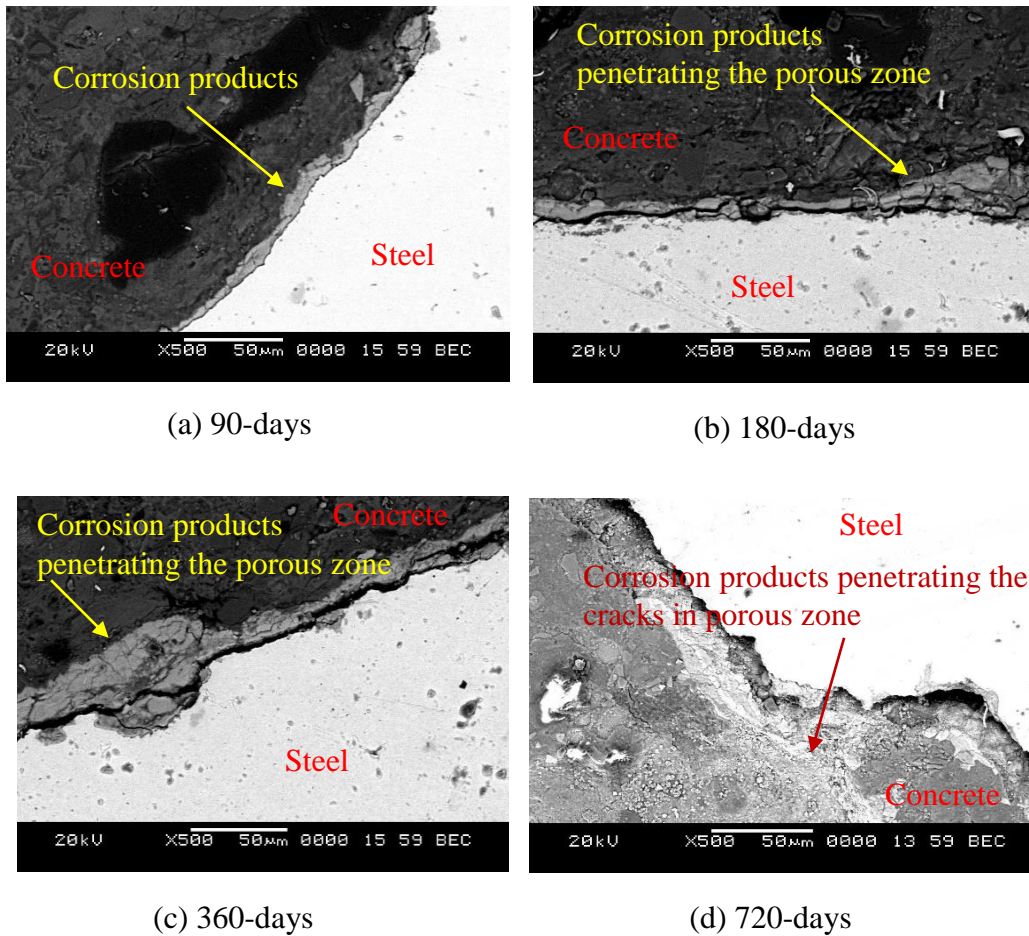
Figure 6.6: SEM images of OPC concrete exposed to marine environment for different exposure periods

For OPC concrete, 90-days of marine environment exposure produced a small amount of corrosion products (shown in Fig 6.6 a) which might have increased the friction during pullout test and resulted in enhanced ultimate bond strength. At 180-days of exposure, the corrosion products started penetrating the porous zone without exerting the expansive pressure. At 360 and 720-days of exposure, the corrosion products started exerting the expansive pressure, which resulted in formation of cracks in the porous zone (refer Figure 6.6 d).

(a) 90-days   (b) 180-days

(c) 360-days   (d) 720-days
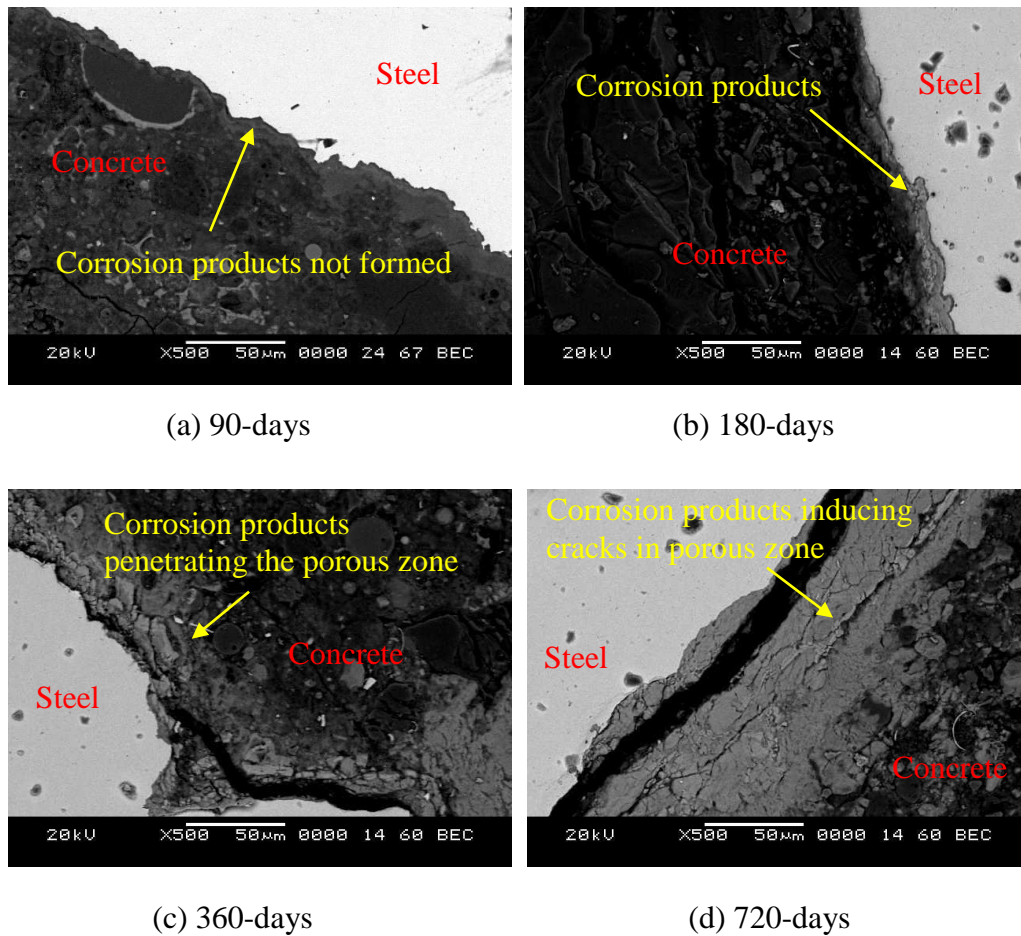
Figure 6.7: SEM images of PPC concrete exposed to marine environment for different exposure periods

SEM image shown in Figure 6.7 (a), for the PPC concrte, it did not showed a noticeable corrosion products at SCI for 90-days. But, when exposted to 180-days, the corrosion products started penetrating the porous zone. At 360-days of exposure, corrosion products started exerting the expansive pressure, which resulted in formation of cracks in the porous zone. Severe cracks were develpoed aftre the exposure of 720-days. It may due to the very high expansive pressure got exerted by the excess corrsion products which directly influneced the ultimate bond strength.

(a) 90-days   (b) 180-days

(c) 360-days   (d) 720-days
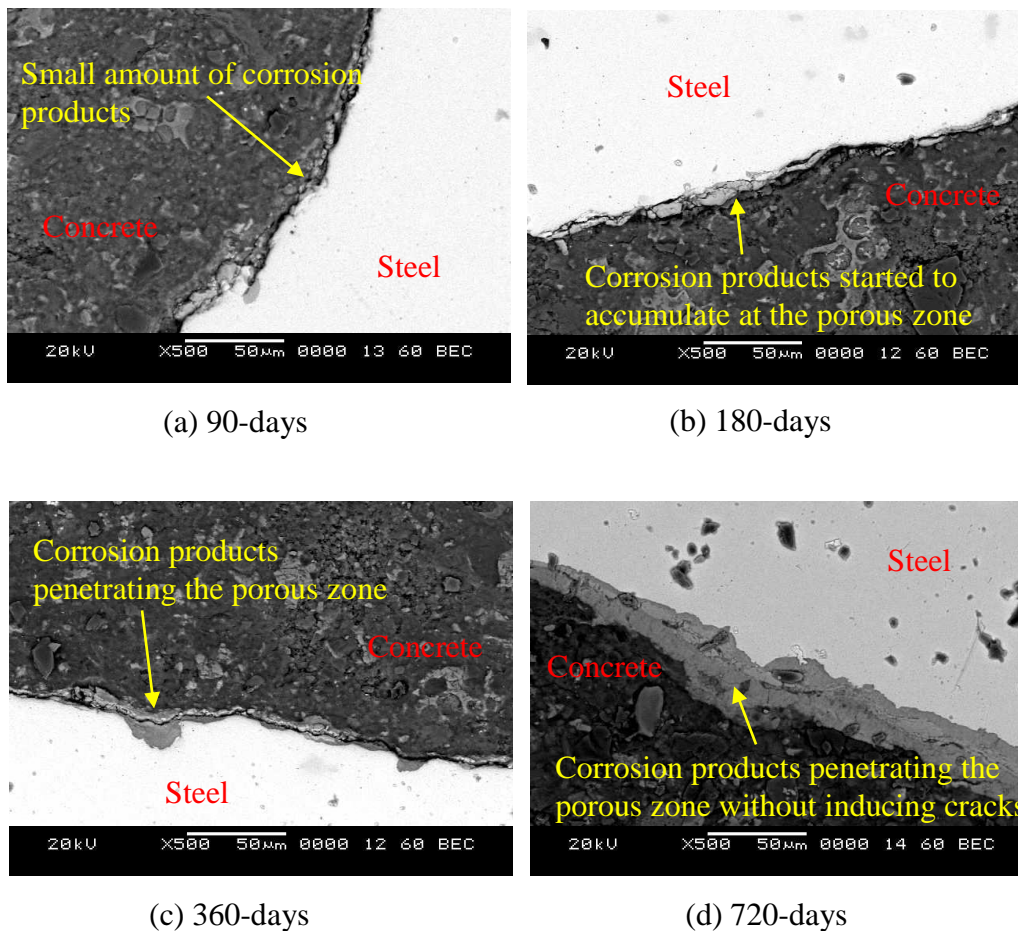
Figure 6.8: SEM images of PSC concrete exposed to marine environment for different exposure periods

For PSC concrete, 90-days of marine environment exposure produced small amount of corrosion products is shown in figure 6.8 (a). These corrosion products along with continuous hydration process resulted in enhanced ultimate bond strength. At 180-days of exposure, the corrosion products started to accumulate at SCI without exerting the expansive pressure on concrete. At 360-days of exposure, the corrosion products started penetrating the PZT. However, the amount of corrosion products are less which did not exert any expansive pressure. The corrosion products formed at SCI might have increased the friction during pullout test and resulted in enhanced ultimate bond strength at 360-days of exposure. At 720-days of exposure, the corrosion products started penetrating the porous zone without exerting any expansive pressure. Hence, at the end of 720-days of exposure also the ultimate bond strength increased for PSC concrete.

6.3.1 Distribution of corrosion products at SCI

(a)　　　　　　　　　　　　　　　　　　　(b)
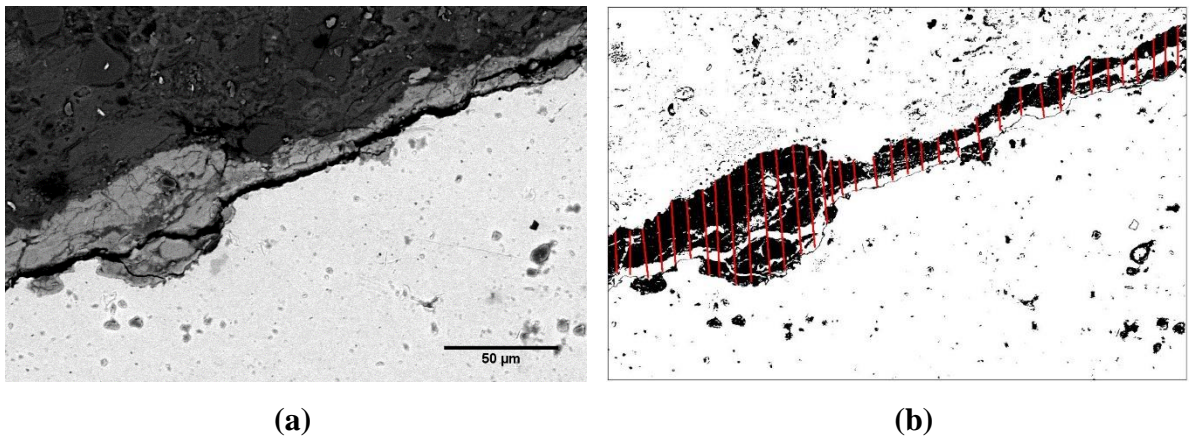
Figure 6.9: (a) BSE image of OPC concrete at 360-days of exposure to marine environment and (b) BSE image after thresholding and measuring the thickness of corrosion product layer

It is observed that using the SEM images, porous zone at SCI and corrosion products distribution were non-uniform. Limited experimental data on distribution of corrosion products at SCI have been reported, which hinders the improvement of accuracy of the

predictive models (Chun-Qing, Melchers and Jian-Jun, 2006; Chen, Baji and Li, 2018). Figure 6.9 (a) shows the representative BSE image of OPC concrete which was exposed to marine environment for 360-days (1 Year). After thresholding the BSE image which is shown in figure 6.9 b, thickness of corrosion product layer was measured using ImageJ software (Chen *et al.*, 2018). Same method of thresholding was followed for PPC and PSC concretes for measuring the thickness of corrosion product layer for all the exposure periods. Table 6.1, 6.2 and 6.3 show the thickness of corrosion product layers at twelve spots (shown in Figure 3.9) for OPC, PPC and PSC concretes, respectively for different exposure periods (90, 180, 360 and 720-days) to marine environment.

Table 6.1: Thickness of corrosion product layers at twelve spots for OPC, PPC and PSC concretes for 90-days of exposure to marine environment

| Location | Thickness of corrosion product layers after 90-days of exposure to marine environment | | | | | |
| | OPC | | PPC | | PSC | |
	Mean value (µm)	Standard deviation (µm)	Mean value (µm)	Standard deviation (µm)	Mean value (µm)	Standard deviation (µm)
Spot 1	6.55	4.66	8.12	1.83	8.12	1.53
Spot 2	8.01	2.54	7.28	1.94	10.06	1.61
Spot 3	13.64	4.11	10.21	0.90	12.22	0.75
Spot 4	14.99	3.08	12.32	5.26	14.2	4.38
Spot 5	7.21	3.60	10.58	0.97	9.34	0.81
Spot 6	9.33	4.45	12.35	3.48	10.7	2.89
Spot 7	8.48	3.04	5.97	4.23	15.36	3.52
Spot 8	6.21	2.40	8.55	2.53	7.1	2.10
Spot 9	4.61	0.09	5.79	0.19	6.25	0.16
Spot 10	4.11	3.49	10.41	1.00	11.1	0.83
Spot 11	7.31	2.22	5.96	1.49	15.25	1.24
Spot 12	9.22	2.70	8.34	1.72	11.39	1.43

Table 6.2: Thickness of corrosion product layers at twelve spots for OPC, PPC and PSC concretes for 180-days of exposure to marine environment

Location	Thickness of corrosion product layers after 180-days of exposure to marine environment					
	OPC		PPC		PSC	
	Mean value (μm)	Standard deviation (μm)	Mean value (μm)	Standard deviation (μm)	Mean value (μm)	Standard deviation (μm)
Spot 1	11.11	3.73	10.22	2.01	10.32	1.84
Spot 2	10.33	2.03	11.77	2.13	12.63	1.93
Spot 3	16.37	3.29	11.74	0.99	14.33	0.90
Spot 4	17.99	2.46	14.17	5.79	16.18	5.26
Spot 5	18.33	2.88	16.17	1.07	12.54	0.97
Spot 6	20.21	3.56	14.2	3.83	11.22	3.47
Spot 7	15.18	2.43	8.87	4.65	12.2	4.22
Spot 8	9.33	1.92	10.53	2.78	7.95	2.52
Spot 9	7.52	0.07	7.36	0.21	8.4	0.19
Spot 10	10.66	2.79	11.97	1.10	13.95	1.00
Spot 11	10.11	1.78	6.85	1.64	17.08	1.49
Spot 12	14.96	2.16	9.59	1.89	12.76	1.72

Table 6.3: Thickness of corrosion product layers at twelve spots for OPC, PPC and PSC concretes for 360-days of exposure to marine environment

Location	Thickness of corrosion product layers after 360-days of exposure to marine environment					
	OPC		PPC		PSC	
	Mean value (μm)	Standard deviation (μm)	Mean value (μm)	Standard deviation (μm)	Mean value (μm)	Standard deviation (μm)
Spot 1	16.22	4.10	15.25	2.30	14.11	3.73
Spot 2	20.11	2.23	14.28	2.45	13.12	2.03
Spot 3	21.38	3.62	16.44	3.60	16.93	3.29
Spot 4	23.69	2.71	19.84	1.47	18.23	2.46
Spot 5	25.93	3.17	22.64	2.14	16.32	2.88
Spot 6	26.53	3.92	19.88	6.33	12.69	3.56
Spot 7	21.68	2.67	10.62	3.25	15.86	2.43
Spot 8	11.55	2.11	13.54	1.01	10.34	1.92
Spot 9	22.16	0.08	8.12	1.14	11.02	1.24
Spot 10	17.94	3.07	16.76	3.56	15.34	2.79
Spot 11	14.44	1.96	9.59	2.58	22.23	1.78
Spot 12	22.64	2.38	13.43	1.17	16.59	2.16

Table 6.4: Thickness of corrosion product layers at twelve spots for OPC, PPC and PSC concretes for 720-days of exposure to marine environment

Location	Thickness of corrosion product layers after 720-days of exposure to marine environment					
	OPC		PPC		PSC	
	Mean value (μm)	Standard deviation (μm)	Mean value (μm)	Standard deviation (μm)	Mean value (μm)	Standard deviation (μm)
Spot 1	18.01	2.53	18.31	2.78	20.21	3.28
Spot 2	23.22	2.70	16.60	2.96	18.17	1.78
Spot 3	25.06	3.96	20.55	4.36	19.15	2.90
Spot 4	26.83	1.62	24.81	1.78	20.56	2.17
Spot 5	28.72	2.35	28.32	2.59	16.77	2.54
Spot 6	28.64	6.96	24.85	4.66	15.95	3.14
Spot 7	26.02	3.58	15.03	3.93	16.25	2.14
Spot 8	15.22	1.11	18.18	1.22	10.59	1.69
Spot 9	24.59	1.25	14.63	1.38	15.19	1.06
Spot 10	19.53	3.92	20.95	4.31	16.59	2.46
Spot 11	17.93	2.84	11.99	3.12	25.75	1.57
Spot 12	26.77	1.29	16.79	1.42	17.23	1.90
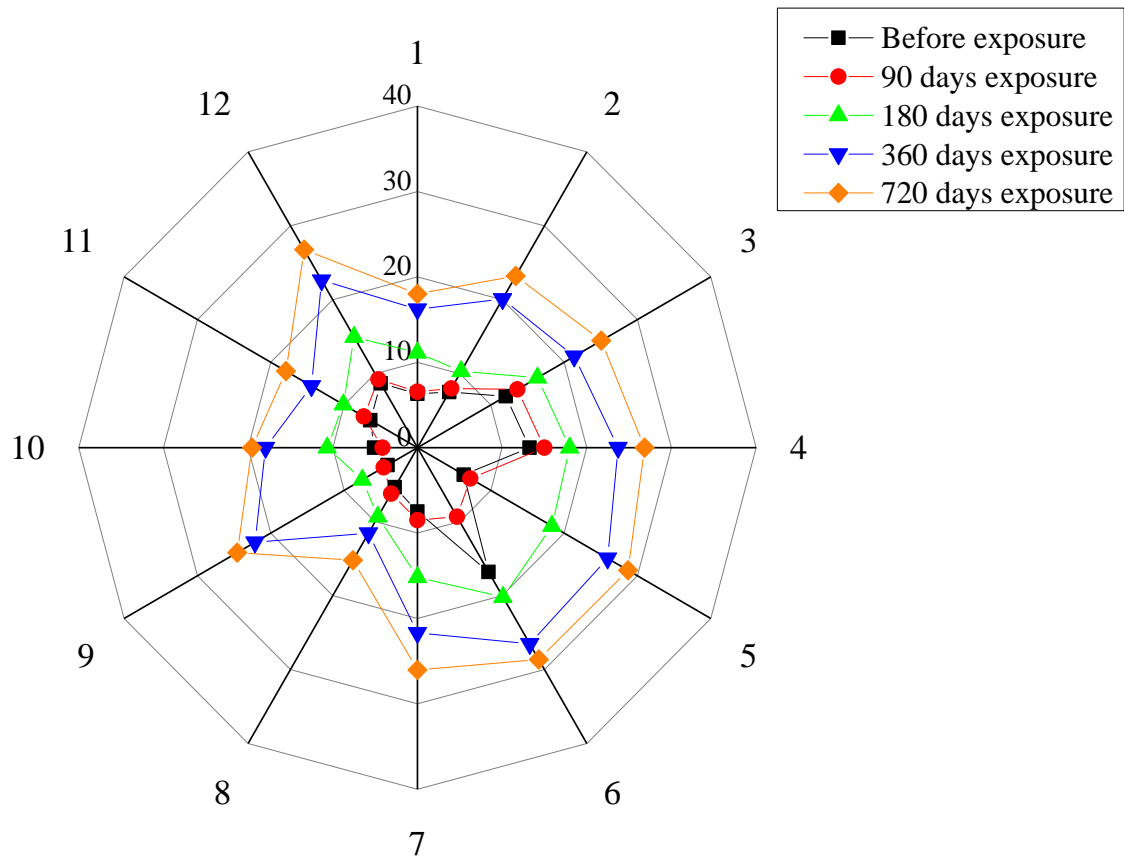
Figure 6.10: Thickness of corrosion product layers (μm) measured at twelve spots around steel bar of OPC concrete at 90, 180, 360 and 720-days of exposure to marine environment.
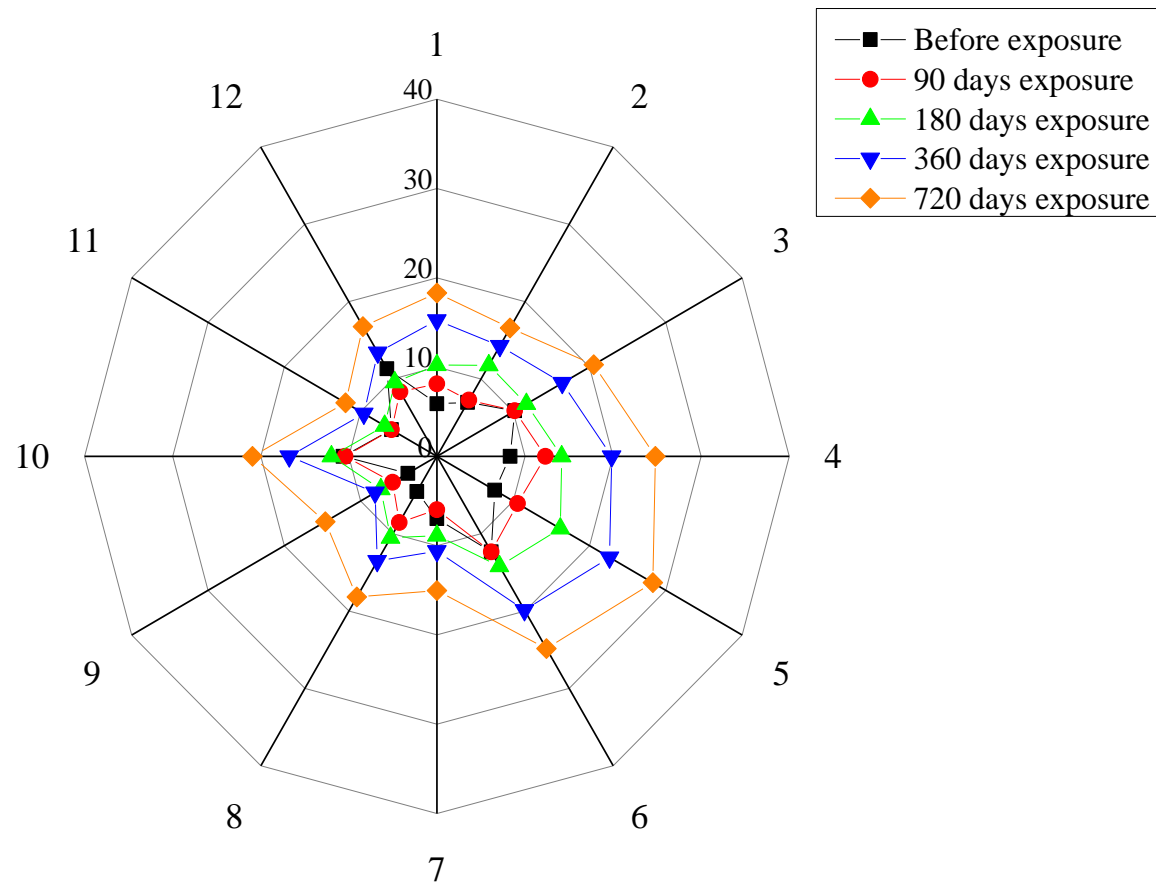
Figure 6.11: Thickness of corrosion product layers (μm) measured at twelve spots around steel bar of PPC concrete at 90, 180, 360 and 720-days of exposure to marine environment.

143
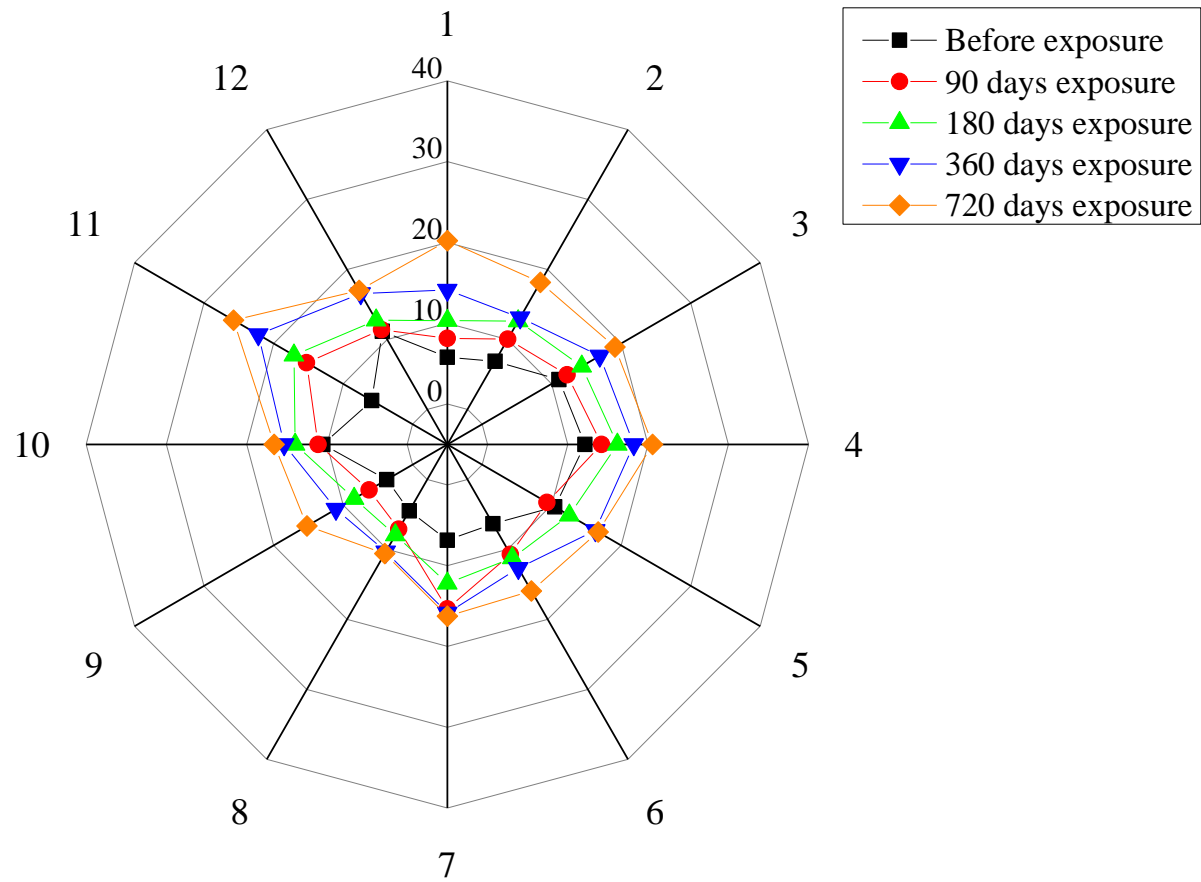
Figure 6.12: Thickness of corrosion product layers (μm) measured at twelve spots around steel bar of PSC concrete at 90, 180, 360 and 720-days of exposure to marine environment.

Figure 6.10, 6.11 and 6.12 shows the mean thickness of corrosion products layer for OPC, PPC and PSC concrete mixes, respectively, after exposing the RC samples to marine environment for 90, 180, 360 and 720-days. After corrosion initiation, corrosion products start occupying the space in PZT. The reduction in volume of reinforcing steel after corrosion results in the rust formation, which might increase the thickness of corrosion product layer and overall PZT. Only a few spots where selected where an enriched corrosion products penetrated the PZT around SCI and analyzed for measuring the thickness of corrosion product layer.

It can be observed that all the concrete mixes show an increase in thickness of corrosion product layer as the exposure period increased from 90-days to 720-days. However, the distribution of corrosion product was found to be non uniform, which is due to the inhomgenious distribution of PZT. At few spots the corrosion products were well within the PZT and at few spots the PZT was fully filled by corrosion products which can be seen SEM imges of Figure 6.6 - 6.8. It is observed from Figure 6.10 – 6.12 that there are trivial differences in mean thickness of corrosion products layer for OPC, PPC and PSC mixes till 180-days of exposure period. However, thickness of corrosion products layer was slightly minimal for PSC concrete mix when compared to PPC and OPC mixes at 360-days and 720-days of exposure to marine environment. The minimal rate of corrosion for PSC concrete resulted in lower thickness of corrosion products layer.

6.4 SERVICE LIFE PREDICTION THROUGH MEASURED VALUES OF POROUS ZONE THICKNESS

The service life of samples exposed to marine environment was predicted using mathematical model proposed by El Maaddawy and Soudki (2007). The model considers the PZT as one of the important parameter while predicting the time from corrosion initiation to corrosion cracking. The input parameters for the mathematical models were diameter of the steel reinforcing bar (10 mm), porous zone thickness (μm), poisson's ratio of concrete (0.15), corrosion current density (μA/cm^2), characteristic compressive strength of concrete (f_{ck} = 40 MPa), concrete creep coefficient (1.6) and clear cover of the

specimen (15 mm). By considering the above input parameters, the service life (year) from corrosion initiation to corrosion cracking was calculated. The established service life prediction models use a single avearge value of PZT, which assumes the uniform distribution of corrosion products around SCI. However, it is observed that PZT is not uniform around SCI, which is discussed in the chapter 5. Also, the distribution of corrosion products is not uniform and varies from point to point around the steel bar, which is attributed to the non uniformity of PZT. Here, the present study considers, two values of PZT (minimum and maximum) which helps in finding the two extreme time bounds for service life of structures. Also, it is considered an average value of PZT which was assumed by previous researchers for predicting the service life of structures (Liu, 1996a; Weyers, 1998; Wang, Wang and Liu, 2004; Bhargava *et al.*, 2006).

Table 6.5 shows predicted time from corrosion initiation to corrosion cracking (which is referred as 'service life') for different exposure periods considering as minimum, average and maximum values of porous zone thickness and corresponding corrosion current density values. For better understanding, the service life of OPC, PPC and PSC concretes were calculated using minimum, average and maximum values of PZT (before exposure to marine environment) and presented in Figure 6.13. It can be observed that small variation in considering the value of PZT in service life prediction models leads to larger variations in predicted service life of structures.

To comapre service life of OPC, PPC and PSC concretes before and after exposure to the marine environment (from Table 6.5), it is found that PZT and corrosion current density played an imporatnt role. As the corrosion current density increasesd, the filling capabilty of PZT also increased. It can be found that PZT (average) is being filled rapidly for OPC concrete when corrosion current density is higher (Zhao, Wu and Jin, 2013). Similarly, the PPC and PSC concretes corrosion current density values are quite lower than OPC concrete which is resulted in higher service life values.

146
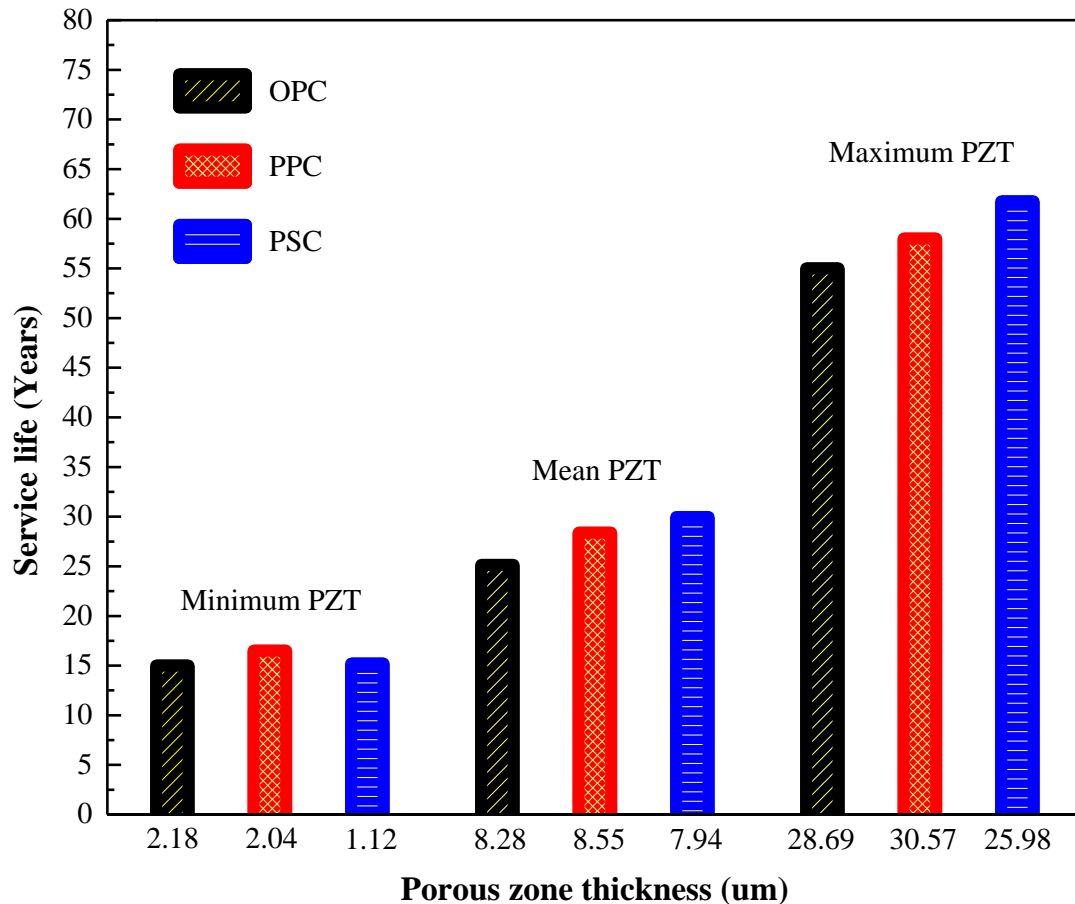
Figure 6.13: Influence of considering the porous zone thickness on the service life of OPC, PPC and PSC concrete

It can also be noted from Table 6.5 that service life of structure increases with increase in the thickness of porous zone. This is mainly due to the available higher free space for corrosion products to occupy within the porous zone before exerting the expansive pressure. In the present case, OPC concrete showed higher PZT which should reflect in higher service life values. However, the obtained results are contradictory as service life of OPC concrete was lesser as compared to PPC and PSC concrete mixes. As the PZT is higher, availability of moisture and oxygen concentration would be more and correspondigly corrosion current density will be higher. The corrosion products will fill

the PZT at a faster rate due to more corrosion rate of steel. For example, the average value of PZT of OPC concrete at 90-days curing (before exposure) is 8.28 μm, as the exposure to marine environment reached to 720-days, corrosion products occupy the PZT and the value reduced to 5.03 μm. The corrosion products occupy the PZT by 39.25 % at the end of 720-days of exposure. At the same time the rate of corrosion current density increased by 14 times for OPC concrete. Similarly, for PPC and PSC concretes the corrosion products occupy the PZT by 35.93 % and 22.53 % at the end of 720-days of exposure and the rate of corrosion current density increased by 10.72 times 9.32 times, respectively. With the increase in exposure period, the rate of filling of PZT by corrosion products was more for OPC concrete as its corrosion current density is more compared to PPC and PSC concrete, which resulted in lesser service life values.

However, in case of PSC and PPC concrete the PZT are lesser compared to OPC concrete along with lower corrosion current denmsity which will delay the filling of PZT. Overall, it can be summerized that the PSC concrete performance is superior over the other concretes (OPC and PPC).

There are two draw backs in the current service life prediction model propsed by El Maaddawy and Soudki, (2007). The first one being the consideration of a constant and uniform PZT around SCI and second one is assumption of a uniform distribution of corrosion products within the PZT. However, in the present study, it is found that PZT is not uniformly distrubuted around SCI. Also, a non uniform distribution of PZT resulted in non uniform distribution of corrosion products around SCI. Considering the uniform PZT and uniform distribution of corrosion products around SCI seems to be over simplification and which may lead to misinterpretation of service life of corroding RC structures. A detailed and reformed service life prediction model needs to be developed by considering the non uniform distribution of porous zone as well as non-uniform distribution of corrosion layer.

Table 6.5: Time from corrosion initiation to corrosion cracking for different exposure periods considering minimum, average and maximum values of porous zone thickness

Type of concrete and exposure details	i_{corr} ($\mu A/cm^2$)	Porous zone thickness (μm)			1*	2*	3*
		Minimum	Average	Maximum			
OPC							
OPC 90 days curing	0.0989	2.18	8.28	28.69	15.10	28.81	58.72
OPC 90 days exposure	0.2996	3.65	7.43	26.32	5.78	9.05	18.1
OPC 180 days exposure	0.4583	3.11	6.98	25.36	3.59	5.76	11.49
OPC 360 days exposure	0.7957	2.35	6.01	22.65	1.91	3.12	6.06
OPC 720 days exposure	1.4852	2.66	5.03	23.74	1.06	1.56	3.37
PPC							
PPC 90 days curing	0.0891	3.44	8.22	26.44	19.06	31.87	61.07
PPC 90 days exposure	0.2761	2.88	8.02	25.68	5.82	10.17	19.26
PPC 180 days exposure	0.3305	3.32	7.64	26.37	5.08	8.31	16.43
PPC 360 days exposure	0.5650	2.88	7.10	23.41	2.84	4.70	8.76
PPC 720 days exposure	1.0444	1.89	6.29	20.64	1.38	2.42	4.31

Type of concrete and	i_{corr} (µA/cm²)	Porous zone thickness (µm)			1*	2*	
PSC							
PSC 90 days curing	0.0869	4.55	7.94	26.22	19.39	32.15	62.20
PSC 90 days exposure	0.2203	3.54	7.51	22.36	7.78	12.36	21.68
PSC 180 days exposure	0.3094	3.68	7.30	24.34	5.62	8.69	16.48
PSC 360 days exposure	0.4950	3.44	6.97	20.55	3.43	5.33	9.06
PSC 720 days exposure	0.8975	2.22	6.48	21.88	1.67	2.85	5.24

1* - Service life prediction considering minimum value of porous zone thickness (Years), 2*- Service life prediction considering average value of porous zone thickness (Years), 3* - Service life prediction considering maximum value of porous zone thickness (Years).

CHAPTER – 7

CONCLUSIONS AND SCOPE FOR FUTURE WORK

7.1 CONCLUSIONS

In the present research work, parameters which affect the engineering properties of steel-concrete interface, such as porous zone thickness, nanomechanical properties and hydration products were studied. The results based on experimental investigation allow us to draw the following conclusions.

- The properties of steel-concrete interface especially the porous zone thickness and nanomechanical properties (hardness and elastic modulus) are sensitive to the cutting tool used during sample preparation of reinforced concrete samples for SEM analysis. For cutting the reinforced concrete samples, a low-speed precision diamond saw cutter with speed of 100 – 200 rpm is recommended.

- The properties of steel-concrete interface were found to be influenced by the water curing period. A reduction in mean porous zone thickness was found in all three kinds of concretes (OPC, PPC and PSC). The PSC concrete showed a significant reduction in mean porous zone thickness at SCI when compared with OPC and PPC concrete till 360-days of water curing.

- The preferential formation of calcium hydroxide was confirmed through SEM images as well as EDS analysis around steel-concrete interface.

- As the curing period increased, it was found that there is a gradual reduction in the Ca/Si ratio, which signifies the gradual reduction in calcium hydroxide from the steel surface toward the bulk concrete.

- A gradual increase in ultimate bond strength is observed up to 360-days of water curing. The reduction in mean porous zone thickness around SCI can be considered as one of the many influencing factors that resulted in increased ultimate bond strength till 360-days of water curing.

- The long-term curing (up to 360-days), especially for PPC and PSC concretes, helped in the advancement of pozzolanic reaction, and in this process, the calcium hydroxide content reduced (Ca/Si ratio reduced) at steel-concrete interface, which is responsible for increased ultimate bond strength as compared with OPC concrete.

- Exposure of reinforced concrete samples to marine environment increased the ultimate bond strength for up to 360-days. Microstructure study revealed that corrosion products penetrated the porous zone between steel and concrete which increased the friction during pull out test and resulted in increased ultimate bond strength.

- The longer exposure to marine environment for duration of 720-days reduced the ultimate bond strength. The microstructure study revealed that corrosion products completely filled the porous zone and started exerting the expansive pressure which resulted in generation of severe cracks at steel-concrete interface.

- It is found that non uniform distribution of porous zone thickness resulted in non uniform distribution of corrosion products at steel-concrete interface.

- The porous zone thickness values around the steel-concrete interface and corrosion current density plays an important role while predicting the service life of structures exposed to marine environment.

- The PSC concrete was found to have lesser corrosion current density values when compared to PPC and OPC concretes which resulted in greater time for corrosion initiation to corrosion cracking (greater service life).

152

- Overall, PSC concrete performed superior in marine environment when compared to PPC and OPC concretes. From the present study, it is recommended to use PSC concrete followed by PPC and OPC concrete for marine environment.

7.2 SCOPE FOR FUTURE STUDY

- From the experimental analysis it was found that engineering properties of steel-concrete interface, such as porous zone thickness and hydration products will change over time. The long-term analysis of properties of steel-concrete interface needs systematic analysis.

- It was found that the properties of steel-concrete interface are sensitive to sample preparation methods. There is a huge scope to look out for a method, where there is least damage to steel-concrete interface.

- Non-uniform distribution of porous zone thickness at steel-concrete interface and its influence on formation of corrosion products needs further research.

- A detailed and reformed service life prediction model needs to be developed by considering the non uniform distribution of porous zone as well as non-uniform distribution of corrosion products.

References

516, I. (1959) 'Indian standard methods of tests for strength of concrete', *Bureau of Indian Standards*.

Ahmad, S. (2003) 'Reinforcement corrosion in concrete structures, its monitoring and service life prediction—a review', *Cement and concrete composites*. Elsevier, 25(4–5), pp. 459–471.

Allison, P. G. *et al.* (2012) 'Nanomechanical and chemical characterization of the interface between concrete, glass–ceramic bonding enamel and reinforcing steel', *Construction and Building Materials*. Elsevier, 37, pp. 638–644.

Angst, U. M. *et al.* (2017) 'The steel–concrete interface', *Materials and Structures*. Springer, 50(2), p. 143.

Ann, K. Y. and Song, H.-W. (2007) 'Chloride threshold level for corrosion of steel in concrete', *Corrosion Science*. Elsevier, 49(11), pp. 4113–4133.

Arel, H. Ş. and Yazıcı, Ş. (2012) 'Concrete–reinforcement bond in different concrete classes', *Construction and building materials*. Elsevier, 36, pp. 78–83.

Basheer, L., Basheer, P. A. M. and Long, A. E. (2005) 'Influence of coarse aggregate on the permeation, durability and the microstructure characteristics of ordinary Portland cement concrete', *Construction and Building Materials*. Elsevier, 19(9), pp. 682–690.

Bäumel, A. (1959) 'Die Auswirkung von Betonzusatzmitteln auf das Korrosionsverhalten von Stahl in Beton', *Zement-Kalk-Gips*, 7, pp. 294–305.

Bazant, Z. P. (1979) 'Physical model for steel corrosion in concrete sea structures--application', *Journal of the structural division*, 105(ASCE 14652 Proceeding).

Bentz, D. P., Stutzman, P. E. and Garboczi, E. J. (1992) 'Experimental and simulation studies of the interfacial zone in concrete', *Cement and concrete research*. Elsevier, 22(5), pp. 891–902.

Bhargava, K. *et al.* (2005) 'Modeling of time to corrosion-induced cover cracking in

reinforced concrete structures', *Cement and Concrete Research*. Elsevier, 35(11), pp. 2203–2218.

Bhargava, K. *et al.* (2006) 'Analytical model for time to cover cracking in RC structures due to rebar corrosion', 236, pp. 1123–1139. doi: 10.1016/j.nucengdes.2005.10.011.

'Biniam_Thesis_Nov_30 (44)' (no date).

Brough, A. R. and Atkinson, A. (2000) 'Automated identification of the aggregate–paste interfacial transition zone in mortars of silica sand with Portland or alkali-activated slag cement paste', *Cement and Concrete Research*. Elsevier, 30(6), pp. 849–854.

Castel, A. *et al.* (2003) 'Influence of steel–concrete interface quality on reinforcement corrosion induced by chlorides', *Magazine of Concrete Research*. Thomas Telford Ltd, 55(2), pp. 151–159.

Castel, A., François, R. and Arliguie, G. (2000) 'Mechanical behaviour of corroded reinforced concrete beams—Part 1: Experimental study of corroded beams', *Materials and Structures*. Springer, 33(9), pp. 539–544.

Chen, D. and Mahadevan, S. (2008) 'Chloride-induced reinforcement corrosion and concrete cracking simulation', *Cement and Concrete Composites*, 30(3), pp. 227–238. doi: 10.1016/j.cemconcomp.2006.10.007.

Chen, F. *et al.* (2018) 'Quantification of steel-concrete interface in reinforced concrete using Backscattered Electron imaging technique', *Construction and Building Materials*. Elsevier, 179, pp. 420–429.

Chen, F. *et al.* (2019) 'Effect of design parameters on microstructure of steel-concrete interface in reinforced concrete', *Cement and Concrete Research*. Elsevier, 119, pp. 1–10.

Chen, F., Baji, H. and Li, C.-Q. (2018) 'A comparative study on factors affecting time to cover cracking as a service life indicator', *Construction and Building Materials*. Elsevier, 163, pp. 681–694.

Chernin, L., Val, Æ. D. V and Volokh, K. Y. (2010) 'Analytical modelling of concrete

cover cracking caused by corrosion of reinforcement', pp. 543–556. doi: 10.1617/s11527-009-9510-2.

Chun-Qing, L., Melchers, R. E. and Jian-Jun, Z. (2006) 'Analytical model for corrosion-induced crack width in reinforced concrete structures', *ACI Materials Journal*. American Concrete Institute, 103(4), p. 479.

Das, B. B., Singh, D. N. and Pandey, S. P. (2011) 'Rapid chloride ion permeability of OPC-and PPC-based carbonated concrete', *Journal of Materials in Civil Engineering*. American Society of Civil Engineers, 24(5), pp. 606–611.

Davydov, D., Jirásek, M. and Kopecký, L. (2011) 'Critical aspects of nano-indentation technique in application to hardened cement paste', *Cement and Concrete Research*. Elsevier, 41(1), pp. 20–29.

Djelal, C. *et al.* (2016) 'Effect of marine environment on the behaviour of concrete structures reinforced by composite materials', in *MATEC Web of Conferences*, p. 2008.

Elsharief, A., Cohen, M. D. and Olek, J. (2003) 'Influence of aggregate size, water cement ratio and age on the microstructure of the interfacial transition zone', *Cement and concrete research*. Elsevier, 33(11), pp. 1837–1849.

Escalante-Garcia, J. I., Mendoza, G. and Sharp, J. H. (1999) 'Indirect determination of the Ca/Si ratio of the CSH gel in Portland cements', *Cement and concrete research*. Elsevier, 29(12).

Fang, C. *et al.* (2004) 'Corrosion influence on bond in reinforced concrete', *Cement and concrete research*. Elsevier, 34(11), pp. 2159–2167.

Fang, C. *et al.* (2006) 'Bond behaviour of corroded reinforcing steel bars in concrete', *Cement and Concrete Research*. Elsevier, 36(10), pp. 1931–1938.

Glass, G. K. *et al.* (2001a) 'Backscattered electron imaging of the steel–concrete interface', *Corrosion Science*. Elsevier, 43(4), pp. 605–610.

Glass, G. K. *et al.* (2001b) 'Backscattered electron imaging of the steel ± concrete interface', 43, pp. 605–610.

Glass, G. K. and Reddy, B. (2002) 'The influence of the steel concrete interface on the risk of chloride induced corrosion initiation', in *COST*, pp. 227–232.

Goudar, S. K., Das, Bibhuti Bhusan and Arya, S. B. (2019) 'Combined Effect of Marine Environment and pH on the Impedance of Reinforced Concrete Studied by Electrochemical Impedance Spectroscopy', in *Sustainable Construction and Building Materials*. Springer, pp. 635–649.

Goudar, S. K., Das, B B and Arya, S. B. (2019) 'Microstructural Study of Steel-Concrete Interface and Its Influence on Bond Strength of Reinforced Concrete', *ADVANCES IN CIVIL ENGINEERING MATERIALS*. AMER SOC TESTING MATERIALS 100 BARR HARBOR DR, W CONSHOHOCKEN, PA 19428-2959 USA, 8(1), pp. 171–189.

Guo, A. *et al.* (2015) 'Experimental investigation on the cyclic performance of reinforced concrete piers with chloride-induced corrosion in marine environment', *Engineering Structures*. Elsevier, 105, pp. 1–11.

Hime, W. G., Backus, L. A. and Li, C. Q. (1999) 'MODELING TIME-TO-CORROSION CRACKING IN CHLORIDE CONTAMINATED REINFORCED CONCRETE STRUCTURES. DISCUSSIONS AND CLOSURE', *ACI Materials Journal*, 96(5).

Hiremath, P. N. and Yaragal, S. C. (2017a) 'Effect of different curing regimes and durations on early strength development of reactive powder concrete', *Construction and Building Materials*. Elsevier, 154, pp. 72–87.

Hiremath, P. N. and Yaragal, S. C. (2017b) 'Influence of mixing method, speed and duration on the fresh and hardened properties of Reactive Powder Concrete', *Construction and Building Materials*. Elsevier, 141, pp. 271–288.

Horne, A. T., Richardson, I. G. and Brydson, R. M. D. (2007) 'Quantitative analysis of the microstructure of interfaces in steel reinforced concrete', *Cement and Concrete Research*. Elsevier, 37(12), pp. 1613–1623.

Hu, C. and Li, Z. (2015) 'A review on the mechanical properties of cement-based materials measured by nanoindentation', *Construction and Building Materials*. Elsevier

Ltd, 90, pp. 80–90. doi: 10.1016/j.conbuildmat.2015.05.008.

Isu, N., Ishida, H. and Mitsuda, T. (1995) 'Influence of quartz particle size on the chemical and mechanical properties of autoclaved aerated concrete (I) tobermorite formation', *Cement and concrete research*. Elsevier, 25(2), pp. 243–248.

Ji, X. and Song, Y. (2008) 'Experimental research on bond behaviors between steel bars and concrete after freezing and thawing cycles', *JOURNAL-DALIAN UNIVERSITY OF TECHNOLOGY*. DALIAN UNIVERSITY OF TECHNOLOGY, 48(2), p. 240.

Kenny, A. and Katz, A. (2010) 'Influence of the Interfacial Transition Zone Properties on Chloride Corrosion in Reinforced Concrete-Characterization of ITZ', in *Advanced Materials Research*. Trans Tech Publ, pp. 69–72.

Kenny, A. and Katz, A. (2012) 'Characterization of the interfacial transition zone around steel rebar by means of the mean shift method', *Materials and structures*. Springer, 45(5), pp. 639–652.

Kenny, A. and Katz, A. (2015) 'Statistical relationship between mix properties and the interfacial transition zone around embedded rebar', *Cement and Concrete Composites*. Elsevier, 60, pp. 82–91.

Al Khalaf, M. N. and Page, C. L. (1979) 'Steel/mortar interfaces: microstructural features and mode of failure', *Cement and Concrete Research*. Elsevier, 9(2), pp. 197–207.

Liao, K.-Y. *et al.* (2004) 'A study on characteristics of interfacial transition zone in concrete', *Cement and Concrete Research*. Elsevier, 34(6), pp. 977–989.

Liu, Y. (1996a) 'Modeling the Time-to-Corrosion Cracking of the Cover Concrete in Chloride Contaminated Reinforced Concrete Structures', *Dissertation*.

Liu, Y. (1996b) 'Modeling the time-to corrosion cracking of the cover concrete in chloride contaminated reinforced concrete structures'. Virginia Tech.

El Maaddawy, T. and Soudki, K. (2007) 'A model for prediction of time from corrosion initiation to corrosion cracking', *Cement and concrete composites*. Elsevier, 29(3), pp. 168–175.

Mondal, P., Shah, S. P. and Marks, L. D. (2008) 'Nanoscale characterization of cementitious materials', *ACI Materials Journal*. American Concrete Institute, 105(2), p. 174.

Monteiro, P. J. M., Gjorv, O. E. and Mehta, P. K. (1985) 'Microstructure of the steel-cement paste interface in the presence of chloride', *Cement and Concrete Research*. Elsevier, 15(5), pp. 781–784.

Moreno, M. *et al.* (2004) 'Corrosion of reinforcing steel in simulated concrete pore solutions: Effect of carbonation and chloride content', *Corrosion Science*. Elsevier, 46(11), pp. 2681–2699.

Morinaga, S. (1988) 'Prediction of service lives of reinforced concrete buildings based on rate of corrosion of reinforcing steel', *Special report of Institute of Technology, Shimizu Corporation*, 23.

Morris, W. and Vazquez, M. (2002) 'Corrosion of reinforced concrete exposed to marine environment', *Corrosion reviews*. De Gruyter, 20(6), pp. 469–508.

Němeček, J., Králík, V. and Vondřejc, J. (2013) 'Micromechanical analysis of heterogeneous structural materials', *Cement and Concrete Composites*. Elsevier, 36, pp. 85–92.

Novidis, D. G. and Pantazopoulou, S. J. (2008) 'Bond tests of short NSM-FRP and steel bar anchorages', *Journal of Composites for Construction*. American Society of Civil Engineers, 12(3), pp. 323–333.

Ollivier, J. P., Maso, J. C. and Bourdette, B. (1995) 'Interfacial transition zone in concrete', *Advanced cement based materials*. Elsevier, 2(1), pp. 30–38.

Page, C. L. (1975) 'Mechanism of corrosion protection in reinforced concrete marine structures', *Nature*. Nature Publishing Group, 258(5535), p. 514.

Page, C. L. (2009) 'Initiation of chloride-induced corrosion of steel in concrete: Role of the interfacial zone', *Materials and Corrosion*, 60(8), pp. 586–592. doi: 10.1002/maco.200905278.

Page, Chris L (2009) 'Initiation of chloride-induced corrosion of steel in concrete: role of the interfacial zone', *Materials and corrosion*. Wiley Online Library, 60(8), pp. 586–592.

Page, C. L. and Treadaway, K. W. J. (1982) 'Aspects of the electrochemistry of steel in concrete', *Nature*. Nature Publishing Group, 297(5862), p. 109.

Petre-Lazar, I. and Gérard, B. (2000) 'Mechanical behaviour of corrosion products formed at the steel-concrete interface. testing and modelling', *Condition monitoring of materials and structures*.

Pop, I. *et al.* (2013) 'Bond between powder type self-compacting concrete and steel reinforcement', *Construction and Building Materials*, 41, pp. 824–833. doi: 10.1016/j.conbuildmat.2012.12.029.

Prokopski, G. and Halbiniak, J. (2000) 'Interfacial transition zone in cementitious materials', *Cement and Concrete Research*. Elsevier, 30(4), pp. 579–583.

Richardson, I. G. (2000) 'The nature of the hydration products in hardened cement pastes', *Cement and Concrete Composites*. Elsevier, 22(2), pp. 97–113.

Ryou, J. S. and Ann, K. Y. (2008) 'Variation in the chloride threshold level for steel corrosion in concrete arising from different chloride sources', *Magazine of Concrete Research*. Thomas Telford Ltd, 60(3), pp. 177–187.

Sagoe-Crentsil, K. K. and Glasser, F. P. (1990) 'Analysis of the Steel/Concrete Interface', *Corrosion of Reinforcement in Concrete*, pp. 74–86.

Sahoo, S., Das, B. B. and Mustakim, S. (2016) 'Acid, Alkali, and Chloride Resistance of Concrete Composed of Low-Carbonated Fly Ash', *Journal of Materials in Civil Engineering*. American Society of Civil Engineers, 29(3), p. 4016242.

Santhanam, M., Cohen, M. D. and Olek, J. (2001) 'Sulfate attack research—whither now?', *Cement and concrete research*. Elsevier, 31(6), pp. 845–851.

Scrivener, K. L. *et al.* (1986) 'Analysis of phases in cement paste using backscattered electron images, methanol adsorption and thermogravimetric analysis', *MRS Online Proceedings Library Archive*. Cambridge University Press, 85.

Scrivener, K. L., Crumbie, A. K. and Laugesen, P. (2004) 'The interfacial transition zone (ITZ) between cement paste and aggregate in concrete', *Interface Science*, 12(4), pp. 411–421. doi: 10.1023/B:INTS.0000042339.92990.4c.

Scrivener, K. L. and Pratt, P. L. (1996) 'Characterization of interfacial microstructure', *Interfacial transition zone in concrete*. E&FN Spon, London, 2, pp. 3–18.

Shen, Q., Pan, G. and Zhan, H. (2017) 'Effect of Interfacial Transition Zone on the Carbonation of Cement-Based Materials', *Journal of Materials in Civil Engineering*, 29(7), p. 04017020. doi: 10.1061/(asce)mt.1943-5533.0001860.

Soylev, T. A. and Franc, R. (2003) 'Quality of steel – concrete interface and corrosion of reinforcing steel', *Cement and Concrete Research*. Elsevier, 33(9), pp. 1407–1415. doi: 10.1016/S0008-8846(03)00087-5.

Soylev, T. A. and François, R. (2003) 'Quality of steel-concrete interface and corrosion of reinforcing steel', *Cement and Concrete Research*, 33(9), pp. 1407–1415. doi: 10.1016/S0008-8846(03)00087-5.

Soylev, Tayfun A and François, R. (2003) 'Quality of steel–concrete interface and corrosion of reinforcing steel', *Cement and Concrete Research*. Elsevier, 33(9), pp. 1407–1415.

Söylev, T. A. and François, R. (2005) 'Corrosion of Reinforcement in Relation to Presence of Defects at the Interface between Steel and Concrete', 17(August), pp. 447–455.

Tawie, R. and Lee, H. K. (2010) 'Cement and Concrete Research Piezoelectric-based non-destructive monitoring of hydration of reinforced concrete as an indicator of bond development at the steel – concrete interface', *Cement and Concrete Research*. Elsevier Ltd, 40(12), pp. 1697–1703. doi: 10.1016/j.cemconres.2010.08.011.

Thoft-Christensen, P. (2000) 'Stochastic modeling of the crack initiation time for reinforced concrete structures', in *Advanced Technology in Structural Engineering*, pp. 1–8.

Turk, K., Karatas, M. and Ulucan, Z. C. (2010) 'Effect of the use of different types and dosages of mineral additions on the bond strength of lap-spliced bars in self-compacting concrete', *Materials and structures*. Springer, 43(4), pp. 557–570.

Tuutti, K. (1980) 'Service life of structures with regard to corrosion of embedded steel', *Special Publication*, 65, pp. 223–236.

Vedalakshmi, R. *et al.* (2016) 'Durability performance of rebar embedded in chloride admixed blended cement concretes Durability performance of rebar embedded in chloride admixed blended cement concretes', 2782(August). doi: 10.1179/174327809X409204.

Wang, X. H. *et al.* (2009) 'Application of nanoindentation testing to study of the interfacial transition zone in steel fiber reinforced mortar', *Cement and Concrete Research*. Elsevier, 39(8), pp. 701–715.

Wang, X., Wang, X. H. Ã. and Liu, X. L. Ã. (2004) 'Modelling effects of corrosion on cover cracking and bond in reinforced concrete Modelling effects of corrosion on cover cracking and bond in reinforced concrete', (July 2016). doi: 10.1680/macr.56.4.191.36306.

Weyers, R. E. (1998) 'Service life model for concrete structures in chloride laden environments', *Materials Journal*, 95(4), pp. 445–453.

Weyers, R. E., Sprinkel, M. M. and Brown, M. C. (2006) *Summary report on the performance of epoxy-coated reinforcing steel in Virginia*. Virginia Center for Transportation Innovation and Research.

Wong, H. S. *et al.* (2010) 'On the penetration of corrosion products from reinforcing steel into concrete due to chloride-induced corrosion', *Corrosion Science*. Elsevier, 52(7), pp. 2469–2480.

Wong, H. S., Head, M. K. and Buenfeld, N. R. (2006) 'Characterising the pore structure of cement-based materials using backscattered electron and confocal microscopy', in *Measuring, Monitoring and Modeling Concrete Properties*. Springer, pp. 495–502.

Xiao, J. *et al.* (2013) 'Properties of interfacial transition zones in recycled aggregate

concrete tested by nanoindentation', *Cement and Concrete Composites*. Elsevier, 37, pp. 276–292.

Xu, S. and Wang, H. (2008) 'Experimental study on bond-slip between ultra high toughness cementitious composites and steel bar', *Engineering Mechanics*, 11, pp. 53–61.

Yalciner, H., Eren, O. and Sensoy, S. (2012) 'An experimental study on the bond strength between reinforcement bars and concrete as a function of concrete cover, strength and corrosion level', *Cement and Concrete Research*. Elsevier, 42(5), pp. 643–655.

Yang, T. (2006) 'AFM Study of the Interactions between Moisture and the Surface of Cementitious Materials', (16534).

Yu, L., François, R. and Gagné, R. (2016) 'Influence of steel–concrete interface defects induced by top-casting on development of chloride-induced corrosion in RC beams under sustained loading', *Materials and Structures*. Springer, 49(12), pp. 5169–5181.

Yuan, Y. and Ji, Y. (2009) 'Modeling corroded section configuration of steel bar in concrete structure', *Construction and Building Materials*. Elsevier Ltd, 23(6), pp. 2461–2466. doi: 10.1016/j.conbuildmat.2008.09.026.

Zacharda, V., Štemberk, P. and Němeček, J. (2018) 'Nanomechanical Performance of Interfacial Transition Zone in Fiber Reinforced Cement Matrix', 760, pp. 251–256. doi: 10.4028/www.scientific.net/KEM.760.251.

Zayed, A. M. (1991) 'The Nature of the Concrete-Steel Rebar Interface in Plain and Silica Fume Concrete', *MRS Online Proceedings Library Archive*. Cambridge University Press, 245.

Zhang, L. *et al.* (2017) 'Cement and Concrete Research Novel understanding of calcium silicate hydrate from dilute hydration', *Cement and Concrete Research*. Elsevier, 99(December 2016), pp. 95–105. doi: 10.1016/j.cemconres.2017.04.016.

Zhao, Y. *et al.* (2011) 'Non-uniform distribution of rust layer around steel bar in concrete', *Corrosion Science*. Elsevier Ltd, 53(12), pp. 4300–4308. doi:

10.1016/j.corsci.2011.08.045.

Zhao, Y. *et al.* (2016) 'Corrosion-induced concrete cracking model considering corrosion product-filled paste at the concrete/steel interface', *Construction and Building Materials*. Elsevier, 116, pp. 273–280.

Zhao, Y., Dai, H. and Jin, W. (2012) 'A study of the elastic moduli of corrosion products using nano-indentation techniques', *Corrosion Science*. Elsevier, 65, pp. 163–168.

Zhao, Y., Wu, Y. and Jin, W. (2013) 'Distribution of millscale on corroded steel bars and penetration of steel corrosion products in concrete', *Corrosion Science*. Elsevier Ltd, 66, pp. 160–168. doi: 10.1016/j.corsci.2012.09.014.

Zhu, W. and Bartos, P. J. M. (1997) 'Assessment of interfacial microstructure and bond properties in aged GRC using a novel microindentation method', *Cement and Concrete Research*. Elsevier, 27(11), pp. 1701–1711.

Zhu, W. and Bartos, P. J. M. (2000) 'Application of depth-sensing microindentation testing to study of interfacial transition zone in reinforced concrete', *Cement and Concrete Research*. Elsevier, 30(8), pp. 1299–1304.

Zhu, W., Sonebi, M. and Bartos, P. J. M. (2004a) '<Zhu Sonebi Bartos MS04 bond in scc.pdf>', 37(September), pp. 442–448.

Zhu, W., Sonebi, M. and Bartos, P. J. M. (2004b) 'Bond and interfacial properties of reinforcement in self-compacting concrete', *Materials and structures*. Springer, 37(7), p. 442.

PUBLICATIONS BASED ON THE PRESENT RESEARCH WORK

<u>**International Journals**</u> **(SCI and Scopus indexed)**

Sharan Kumar Goudar, B. B. Das and S B Arya, "Microstructural Study of Steel-Concrete Interface and its Influence on Bond Strength of Reinforced Concrete", *Advances in Civil Engineering Materials*, **ASTM International**, Vol. 8(1), 2019, pp. 171-189.

Sharan Kumar Goudar, B. B. Das, S B Arya and Shivaprasad K N, "Influence of sample preparation techniques on microstructure and nano-mechanical properties of steel-concrete interface" *Construction and Building Materials*, **Elsevier**, Vol. 256, 2020, pp. 119242.

Sharan Kumar Goudar, B. B. Das, S B Arya and Sumukh E P, "Effect of marine environment exposure on engineering properties of steel-concrete interface and service life prediction of RC structures" (Submitted to Engineering Structures, Elsevier).

<u>**Book Chapters**</u> **(Scopus indexed)**

E P Sumukh, **Sharan Kumar Goudar** and B B Das, "Predicting the service-life of reinforced concrete by incorporating the experimentally determined properties of steel-concrete interface and corrosion", In Trending Moments and Steer Forces – Civil Engineering Today" during 31st October – 01st November 2019 at Don Bosco College of Engineering, Fatorda, Goa. (**Accepted for Springer Book Chapter**).

Sharan Kumar Goudar, B B Das and S. B. Arya, "Combined Effect of Marine Environment and pH on the Impedance of Reinforced Concrete Studied by Electrochemical Impedance Spectroscopy", In Sustainable Construction and Building Materials, Lecture Notes in Civil Engineering, Vol. 25, *Springer Nature*, Singapore, 2019, pp. 635-649.

Sharan Kumar Goudar, Das B B, Arya S B, "The significance of high volume GGBS on bond strength and microstructure properties of steel-concrete interface", National Conference on Advances in Sustainable Construction Materials (ASCM) 2019, NIT Warangal, 15-16 March 2019. **(Under Review for Springer Book Chapter)**.

Sumukh E P, **Sharan Kumar Goudar** and B B Das, "A Review on the Properties of Steel-Concrete Interface and Characterization Methods", Smart Materials and Techniques for Sustainable Development (SMTS – 2019), Dr. N. G. P. Institute of Technology, Coimbatore, Tamilnadu, India. April 4-5, 2019 **(Accepted for Springer book chapter).**

Sharan Kumar Goudar, A Gokul and B B Das, "Influence of 'pH' on concrete bond strength retention in simulated marine environment." 2nd International Conference on Advances in Concrete, Structural and Geotechnical Engineering (ACSGE-2018), BITS Pilani, India, 26-28 February 2018, *Bloomsbury Publishing India Pvt. Ltd*. pp. 683-687.

Conferences proceedings

Sharan Kumar Goudar, B B Das and S B Arya, "Corrosion behavior of OPC, PPC and PSC based concretes in harsh marine environment through electrochemical impedance spectroscopy." 5th International Corrosion Prevention Symposium for Research Scholars (CORSYM 2018), IIT Madras, Chennai, India, 23-24 March 2018, pp. 129-130.

Sharan Kumar Goudar, P P Kiran Ram, A Gokul, B B Das and S. B. Arya, "Bond strength and corrosion resistance of reinforced concrete exposed to simulated acidic and alkaline marine environment", UKIERI Concrete Congress, NIT Jalandhar, Punjab, 05-08 March 2019.

OTHER PUBLICATIONS

International Journals (SCI and Scopus indexed)

Parameshwar N Hiremath, H P Thanu, Basavana gowda S N and **Sharan Kumar Goudar**, "Early strength development of blended concrete under different curing conditions", *Emerging Materials Research*, ***ICE Publishing***, Vol. 9(1). DOI: 10.1680/jemmr.19.00066.

Book Chapters (Scopus indexed)

Sharan Kumar Goudar, Santhosh Kumar Gedela and B B Das, "A review on mechanical and microstructure properties of reinforced concrete exposed to high temperatures" International Conference on Recent Development in Sustainable Infrastructure – Materials and Management (ICRDSI-2019) at KIIT, Deemed University, Bhubaneshwar, India, during 11th July – 13th July 2019 (**Accepted for Springer book chapter**) – **Best Paper Award.**

Sharan Kumar Goudar, Shivaprasad K N, B. B. Das, "Mechanical Properties of Fiber Reinforced Concrete Using Coal-Bottom Ash as Replacement of Fine Aggregate" Lecture Notes in Civil Engineering, Sustainable Construction and Building Materials, Select Proceedings of ICSCBM 2018 (**Springer book chapter**).

Rohini Srikumar, **Sharan Kumar Goudar**, B. B. Das, "Durability studies of polypropylene fibre reinforced concrete" Lecture Notes in Civil Engineering, Sustainable Construction and Building Materials, Select Proceedings of ICSCBM 2018 (**Springer book chapter**).

Shonu Yadav, **Sharan Kumar Goudar**, B. B. Das, "Durability studies of steel fibre reinforced concrete" Lecture Notes in Civil Engineering, Sustainable Construction and Building Materials, Select Proceedings of ICSCBM 2018 (**Springer book chapter**).

CURRICULUM VITAE

PERSONAL DETAILS:

Name	:	SHARAN KUMAR
Surname	:	Goudar
Father's Name	:	Hanamanthgouda Goudar
Mother's Name	:	Shashikala
Date of Birth	:	21-07-1989
E-Mail ID	:	sgcr17@gmail.com
Contact Number	:	Mobile: +91-9538566097

EDUCATION QUALIFICATION:

Course	Institution/University	Year of Passing	Class obtained	Percentage of Marks
B.E. (Civil Engineering)	Poojya Doddappa Appa College of Engineering, Gulbarga.	2011	First Class with Distinction	7.84 (CGPA)
M.Tech (Structural Engineering)	Basaveshwar Engineering college, Bagalkot.	2013	First Class with Distinction	8.34 (CGPA)

WORK EXPERIENCE:

Organization	Post held	Duration
Vivekananda College of Engineering and Technology, Puttur, Dakshina Kannada, Karnataka	Assistant Professor	July 2013 to June 2014
Mangalore Institute of Technology and Engineering, Moodabidri, Dakshina Kannada, Karnataka	Assistant Professor	July 2014 to June 2015
National Institute of Technology Karnataka, Surathkal, Mangalore, Karnataka	Research Scholar	July 2015 to September 2019
College of Engineering Pune (COEP), Maharashtra	Assistant Professor	September 2019 to Till date

RESEARCH PUBLICATIONS:

Type of Publication	No. of Publications (Under Review)
International Journal Papers	3 (4)
Book Chapters	9 (3)
International Conference	11 (2)